Hydrofoils with High Dihedral Wings

Justin Ayinbila Amoah

A Thesis

In

The Department

Of

Mechanical, Industrial and Aerospace Engineering

Presented in Partial Fulfillment of the Requirements

for the Degree of Master of Applied Science (Mechanical Engineering) at

Concordia University

Montreal, Quebec, Canada

July 2025

© Justin Ayinbila Amoah, 2025

CONCORDIA UNIVERSITY

School of Graduate Studies

This is to certify that	the thesis prepared	
By:	Justin Ayinbila Amoah	
Entitled:	Hydrofoils with High Dihedra	ıl Wings
and submitted in parti	al fulfillment of the requirement	nts for the degree of
	Master of Applied Science (N	Mechanical Engineering)
complies with the reg originality and quality	•	meets the accepted standards with respect to
Signed by the final Ex	xamining Committee:	
		Chair
	Dr Mojtaba Kheiri	
		Examiner
	Dr Mojtaba Kheiri	
		Examiner
	Dr Youmin Zhang	
		Thesis Supervisor
	Dr. Hang Xu	
Approved by		
	Dr. Muthukumaran Packiri	samy
	Chair, Department of Mech	nanical, Industrial and Aerospace Engineering
2025		
	Mourad Debbabi	
	Dean, Gina Cody School o	f Engineering and Computer Science

Abstract

Hydrofoils are among the most efficient watercraft and offer a promising solution for sustainable maritime transport through electrification. Hydrofoils, i.e., wings operating in water, lift watercraft above the water surface to decrease drag and increase cruising speed. The reduction in drag translates to improved cruising efficiency, which is essential for electric watercraft with batteries that have limited energy density. However, maintaining sufficient stability during the foiling mode remains a critical concern due to the limited operational altitude at a one-foot scale and the complex two-phase flow environment, unlike aircraft. This thesis investigates the influence of high dihedral angles (30° - 50°) on the passive stability characteristics, specifically roll, pitch, and yaw, of a canard-configured surface-piercing hydrofoil watercraft.

This thesis proposes a multiphase Computational Fluid Dynamics (CFD) simulation framework via a commercial numerical simulation package (Star-CCM+) to simulate the air-water interface. The proposed framework can address the two-phase gas-liquid complex flow condition, including ventilation and submergence effects, using the Volume of Fluid (VOF) model. The watercraft was modeled as a rigid body, and the effect of the dihedral angle was isolated for the study. Small disturbance theory was used to obtain stability derivatives, which assessed the hydrofoil watercraft's initial response to perturbations.

Simulation results demonstrate that dihedral angles in the range of 30° to 40° provide the most favorable initial stability characteristics across the longitudinal, lateral, and directional stability axes. In contrast, dihedral angles beyond 45° lead to diminished pitch and yaw stability and increased coupling between motion axes, which may increase the risk of oscillatory behavior. These findings highlight the importance of carefully selecting dihedral angles during the design process.

This work presents a validated CFD-based framework for evaluating hydrofoil stability under realistic two-phase flow conditions. The research outcomes provide insight into the initial tendency of high dihedral angles to disturbances in the longitudinal, lateral, and directional stability axes.

Acknowledgments

The past two years have been a very interesting time in my life. I thank God for having been with me through everything. This is an experience I would definitely choose again if I went back in time, with some minor changes, of course. The people around me made it worth it, and this goes out to you all.

To Dr. Hang Xu, my supervisor, who guided me throughout my program, both academically and personally. Thank you for the opportunity to study with you and for all the support you provided. Thank you for always being available and pushing us to be better. I am also grateful for the snacks during our meetings. I have grown so much in the past two years.

To the industry partner and students who worked with me on hydrofoil projects, it was a joy to discuss "Navalspace" with you all.

To my lab mates and members of the Advanced Metamaterials and Manufacturing Group, especially Alexandra, Atharva, and Aron, your support and encouragement kept me going.

To Allyson, her family, who are like family, and research group, my friends from the Aircraft Systems Lab, and my friends beyond school, thank you for your encouragement, insights, and experiences you shared with me. I am glad to know you.

To the Dream Team, Andrew and Gala, who made graduate studies more interesting. Thank you for the time you spent with and for me and your insights from the aerospace perspective. I am grateful to have met you.

To ASFB 5, thank you for being with me throughout and for your unwavering support and belief in me. Thank you for everything.

Last but not least, to my family, especially Mama, Dad, fellow triplet brothers, and baby Jesse, for your unconditional love and support across several seas. You have always been with me from the beginning, and I cannot begin to express how grateful I am to have you in my life. Thank you for believing in me and supporting me in every way and step.

I am truly grateful to all who have supported me and made this work a reality.

Table of Contents

Table of Contents	V
Table of Figures	viii
Table of Tables	xi
Nomenclature	xiii
Chapter 1: Introduction	1
1.1 Background and Motivation	1
1.2 Goal	4
1.3 Thesis Structure	4
Chapter 2: Literature Review	5
2.1 Introduction to Hydrofoils	5
2.1.1 Current Advancements in Hydrofoil Technology	7
2.2 Physics of Hydrofoils	8
2.2.1 Lift and Drag	9
2.2.2 Free Surface Effects	10
2.3 Hydrofoil Configurations	12
2.4 Hydrofoil Motions	14
2.4.1 State Vector	16
2.5 Hydrofoil Stability	16
2.6 Stability Derivatives	18
2.6.1 Stability Derivatives for Hydrofoil Stability Analysis	19
2.7 Wing Dihedrals	20
2.8 Current State of Hydrofoil Analysis Methods	23
2.9 Research Gap	25
2.10 Objectives	26

Chapter 3: Methodology	27
3.1 Nomenclature and Axis Convention	27
3.2 Hydrofoil Layout Selection	28
3.2.1 Design Requirements	28
3.2.2 Benchmarking and Configuration Analysis	28
3.3 Simulation Methodology	31
3.3.1 Mesh Generation	31
3.3.2 Physical Models	32
3.3.3 Domain and Boundary Conditions	32
3.3.4 Convergence Criteria	33
3.4 Post-processing	35
3.4.1 Extracted Output	35
3.4.2 Stability Derivatives of a Hydrofoil Watercraft	35
3.4.3 Determination of Stability Derivatives	36
3.5 Variable Control Method for Investigating the Effect of High Dihedral Wings	38
3.6 Assumptions and Limitations of the Proposed CFD Framework	39
Chapter 4: Results and Discussion	41
4.1 Validation of CFD Simulation Framework	41
4.2 Application of the Simulation Framework to Hydrofoil Configurations	43
4.2.1 Overview of Evaluated Configurations	43
4.2.2 Low-Speed Performance: Takeoff and Cruising at 7 km/h	44
4.2.3 Mid-Speed Performance: Cruise (10.80 - 11.52 km/h)	45
4.2.4 Human versus Electric Propulsion Analysis	45
4.3 Stability Margin Evaluation	46
4.3.1 Passive Stability Margin Analysis	46

4.3.2 Mission Profile Simulation	47
4.4 Equilibrium Position	48
4.5 Stability Derivatives	49
4.5.1 Stability Derivatives with Respect to Pitch $(\partial \theta)$	50
4.5.2 Stability Derivatives with Respect to Roll $(\partial \phi)$	53
4.5.3 Stability Derivatives with Respect to Yaw $(\partial \psi)$	56
Chapter 5: Summary and Conclusion	59
5.1 Contribution and Summary of Findings	59
5.2 Future Work	60
List of Related Publications	62
References	63
Appendix A: Hydrofoil Configurations	72
Appendix B: Hydrofoil Selection and Performance Study	74
Appendix C: High Dihedral Case Study II	80
Appendix D: Dihedral Effect Isolation Study	87
Appendix E: Simulation Setup and Convergence	89

Table of Figures

Figure 1.1. HMCS Bras d'Or, a hydrofoil that served in the Canadian Navy in the 1960s	. 1
Figure 2.1. Watercraft resistance versus speed (Yamaha SX220 above and Quadrofoil below)	. 5
Figure 2.2. Enrico Forlanini demonstrating his foiler on Lake Maggiore, early 20 th century	. 6
Figure 2.3. a) Bell Hydrodome, b) Boeing Jetfoil, and c) Supramar PT 50	. 7
Figure 2.4. America's Cup sailing hydrofoil watercraft a) AC72 and b) AC75	. 8
Figure 2.5. Forces acting on a hydrofoil watercraft in the foiling mode (ENVO waterbike	
pontoons)	. 9
Figure 2.6. Typical lift and drag characteristics of a hydrofoil wing	10
Figure 2.7. Illustration of submergence and foil AoA, α	11
Figure 2.8. Two main types of lifting hydrofoils: a) Surface-piercing hydrofoil and b) Fully	
submerged hydrofoil	12
Figure 2.9. Foil layouts	13
Figure 2.10. Hydrofoil motion	15
Figure 2.11. Hydrofoil mission profile	15
Figure 2.12. Aircraft (hydrofoil) longitudinal stability	18
Figure 3.1. Illustrates the naming convention of major components of a hydrofoil watercraft	
using the Navier N30 model	27
Figure 3.2. Notable recreational watercraft with less than 11 passengers.	29
Figure 3.3. A CAD model with exaggerated wingspan for dihedral wing visualisation generated	d
by Autodesk Fusion 360	30
Figure 3.4. Mesh visualisation of the hydrofoils	32
Figure 3.5. Simulation boundary conditions and domain size, where $L_{\rm wc}$ is the typical length of	•
the watercraft	33
Figure 3.6. Flowchart of the stability derivative determination process	36
Figure 3.7. A small perturbation applied to the pitch angle in the CFD simulation	37
Figure 3.8. A small perturbation applied to the roll (left) and yaw (right) angles, in the CFD	
simulation	38
Figure 3.9. Render of canard configured hydrofoil watercraft with varying dihedral angles	
(wingspan is exaggerated for representation)	39
Figure 4.1. Validation of CFD data using experimental data for dihedral hydrofoils	42

Figure 4.2. Hydrofoil configurations: a) Hybrid layout, b) Surface-piercing dihedral tandem	
layout, and c) Surface-piercing dihedral canard layout	3
Figure 4.3. Passive stabilizing effect. From top to bottom, trim, yaw, and roll stability. From left	-
to right, initial state, after introduction of disturbance, and return to stable state	7
Figure 4.4. A sample mission profile of the hybrid configuration	8
Figure 4.5. Sinkage changes with respect to dihedral angle variation	8
Figure 4.6. Sinkage at the equilibrium position	9
Figure 4.7. Trim position at equilibrium stages of hydrofoil with different dihedral angles 4	9
Figure 4.8. Moments generated by the dihedral wings on opposite sides in response to a pitch	
disturbance (Moment not drawn to scale). The red moment represents the left wing, and the	
green moment represents the right wing. a) 35° dihedral model and b) 45° dihedral model 5°	1
Figure 4.9. Demonstration of the change in lift and moment arm due to changes in the submerge	d
area of the dihedral wing	5
Figure 4.10. Moments generated by the opposing dihedrals in response to a roll disturbance	
(Force, moment and moment arm not drawn to scale). The red represents the left wing, and the	
green represents the right. a) 35° and b) 45° dihedral model	5
Figure 4.11. Moments generated by the dihedral wings on opposite sides in response to a yaw	
disturbance (Moments not drawn to scale). The red moment represents the left wing, and the	
green moment represents the right wing. a) 35° dihedral model and b) 45° dihedral model 5°	7
Figure A.1. Literature review poster	3
Figure B.1. Model hydrofoil configurations from left to right: a) Hybrid layout, b) Surface-	
piercing dihedral tandem layout, and c) Surface-piercing dihedral canard layout	6
Figure C.2. Configuration a (Hybrid configuration)	9
Figure C.1. Visualization of the 30° dihedral model equilibrium position	0
Figure C.2. Trim at the equilibrium position	1
Figure C.3. Introducing a pitch disturbance to the hydrofoil system	1
Figure E.1. Sample drag report plot	0
Figure E.2. Sample lift report plot	0
Figure E.3. Sample motion plot	0
Figure E.4. Sample moment plot	1
Figure E.5. Sample wall v+ value study	1

Figure E.6. Sample mesh skewness angle study	92
Figure E.7. Sample mesh quality study	92
Figure E.8. Lift mesh convergence plot	94

Table of Tables

Table 2.1. Stability derivatives	. 19
Table 2.2 Summary of related literature with surface-piercing hydrofoils	21
Table 2.3 Summary of related literature with surface-piercing hydrofoils continuation	. 22
Table 3.1. Design requirements	28
Table 3.2. Hydrofoil watercraft parameters	30
Table 4.1. Quantitative validation of CFD results against experimental data	42
Table 4.2. KCS hull validation comparison	43
Table 4.3. Configuration performance comparison	44
Table 4.4. Performance estimation of selected configurations	44
Table 4.5. Summary of configuration performance	46
Table 4.6. Nondimensionalized stability derivatives with respect to pitch	50
Table 4.7. Moments generated by the dihedral wings on opposite sides in response to a pitch	
disturbance	51
Table 4.8. Nondimensionalized stability derivatives with respect to roll	53
Table 4.9. Moments generated by the dihedral wings on opposite sides in response to a roll	
disturbance	54
Table 4.10 Stability derivatives in response to a roll disturbance	54
Table 4.11. Nondimensionalized stability derivatives with respect to yaw	56
Table 4.12. Moments generated by the dihedral wings on opposite sides in response to a yaw	
disturbance	56
Table 4.13. Stability derivatives in response to a yaw disturbance	. 57
Table B.1. Hydrofoil layout decision matrix	74
Table B.2. Design requirements	. 75
Table B.3. Performance estimation considering both human power and electric propulsion	. 77
Table B.4. Performance estimation considering electric propulsion only	. 78
Table C.1. Stability derivatives coefficients with respect to pitch	82
Table C.2. Stability derivatives with respect to roll	84
Table C.3. Stability derivatives with respect to yaw	85
Table D.1. Canard incidence angle adjustment	87
Table D.2. Stability derivatives in response to a roll disturbance	87

Table D.3. Stability derivatives in response to a pitch disturbance	88
Table D.4. Stability derivatives in response to a yaw disturbance	38
Table E.1 Simulation conditions	39
Table E.2. Mesh convergence study	94
Table E.3. Force and moment change mesh convergence study	94

Nomenclature

Acronyms

AC	America's Cup
AoA	Angle of Attack
AR	Aspect Ratio
CAD	Computer-Aided Design
CFD	Computational Fluid Dynamics
CG	Center of Gravity
CSME	Canadian Society for Mechanical Engineering
DOC	Direct Operational Cost
DoF	Degrees of Freedom
EOM	Equations of Motion
GHG	Green House Gas
IMO	International Maritime Organisation
KCS	KRISO Container Ship
LES	Large Eddy Simulations
LHS	Left Hand Side
PHM	Patrol Hydrofoil Missile
RANS	Reynolds-Averaged Navier-Stokes
RHS	Right Hand Side
RMSE	Root Mean Square Error
SST	Shear Stress Transport
URANS	Unsteady Reynolds-Averaged Navier-Stokes
VOF	Volume of Fluid
	Symbols
	-

$C_{l_{ heta}}$	Roll moment coefficient with respect to pitch
C_{l_ϕ}	Roll moment coefficient with respect to roll
$C_{l_{\psi}}$	Roll moment coefficient with respect to yaw
$C_{m_{\theta}}$	Pitch moment coefficient with respect to pitch

$C_{m_{\phi}}$	Pitch moment coefficient with respect to roll
$C_{m_{\psi}}$	Pitch moment coefficient with respect to yaw
$C_{n_{\theta}}$	Yaw moment coefficient with respect to pitch
$C_{n_{\phi}}$	Yaw moment coefficient with respect to roll
$C_{n_{\psi}}$	Yaw moment coefficient with respect to yaw
C_D	Drag coefficient
C_L	Lift coefficient
C_l	Roll moment coefficient
C_m	Pitch moment coefficient
C_n	Yaw moment coefficient
F_n	Froude number
0	Degree angle
b	Wingspan
С	Chord length
D	Drag
F	Force
<i>f(h)</i>	Submergence depth correction factor
g	Acceleration due to gravity
h	Submergence depth
I_{xy}	Product of inertia about the x- and y-axes
I_{xz}	Product of inertia about the x- and z-axes
I_{yz}	Product of inertia about the y- and z-axes
L	Lift
L_{roll}	Moment about the x-axis
L_{wc}	Watercraft length
M	Moment about the y-axis
N	Moment about the z-axis
p	Roll rate
p(t)	Time-averaged pressure

Pitch rate

q

- *r* Yaw rate
- S Reference area
- t Time
- T When used as a superscript, it indicates the transpose of a matrix.
- *u* Surge velocity
- U Inflow velocity
- v Saw velocity
- V Velocity in the x direction
- w Heave velocity
- x x coordinate position
- X Longitudinal axis
- y y coordinate position
- Y Lateral axis
- z z coordinate position
- Z Directional axis
- α Angle of attack
- Γ Dihedral angle
- θ Pitch angle
- μ Dynamic viscosity
- ξ State variable
- ρ Density of water
- φ Roll angle
- ψ Yaw angle

Chapter 1: Introduction

This chapter presents the background and motivation of the present study, along with an outline of the subsequent chapters of this thesis.

1.1 Background and Motivation

The International Maritime Organization (IMO) has implemented measures to reduce greenhouse gas (GHG) emissions by at least 40% by 2030 and 70% by 2050 compared to the 2008 level [1]. This has increased the demand for more sustainable alternatives to fossil fuels. Potential solutions include sustainable bio-oil, hydrogen fuel, and electrical power. Electrical power is easy to access; however, electrical batteries cannot provide the same level of energy density as bio-oil and hydrogen [2]. To be comparable in performance, electrical watercraft need to be more efficient, e.g. cruising at low drag, to meet design requirements, such as long range. Hydrofoil technology reduces drag via lifting the boat hull above the water in the foiling mode [3] to improve energy efficiency [4], making it an environment-friendly solution.



Figure 1.1. HMCS Bras d'Or, a hydrofoil that served in the Canadian Navy in the 1960s [5]

Hydrofoils (Fig. 1.1) change their cruising mode from displacement to low-drag foiling at the cost of vanishing ship stability. In the displacement modes, hydrofoils float via buoyancy and are compliant with ship stability, which is assessed by the adequate distance between the center of gravity (CG) and the center of buoyancy [6]. Compared to ordinary boats, the hydrofoil below the hull lowers the CG, increases its distance between the buoyancy center, and thus increases the

displacement mode's ship stability. However, in the foiling mode, the hull is lifted, leaving only the hydrofoil in the water with negligible buoyancy. Thus, the ship stability vanishes. Supported mainly by lift, the hydrofoils' stability is analogous to the flight stability of aircraft. Stability in flight dynamics refers to the ability of an aircraft to return to a particular flight condition after external disturbances without active control of pilots or computers [7]. This passive returning process usually occurs in correspondence to an obvious change in altitude.

The stability of a hydrofoil in foiling mode is different from that of an aircraft. Unlike the high cruising altitude of aircraft, the hydrofoil's ride flying height, i.e. the distance between the hull and the water surface, is at only a one-foot scale. External disturbances, such as waves and gusts, can pitch, roll, or yaw hydrofoils with a coupled change in altitude [8]. Altitude variation causes lift change due to the free surface effect in the two-phase flow, which influences the altitude in turn. Altitude loss due to disturbance can cause the hydrofoil hull to contact the water surface with high drag, decrease velocity, lose lift, and then stop the foiling mode. The hydrofoil's limited flying height, coupled with the two-phase flow condition, yields different stability responses to disturbances in contrast with aircraft. Although stabilizer concepts can be borrowed from aircraft, additional measures are necessary to equip hydrofoils with sufficient flying stability in the foiling mode.

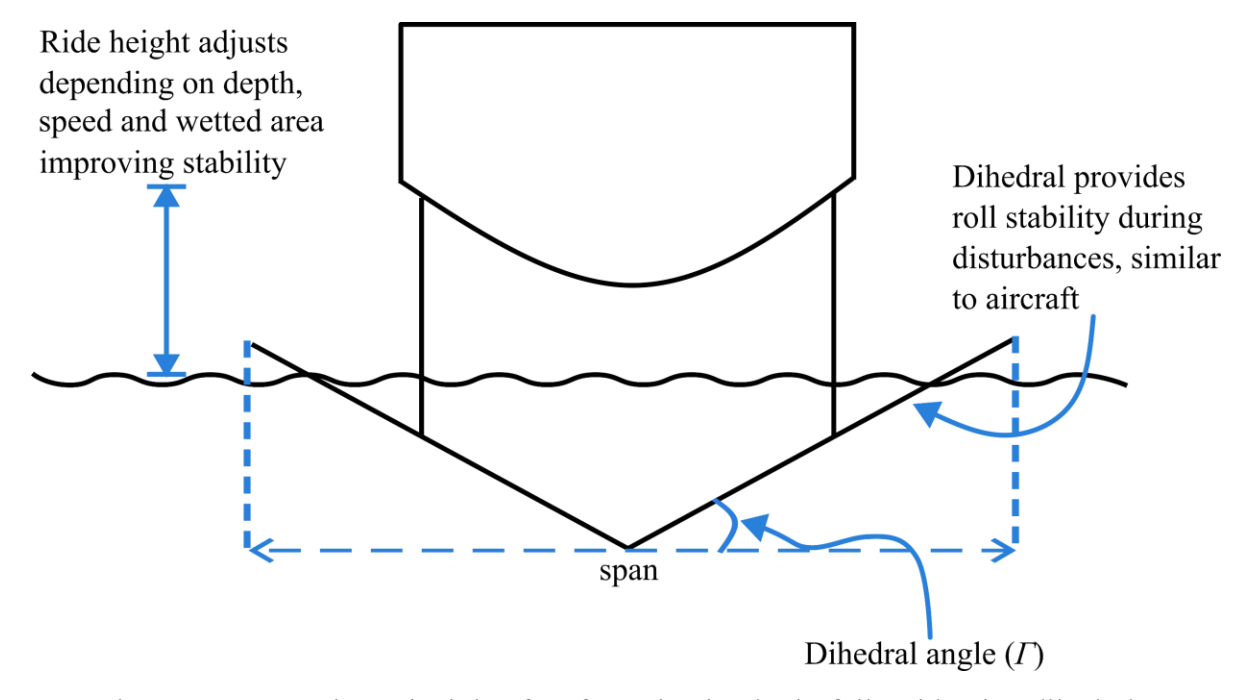


Figure 1.2. Operation principle of surface-piercing hydrofoils with wing dihedral

To improve stability, computerized active control systems are often employed on large-tonnage hydrofoils [9-10]; however, the complexity of the control system increases design, manufacture, and operation costs [11]. In contrast, passive stability measures, such as stabilizing planes and dihedral wings, perform as alternative low-cost approaches. Wing dihedral is the angle of the wing with respect to the horizontal when seen from the front. In aircraft design, dihedral effects have been widely used to enhance roll stability [12]. Under a roll disturbance, aircraft roll with coupled yaw and sideslip, which decreases altitude. In this flight mode, dihedral generates differences in effective angles of attack (AoA) on different sides of the wings. The lower wing experiences a higher AoA than the higher wing, enabling a lift discrepancy and creating righting rolling moments. After an altitude loss, the aircraft with rolling stability can return to level flight [7]. In contrast to the aircraft's dihedral effect, watercraft's low ride height prevents the sensible sideslip of the dihedral hydrofoil from generating efficient righting moments before contacting the water surface and losing the foiling mode. Instead, if the hydrofoil is surface-piercing (when the wing tips are above the water surface as shown in Fig. 1.2), rolling dihedral hydrofoils (i.e. one wing is lower than the other) increases the wetted area on the lower wing and generate more lift. The different lifts generated on the two sides of the wings perform as righting rolling moments. Dihedral wings (Fig. 1.2) can thus elicit the roll stability of hydrofoils.

The aircraft dihedral angles range from 0° to 7°, and their dihedral effect in single-phase flow has been extensively investigated in literature [12-15]. Due to the surface-piercing requirements, i.e. the wing tip must stick out of the water, the dihedrals of hydrofoils range between 15° and 60°. However, the stability effect of high dihedral angles, especially when the dihedral is above 30°, has not been thoroughly investigated. The further investigation should include the effect of the air-water two-phase flow, such as submergence effect, wave-induced disturbance, and cavitation, on the high dihedral wings' contributions to the hydrofoil's roll, pitch, yaw, and depth stability.

This research aims to integrate surface-piercing high dihedral wings in electrical hydrofoils to improve the roll, pitch, yaw, and depth stability. The expected research outcome can improve the stability of hydrofoils without the need for active control and thus increase safety, as well as reduce design, manufacture, and operation costs. Hydrofoil technology, which is more accessible to the wider maritime community, offers a promising marine electrical transportation solution in response to the IMO's GHG reduction targets.

1.2 Goal

The goal of this thesis is to improve the passive stability (e.g. roll, pitch, yaw, and depth stability) of hydrofoil watercraft in the foiling mode via integrating surface-piercing high-dihedral wings. The current study selects and discusses different configurations with dihedral wings. Through proposing a numerical simulation methodology, this research aims to evaluate the stability of the hydrofoil at different dihedral angles under different disturbances. The research outcome will find the optimum dihedral wing design to improve the stability of the hydrofoil.

1.3 Thesis Structure

This thesis presents a framework for analyzing the stability of hydrofoil watercraft using the numerical simulation method. While the introduction chapter outlines the motivation and goal of the study, Chapter 2 covers a detailed overview of hydrofoil watercraft, including configurations, historical developments, and hydrodynamic principles. Chapter 3 details the methodologies, including design via a conceptual approach and CFD simulation. Chapter 4 presents the results from the stability analysis and then discusses the implications of dihedral angles for hydrofoil stability. Chapter 5 concludes the thesis and suggests directions for future research.

Chapter 2: Literature Review

This chapter begins with an overview of hydrofoil watercraft through history, applications, and current design challenges, followed by hydrodynamic principles on which hydrofoils operate. Various hydrofoil configurations are reviewed, and the chapter concludes with an overview of the thesis scope and the identified research gap.

2.1 Introduction to Hydrofoils

A hydrofoil is a wing or lifting surface operating in water [16]. By this definition, a hydrofoil watercraft is a type of watercraft supported above the water surface by these underwater wings. The underwater wings produce a hydrodynamic force, known as lift, to raise the watercraft hull out of the water in a foiling mode. The foiling mode reduces the hydrodynamic resistance, especially at high speeds, as depicted in Fig. 2.1.

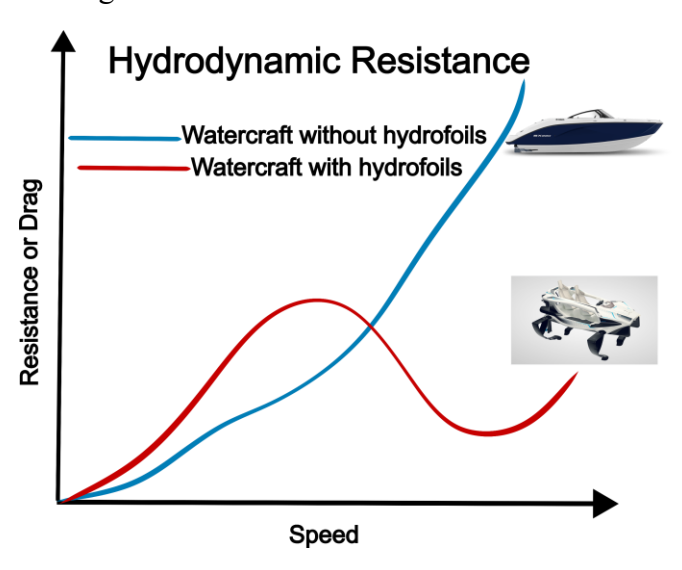


Figure 2.1. Watercraft resistance versus speed (Yamaha SX220 [17] above and Quadrofoil [18] below)

Early stage: Hydrofoils have been in existence since the 19th century [19]. The first developed hydrofoil came into existence in the late 1800s to early 1900s during the early days of airplanes [20]. Following the introduction of the concept of lift generation by an inclined plate moving through a fluid medium in 1809 by Sir George Cayley [21], and the subsequent mathematical formulation by Martin Kutta in 1902 [22], several new modes of travel emerged. Among which are air travel through aircraft and faster movement over water using hydrofoil watercraft. The first successful hydrofoil

boat was designed by Enrico Forlanini in 1905 [23]. By 1906, his 60 hp airscrew-driven boat had reached a speed of almost 40 knots (Fig. 2.2) [23]. In 1909, Captain H. C. Richardson attached foils to a canoe and later applied the same concept to a dinghy (small boat) in 1911 [24]. In 1919, Alexander Graham Bell developed the Hydrodrome [25] (Fig. 2.3 (a)), which reached a speed of 79 mph.



Figure 2.2. Enrico Forlanini demonstrating his foiler on Lake Maggiore, early 20th century [23]

During World War II and the Cold War: Hydrofoil designs have evolved over the years and undergone several design changes, from ladder to V-shaped (Fig. 2.8 and 2.9 on page 12). Military and high-speed ferries were among the first sectors to adopt hydrofoils in the design of watercraft. During World War II, hydrofoils gained popularity for military applications, such as the Canadian HMCS Bras d'Or (Fig. 1.1). Another example is the Patrol Hydrofoil Missile (PHM) class, developed by Boeing. These hydrofoil ships were designed for high speed and maneuverability, allowing them to outrun submarines and evade radar detection. By lifting out of the water, hydrofoils reduce the submerged area, thereby reducing drag and improving overall efficiency.

For commercial uses, the Supramar PT 50 (Fig. 2.3 (c)), introduced in the 1960s, and the Boeing Jetfoil 929-100 [26] (Fig. 2.3 (b)), introduced in the 1970s, were passenger ferries capable of reaching up to 42 knots using hydrofoils. These ferries offered smoother rides in rough seas, making them effective in regions like Hong Kong, Japan, and the Mediterranean.



Figure 2.3. a) Bell Hydrodome, b) Boeing Jetfoil, and c) Supramar PT 50 [23]

After the Cold War, aircraft became popular and widely accepted in commercial applications due to the speed and time savings provided. In contrast, hydrofoil watercraft did not offer economic advantages over traditional watercraft to become a mainstay of marine transportation. The complex and expensive manufacturing and high direct operation costs (DOC) from maintenance required to attain high speeds offset the benefits of speed [27]. As a result, until recent decades, there have been limited applications of hydrofoil craft, with a few exceptions, including the Boeing Jetfoil commercial ferry. However, recent technology and hydrofoil design advancements have seen their application increase across various maritime settings, including recreation and racing.

2.1.1 Current Advancements in Hydrofoil Technology

Hydrofoil technology is gradually becoming popular due to advancements in materials, design methodologies, propulsion modes, and control systems, among others. These innovations have improved the efficiency of hydrofoils while making them more accessible and versatile across multiple applications. One such application is the adoption of hydrofoils in the America's Cup challenges, a sailing competition. The move to hydrofoil watercraft in the competition has drawn attention to hydrofoils in sailing and the broader maritime industry.

The 34th America's Cup, held in San Francisco in 2013, introduced hydrofoiling AC72 catamarans (Fig. 2.4 (a)), revolutionizing yacht racing by setting speed records previously unattainable with conventional sailing vessels. In 2020, the 36th America's Cup featured the AC75 (Fig. 2.4 (b)), a fully foiling monohull class that reached speeds exceeding 55 knots [28]. The use of hydrofoils in the America's Cup accelerated research in hydrodynamics and structural optimization, impacting competitive sailing and the broader maritime industry.



Figure 2.4. America's Cup sailing hydrofoil watercraft a) AC72 [18] and b) AC75 [18]

The trend towards a more sustainable and green future has also led to the recent rise in hydrofoil technology due to the prospect it presents in designing environmentally friendly watercraft. Over the past decade, hydrofoils have transitioned into the recreational market with examples such as the hydrofoil boat (e.g. Candela C-8 (Candela, 2023)) and the foiling surfboard (also known as eFoil), which are both powered by electric motors. These adaptations lead to a more sustainable, smooth, and nearly silent ride above the water's surface. Companies such as SeaBubbles, Quadrofoil, Futuride, and Navier are pioneering the development of electric hydrofoil boats, moving closer to a greener, more sustainable marine industry.

The introduction of hydrofoil technology into both high-performance sailing and recreational watercraft markets has driven major innovations in hydrofoil design. To better appreciate these advancements, the following section examines the underlying physics principles under which hydrofoils operate.

2.2 Physics of Hydrofoils

Hydrofoils operate on the fundamental principles of fluid dynamics, similarly to aircraft wings. However, unlike aircraft, hydrofoil watercraft operate in a two-phase flow medium, which introduces complexities in the dynamic behaviour of hydrofoils [16, 29].

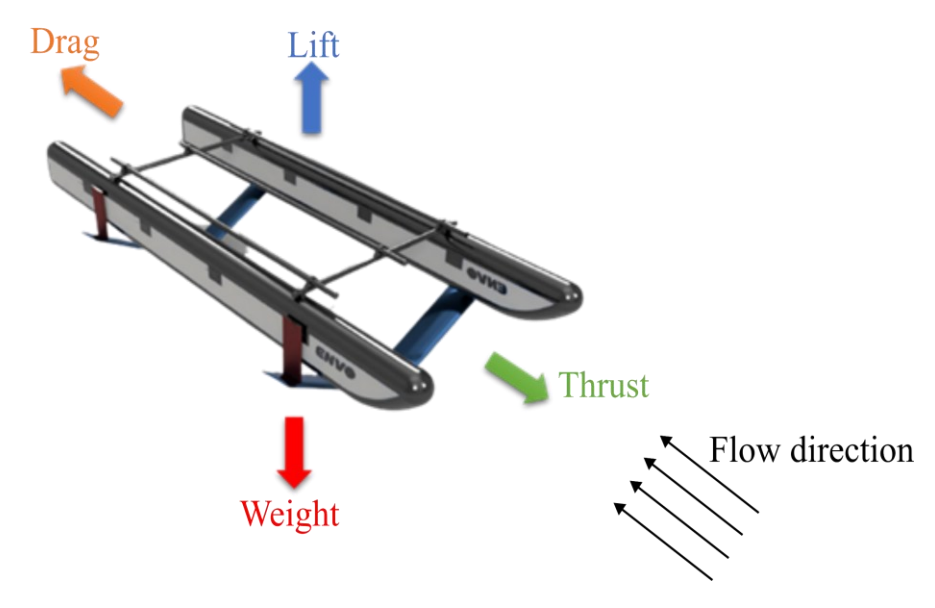


Figure 2.5. Forces acting on a hydrofoil watercraft in the foiling mode (ENVO waterbike pontoons [30])

2.2.1 Lift and Drag

Hydrofoils generate lift and drag by the interaction of the hydrofoil with the fluid medium, inducing a net force on the hydrofoil. As shown in Fig. 2.5, the lift is the component of the net force perpendicular to the flow direction. The drag is the force component in the tangential direction of the fluid flow. The lift and drag of the hydrofoil wing can be expressed mathematically as:

$$L = \frac{1}{2} \rho V^2 S C_L f(h) \tag{1}$$

$$D = \frac{1}{2} \rho \ V^2 \ S \ C_D \tag{2}$$

where:

- C_L is the lift coefficient
- C_D is the drag coefficient
- ρ is the density of fluid
- *V* is the velocity of the watercraft
- S is the reference area of the hydrofoil
- f(h) accounts for the depth-dependent corrections due to free surface effects

The lift typically increases linearly as the AoA increases. However, when the AoA reaches a critical threshold (usually 15° to 20°), the stall condition occurs [31]. Stall is when the boundary

layer separation between the fluid and the foil occurs and causes a lift reduction or a total loss of lift on the hydrofoil, leading to the watercraft crashing into the water surface. Fig. 2.6 shows typical steady characteristics of lift and drag for a general foil.

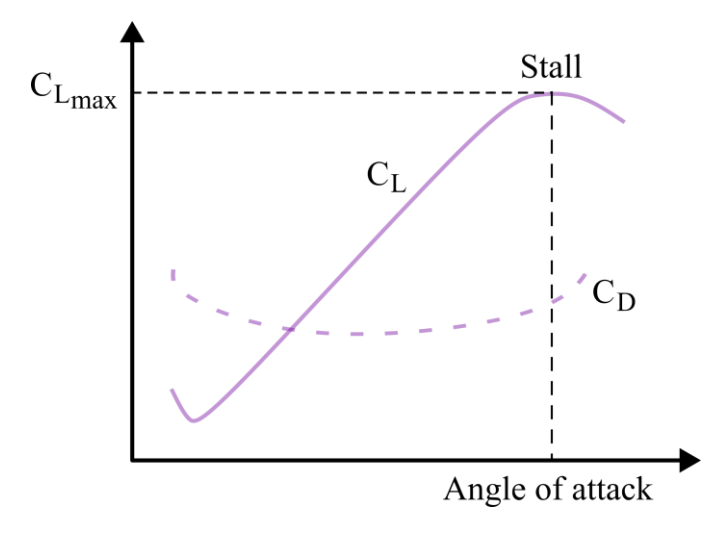


Figure 2.6. Typical lift and drag characteristics of a hydrofoil wing

Due to the nature of the two-phase flow, the operating depth influences the hydrofoil lift and drag via the free surface effect [31-33]. This effect is discussed in the next section.

2.2.2 Free Surface Effects

The free surface refers to the boundary between the air and water fluids. The hydrodynamics of hydrofoil wings are influenced when they operate close to a free surface, e.g. at a depth \leq 1.5 times the chord length of the hydrofoil. The closer a hydrofoil is to the water surface, the more significantly the free surface effect influences the generation of hydrodynamic forces (Fig. 2.7). In this thesis, the influences of submergence depths are referred to as the free surface effect. This section explains four physical effects of the free surface that affect hydrofoil stability performance, i.e. I. pressure field, II. waves, III. cavitation, and IV. ventilation.

I. Pressure field: The pressure distribution around a hydrofoil is affected by proximity to the free surface [35]. As the hydrofoil wing moves closer to the surface, the lift coefficient decreases. This reduction in lift occurs because the free surface constrains the pressure above the hydrofoil, a pressure close to the atmospheric pressure level. This constraint decreases the effective pressure difference across the hydrofoil, thereby reducing the lift. Studies have shown that this effect is particularly significant at low submergence depths

[36-38], with lift losses dependent on the submergence Froude number, F_n , which is given as:

$$F_n = \frac{U}{\sqrt{gh}} \tag{3}$$

where U is the inflow velocity, h is the submergence depth, and g is acceleration due to gravity.

II. Waves: When operating close to the free surface, a hydrofoil induces a pressure field that deforms the free surface, generating waves [10]. This wave-making effect increases drag due to energy dissipation in wave formation. This effect is minimal for deeply submerged foils, but for foils operating near the surface, the drag from the waves becomes more noticeable.

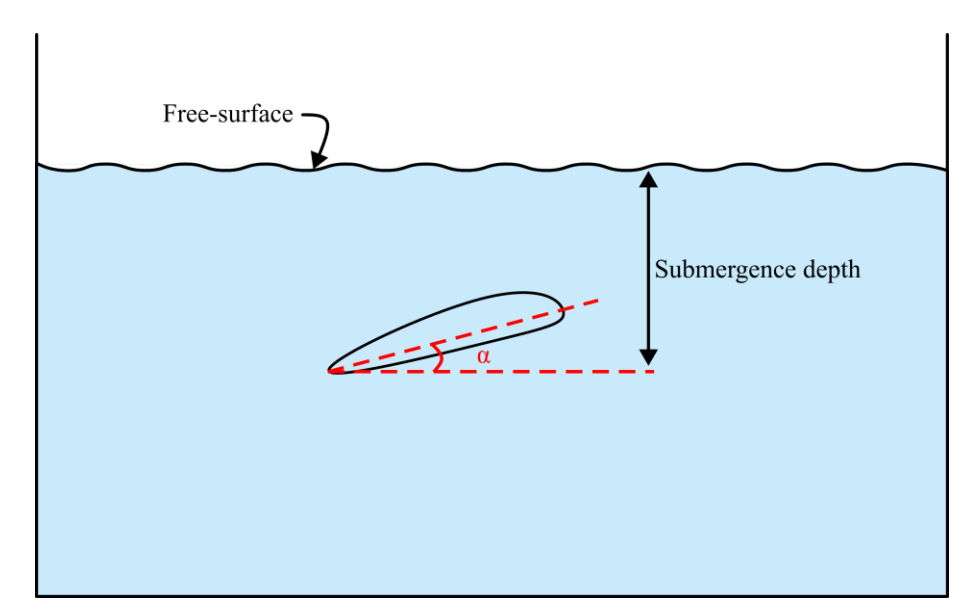


Figure 2.7. Illustration of submergence and foil AoA, α

- III. Cavitation: This occurs when the local pressure on the hydrofoil drops below the water's vapor pressure, forming vapor bubbles. This is more common near the free surface, where the pressure is lower due to air exposure and increased fluid velocity on the suction side of the foil [39].
- IV. Ventilation: When a hydrofoil operates near the free surface, the low pressure on the upper surface can drop below atmospheric pressure, drawing air down to the surface. It results in ventilation, where air pockets disrupt the lift-generating surface, reducing efficiency and increasing drag [40-41].

Free surface effects impact the stability of hydrofoils by altering pressure distributions and flow conditions as the hydrofoil operates near the water surface. These changes impact lift efficiency and increase drag, which can cause instability in riding height, as well as pitch (i.e. bow-up and bow-down motions of the hydrofoil watercraft) [32-33].

2.3 Hydrofoil Configurations

Hydrofoil layouts are traditionally classified by three methods: Method I. is based on the interaction with the water surface (e.g. surface-piercing or fully submerged); Method II. Is based on the relative positioning of the lifting surfaces (e.g. conventional, canard, or tandem); and Method III. is based on the lateral arrangement of wings (e.g. split or non-split).

I. Interaction with the water surface: Hydrofoils can be categorised as surface-piercing and fully submerged hydrofoils as shown in Fig. 2.8. Surface-piercing hydrofoils extend partially above the water, generating lift that varies with the depth of submersion [42]. The submersion depth self-adjusts with the speed of the watercraft. This variation in lift and submersion depth can contribute to inherent stability in pitch, heave (i.e. vertical movement), and roll, reducing the need for active ride control. However, surface-piercing hydrofoils are susceptible to free surface effects due to interaction with the free surface [43]. In contrast, fully submerged hydrofoils remain entirely underwater at all times, providing more consistent lift and minimizing the effects of wave action. While fully submerged hydrofoils offer greater efficiency and comfort, they require an active control system to maintain stability in altitude and attitude [29].

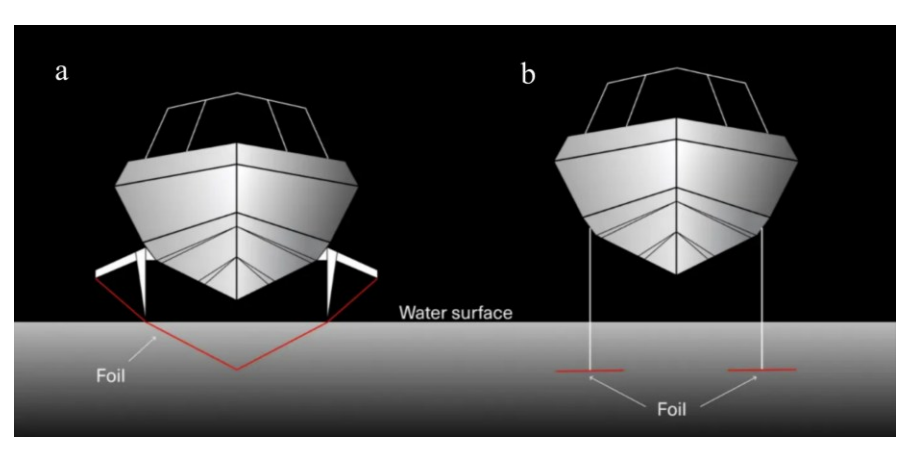


Figure 2.8. Two main types of lifting hydrofoils: a) Surface-piercing hydrofoil and b) Fully submerged hydrofoil [24]

II. Relative positioning of the lifting surfaces: In the conventional configuration, the forward wing supports the majority of the vessel's weight. A rear mounted tail is added to provide stability, trim, and control. The increased moment arm of the tail creates restoring pitching moments for the configuration, improving the pitch stability. In contrast, the canard configuration has the tail at the fore of the watercraft, to serve mainly as a control and stabilizing element, with the majority of the watercraft's weight supported by the rear wing. Because the bow of a watercraft is more exposed to the incoming waves, the canard layout with a smaller front foil minimizes the impact of wave disturbances on the overall watercraft stability. Lastly, the tandem configuration consists of two identically sized wings, which contribute an identical lift force to the watercraft to support the weight [29] as shown in Fig. 2.9. This configuration is less pitch stable as there is no dedicated control surface.

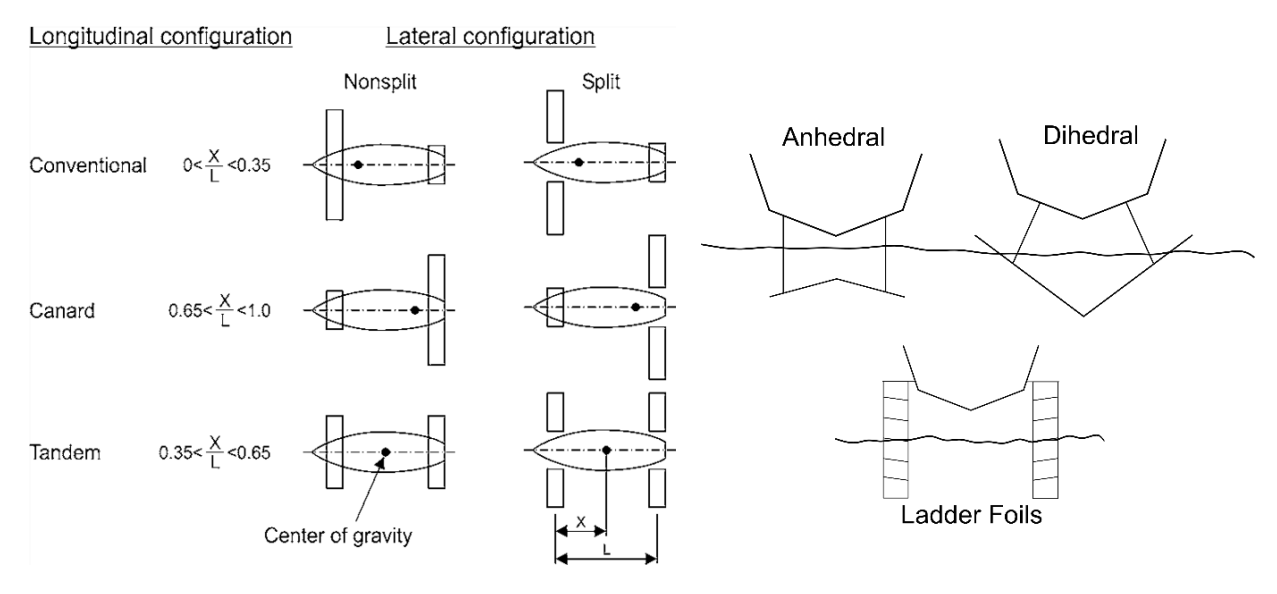


Figure 2.9. Foil layouts [44]

III. Lateral arrangement of the lifting surfaces: Split foils separate the wings to improve hydrodynamic efficiency by reducing interference drag, hence making them suitable for performance-oriented hydrofoil designs [23]. In a split foil layout, the distance between the foils can be adjusted to improve lateral stability. The greater the lateral foil distance, the greater the roll restoring moments under a roll disturbance. Each foil can also be configured with a different geometry, such as dihedral angles, to tailor the stability characteristics. Wings of non-split foils, on the other hand, maintain a continuous structure for simplicity as seen in Fig. 2.9. Non-split foils are often preferred in applications prioritizing robustness and ease of

manufacturing, as they reduce mechanical complexity and maintenance requirements. The stability of non-split foils will mainly depend on the overall wing geometry and control surfaces. As non-split foils are symmetric about the center of the watercraft, non-split foils may tend to react uniformly to changes, when compared to split foils, reducing the overall restoring tendency.

By combining these three classification methods, interaction with the water surface (surface-piercing or fully submerged), tail location (conventional, canard, or tandem), and foil structure (split or non-split), a total of twelve possible hydrofoil configurations emerge ($2 \times 3 \times 2 = 12$). A detailed summary of these configurations is presented in Appendix A.

2.4 Hydrofoil Motions

Hydrofoil watercraft operate in six degrees of freedom (DoF), across three axes, which are comprised of heave/sinkage, trim/pitch, roll, sway, surge, and yaw, as shown in Fig. 2.10. For simplicity, this section focuses on introducing four of these motions:

- I. Heave/Sinkage (vertical displacement): refers to the vertical movement of the hydrofoil watercraft, indicating submergence depth of the hydrofoil.
- II. Trim/Pitch (rotation about the lateral axis): refers to the angular displacement of the hydrofoil watercraft in a bow up or bow down motion about the lateral axis.
- III. Roll (rotation about the longitudinal axis): refers to the side-to-side rotation about the longitudinal axis.
- IV. Yaw (rotation about the directional axis): refers to the rotation of the hydrofoil watercraft about the vertical axis, which results in a change to the watercraft heading.

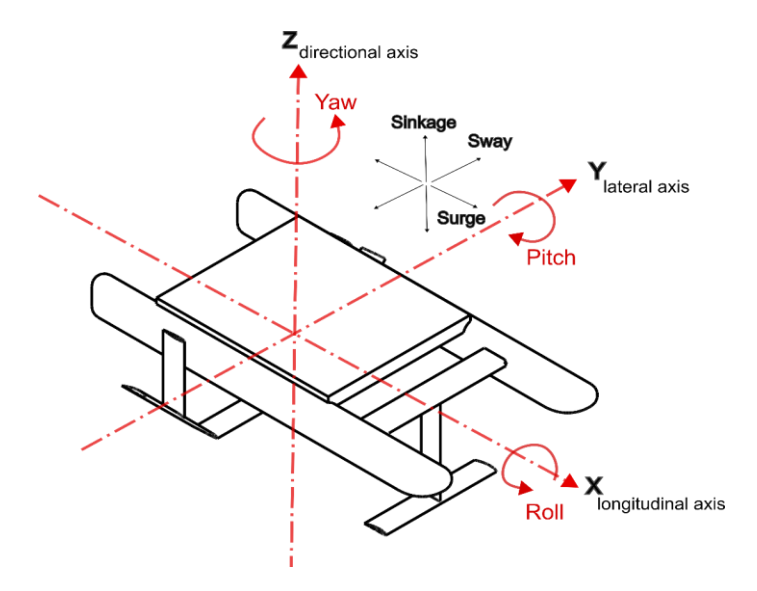


Figure 2.10. Hydrofoil motion

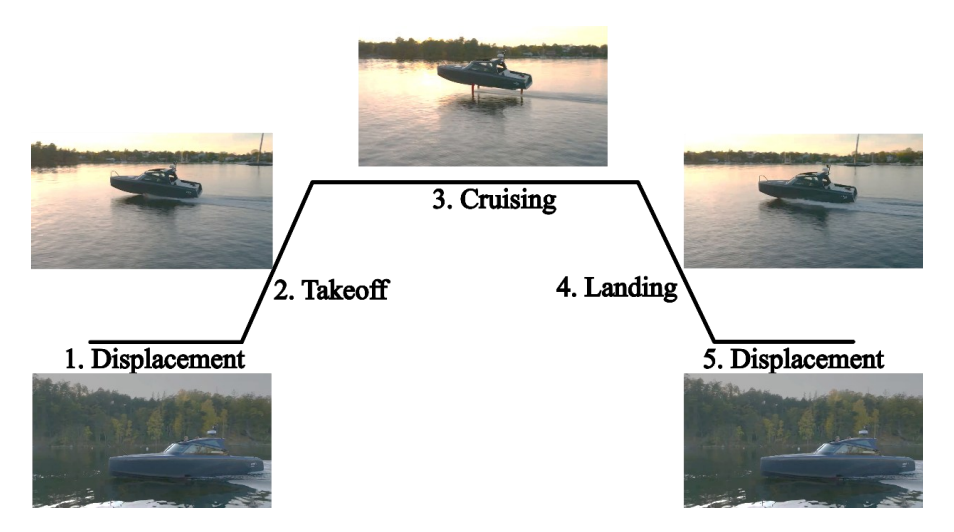


Figure 2.11. Hydrofoil mission profile [45]

Equations of Motion (EOM) govern the hydrofoil's dynamic behaviour. EOM consists of forces and moments on the left-hand side (LHS) of the equations and the vessel's response to the aforementioned forces and moments on the right-hand side (RHS) of the equations [46]. The stability of a hydrofoil is determined by its response to disturbances in the environment, which can be analyzed through its dynamic motion. The variables in the EOM form the foundation for hydrofoil stability analysis, influencing the hydrofoil watercraft's ability to maintain a steady equilibrium cruising state and maneuver efficiently throughout different phases of operation (Fig. 2.11). The EOM can be expressed in the form of a state vector, which will be introduced in the following section.

2.4.1 State Vector

The dynamic behaviour of a hydrofoil watercraft can be described using the state vector, $S(t) = \{x \ y \ z \ \phi \ \theta \ \psi \ u \ v \ w \ p \ q \ r\}^T$ (superscript T indicates the transpose of a matrix). This state vector contains twelve variables that change over time as the hydrofoil moves through the water, influenced by external forces such as hydrodynamic lift, drag, and disturbances. The state vector can be divided into four sections as detailed below.

- I. Position vector: defines the absolute position of the hydrofoil in the global reference frame. The three components, x, y, and z, correspond to the spatial coordinates in a Cartesian coordinate system.
- II. Euler angles: describe the hydrofoil's orientation relative to the global reference frame:
 - Roll (ϕ): Rotation about the longitudinal (x) axis.
 - Pitch (θ) : Rotation about the transverse (y) axis.
 - Yaw (ψ) : Rotation about the vertical (z) axis.
- III. Translational velocities: defines the motion velocities of the hydrofoil along three axes:
 - Surge (*u*): Forward velocity along the x axis.
 - Sway (v): Lateral velocity along the y axis.
 - Heave (w): Vertical velocity along the z axis.
- IV. Angular velocities: captures the rate of change of the hydrofoil's orientation over time:
 - Roll rate (p): The rate of rotation about the x axis.
 - Pitch rate (q): The rate of rotation about the y axis.
 - Yaw rate (r): The rate of rotation about the z axis.

The next section examines hydrofoil stability in literature, which focuses on assessing how these variables respond to small disturbances and identifying the conditions that allow the hydrofoil to return to equilibrium or lead it to instability [41, 44, 46-48].

2.5 Hydrofoil Stability

Stability in hydrofoils refers to a hydrofoil watercraft's return to its original equilibrium position after external disturbances without requiring the operator's proactive correction. Small perturbations

include waves, wind gusts, and sudden changes in velocity. Several factors influence hydrofoil stability, including foil geometry and layout [50], CG positioning [51], and proximity to the free surface [52], which impacts the hydrodynamic interactions with the surrounding fluid.

Hydrofoil stability can be grouped into three primary categories:

- I. longitudinal stability (pitch).
- II. lateral stability (roll).
- III. directional stability (yaw).

Additionally, stability can also be classified as follows:

- I. positive, where the hydrofoil watercraft returns to equilibrium after a disturbance.
- II. neutral, where it remains in the new position after a disturbance.
- III. negative, where the hydrofoil watercraft moves further away from the equilibrium position after a disturbance, rather than returning to it.

Longitudinal stability ensures that a hydrofoil vessel restores or maintains a consistent AoA when it experiences disturbances, such as waves or sudden load shifts. The arrangement of the hydrofoils relative to the CG determines whether the vessel exhibits positive, neutral, or negative longitudinal stability. For a hydrofoil watercraft to be considered longitudinally stable, the pitching moment coefficient should be negative, i.e. $C_{m_{\alpha}} < 0$, which is adopted from the aircraft convention for defining longitudinal stability. This means that when the hydrofoil AoA increases, it generates a negative moment to restore the hydrofoil to its original position. Figure 2.12 provides a visual comparison of stable hydrofoil longitudinal stability, where the green line indicates a stable configuration.

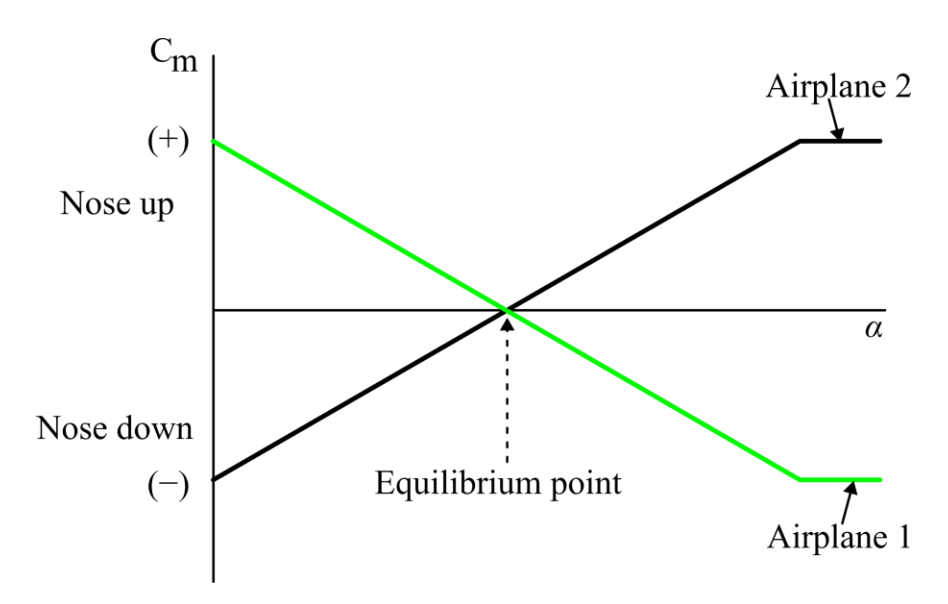


Figure 2.12. Aircraft (hydrofoil) longitudinal stability [53]

A hydrofoil with lateral stability will tend to return to its original orientation after being disturbed. Lateral stability analysis determines the degree to which a hydrofoil resists rolling due to disturbances such as side winds, waves, or unbalanced loading. When the roll moment coefficient (C_l) is negative with respect to the roll angle ϕ , i.e. $C_{l_{\phi}} < 0$, the hydrofoil is lateral stabile. Similarly, the yaw moment coefficient (C_n) governs the hydrofoil's directional stability. A negative $C_{n_{\psi}}$ ensures that the hydrofoil resists yawing disturbances and restores the vessel to its desired heading.

2.6 Stability Derivatives

The hydrofoil watercraft's reaction to small perturbations around equilibrium position can be expressed using stability derivatives. The stability derivatives are coefficients that quantify how the forces and moments acting on the hydrofoil watercraft change in response to small variations in the state variables such as rotations, velocity, pitch rate, or heave displacement. The small perturbations from the equilibrium state are analyzed using a linearized model, in which first-order stability derivatives represent the restoring forces and moments. The force and moment changes can be expressed as $\Delta F = \frac{\partial F}{\partial \xi} \Delta \xi$ and $\Delta M = \frac{\partial M}{\partial \xi} \Delta \xi$, where ξ is the state variable (e.g. pitch angle θ and pitch rate q). The partial derivatives $\frac{\partial F}{\partial \xi}$ and $\frac{\partial M}{\partial \xi}$ form the stability derivatives, which determine the tendency of the hydrofoil watercraft to restore stability or amplify the perturbation from the added disturbance. The stability derivatives to be considered in this thesis are summarized in Table 2.1.

Table 2.1. Stability derivatives

Derivative	Representation	Definition
$M_{ heta}$	$\frac{\partial M}{\partial \theta}$	Pitch moment induced by pitch perturbation
$L_{ heta}$	$rac{\partial L_{roll}}{\partial heta}$	Roll moment induced by pitch perturbation
$N_{ heta}$	$rac{\partial L_{roll}}{\partial heta}$	Yaw moment induced by pitch perturbation
M_ϕ	$rac{\partial M}{\partial \phi}$	Pitch moment induced by roll perturbation
L_{ϕ}	$rac{\partial L_{roll}}{\partial \phi}$	Roll moment induced by roll perturbation
N_ϕ	$rac{\partial N}{\partial \phi}$	Yaw moment induced by roll perturbation
M_{ψ}	$\frac{\partial M}{\partial \psi}$	Pitch moment induced by yaw perturbation
L_{ψ}	$rac{\partial L_{roll}}{\partial \psi}$	Roll moment induced by yaw perturbation
N_{ψ}	$rac{\partial N}{\partial \psi}$	Yaw moment induced by yaw perturbation

2.6.1 Stability Derivatives for Hydrofoil Stability Analysis

Stability derivatives have been used in previous studies in hydrofoil stability analysis to quantify the sensitivity of the vessel to disturbances [41, 46, 47, 53-56]. The work of Straub et al. create a linkage between the stability derivatives and the asymmetric lift and moment variations from perturbations. Three major conditions for stability derivatives are considered:

- I. Negative stability derivatives imply the tendency of the hydrofoil watercraft to generate restoring moments to return to the equilibrium position, i.e. $\frac{\partial M}{\partial \theta} < 0$.
- II. Neutral derivatives, i.e. $\frac{\partial M}{\partial \theta} = \theta$, imply the tendency of the hydrofoil watercraft to remain in a new position after a disturbance.
- III. Positive derivatives, i.e. $\frac{\partial M}{\partial \theta} > 0$, imply that the hydrofoil watercraft tends towards instability or oscillations.

2.7 Wing Dihedrals

Dihedral angles are the angle of hydrofoil wings with respect to the horizontal plane, as shown in Fig. 1.2. Analogous to aircraft design, hydrofoils with dihedrals introduce restoring forces and moments in response to roll and yaw disturbances, thereby contributing to passive stability.

Hydrofoils experience different magnitudes of heave and pitch motions at various AoA, high-lighting that the hydrofoil's orientation affects its dynamic response in waves [8]. Straub et al. [57] analytically compared two hydrofoil configurations, one with a dihedral fore wing and straight aft wing, and another with dihedral wings both fore and aft. The study found that the configuration with dihedral foils both fore and aft exhibits improved stability in regular wave conditions. Although these studies [8, 57] do not directly address the effects of dihedral angles on hydrofoil dynamic stability in turbulent or high-wave environments, they express the significance and potential of hydrofoil configuration and orientation in determining dynamic stability. A summary of related literature is provided in Tables 2.2 and 2.3. Existing literature on the stability implications of dihedral wings, especially high dihedral wings, is limited. Further research on the stability analysis, especially the impact of high dihedral angles, is beneficial to fill this knowledge gap.

Table 2.2 Summary of related literature with surface-piercing hydrofoils

Publica- tion	Study Scope	Methodology	Dihedral Stability Angles pects A Considered dressed	Stability Aspects Addressed	Research Outcome	Identified Gaps
Brizzolara et al. [110]	Performance of negative Brizzolara dihedral surface-piercing et al. [110] hydrofoil on unmanned surface vessel (USV)	Experimental and CFD	40°	Pitch and heave	Design methodology for USV surface-pierc- ing hydrofoils	No analysis of the effects of di- hedral angles on stability
Buermann [37]	Buermann Practicality of hydrofoil- [37] supported craft	Analytical review	Not speci- fied	General sta- bility	Size and speed limits for hydrofoil water-craft	No specific analysis of dihedral angles
Faison [111]	Incorporation of cambered step surface-piercing hydrofoils to high-speed planing hull	Analytical and CFD	30°	Trim and general stability at high speeds	Demonstrated benefits of combining stepped hulls with surface- piercing hydrofoils	No specific analysis of dihedral angles
Fridsma [112]	Ventilation inception on surface-piercing dihedral mental hydrofoils	Analytical and Experi- mental	30°	Ventilation phenomena	Ventilation characteristics of dihedral hydrofoils	No specific analysis of the effects of dihedral angles on stability
Masuyama [42], [54]	Masuyama stability analysis of hy- [42], [54] drofoil sailing boats	Analytical modeling	Not speci- fied	Sway, yaw, roll, and surge	Analyzed stability with dihedral front foils and inverted 'T' rear foil	Specific dihedral angles and their quantitative effects not detailed
Matveev et al. [41]	Air ventilation and its suppression on inclined surface-piercing hydrofoils	CFD simulations	30°	Ventilation ef- fects	Demonstrated methods No specific anal- Ventilation ef- to suppress air ventila- ysis of the effects fects tion on inclined hydro- of dihedral angles foils on stability	No specific analysis of the effects of dihedral angles on stability

Table 2.3 Summary of related literature with surface-piercing hydrofoils continuation

Publication	Publication Study Scope	Methodology	Dihedral Stability Angles pects Ac Considered dressed	y As- d-	Research Out- come	Identified Gaps
Perali et al. [36]	Performance prediction of Perali et al. hydrofoils near free surface using BEM and RANS methods	CFD simulations (BEM and RANS)	8.19°	Lift and drag performance	Validated low-fi- Lift and drag delity BEM for hy- performance drofoil perfor- mance	Validated low-fi- No specific analysis Lift and drag delity BEM for hy- of the effects of dihe- performance drofoil perfor- dral angles on stabil- mance ity
Rothblum [113]	Methods of delaying and controlling ventilation on surface-piercing struts	Experimental study	Not speci- fied	Ventilation	Investigated techniques to delay and control ventilation	No specific analysis of the effects of dihedral angles on stability
Straub et al. [58]	Straub et al. Analysis of dihedral hy- [58] drofoils	Experimental and the- 0° - 60° oretical analysis	°00 - °0	Lift, drag, and flow sep- aration	Theory for hydro- foil trailing vortex drag Large dihedral an- gles can suppress flow separation	No direct study on the dihedral effect on roll, pitch and yaw stability
Vernengo et al. [38]	Vernengo et loaded supercavitating hyal. [38] drofoils	Computational optimization using viscous lifting line method	5° - 20°	Lift distribu- tion	Framework for designing supercavitating hydrofoils	No specific analysis of the effects of dihedral angles on stability
Wetzel [114]	Ventilation scale effects on hydrofoils	Experimental	15° - 60°	Ventilation phenomena	Effect of ventila- tion on hydrofoil center of pressure	No specific analysis of the effects of dihedral angles on stability

2.8 Current State of Hydrofoil Analysis Methods

Early work in hydrofoil stability, such as that by Straub et al. [58] and Tahara et al. [59], relied heavily on experimental approaches and linear analytical models to investigate the hydrofoils' response to perturbations. Other studies used towing tanks and wind tunnels to investigate scale models to establish the concepts of hydrofoil behaviour [56]. For example, Souppez et al. performed experimental investigations on three hydrofoil-assisted racing monohull configurations and found that, although hydrofoils improved righting moments, they introduced drag penalties [60]. These experiments highlight the trade-offs between performance and stability for hydrofoil watercraft. While effective for later design stages, experimental studies are often constrained by cost and complexity, especially when exploring new and unconventional designs such as hybrid designs of surface-piercing and fully submerged hydrofoils [61-62].

Similar to experiments, analytical methods have continued to offer theoretical insights through linearized equations of motion [42, 54]. Several more recent studies have contributed to the modeling of hydrofoil stability [48, 63-64]. Hansen et al. [69] developed a dynamic velocity prediction program (DVPP) for the AC50 class, combining physics-based forces, CFD-derived data, and experimental results to simulate foil configurations and maneuvers [63]. Although the study provided valuable insights into dynamic control, there is limited detail on the analytical methodology and the focus was more on performance outcomes than on the stability mechanisms of hydrofoil watercraft.

The advancement in computing power has seen hydrofoil analysis transition from experimental and linear analytical methods to CFD-driven approaches. Schouten et al. [70] performed a stability analysis using force and torque balance to derive dynamic equations of motion for a solar-powered foiling craft [64]. Their findings detail how the hydrofoil aspect ratio and CG position influence the overall hydrofoil system stability. Horel et al. [3] proposed a system-based modelling approach that accounts for various Froude numbers and hydrofoil shapes in calm water and wave conditions, which relied on CFD-derived coefficients. Haase et al. [65] showed the role of hydrofoils in resistance reduction for catamarans using CFD, reiterating the use of CFD in current hydrofoil design and analysis.

The advancement of CFD has enabled detailed, relatively cost-effective simulation of multiphase flow and complex interactions between hydrofoils and the surrounding water and air [62-67], compared to experimental methods. Previously reported literature by Bague et al. [46] and Ploe [72] have

shown the accuracy of CFD in assessing hydrofoil performance and dynamic behaviour, especially during the early design process. The accuracy of the CFD data is also influenced by how the turbulence is modelled. The choice of turbulence model determines how the unsteady hydrodynamic behaviours of the hydrofoil are captured, especially considering surface piercing hydrofoils, free-surface interaction, and ventilation effects. The flow around a hydrofoil is generally turbulent due to high Reynolds numbers and pressure changes resulting from the hydrofoil's geometry. Several models are available to capture turbulence in CFD simulations, including the RANS standard k- ϵ model. The k- ϵ model is widely used in free-surface multiphase simulations due to its robustness, computational efficiency, and well-validated performance in external flows [8, 11]. The model solves the transport equations for the turbulent kinetic energy (k) and its dissipation rate (ϵ), making it suitable for steady and mildly unsteady flows. While it may underpredict separation in highly adverse pressure gradients, its stability in Volume of Fluid (VOF)-based multiphase applications has led to its adoption in many marine and hydrofoil studies [8, 11, 41, 62].

Independent studies also support the suitability of the k-ε model in hydrofoil modelling. Raza et al. [73] conducted RANS-based simulations of a submerged hydrofoil near the free surface using the standard k-ε model, capturing free-surface wave deformation and lift reduction near the Froude hump region. Kim et al. [74] analyzed a hybrid method combining URANS and LES for simulating turbulent free-surface flows around surface-piercing bodies. Their study showed improved predictions of free-surface deformation and wake structures compared to traditional RANS models, highlighting the balance between accuracy and computational cost.

While hybrid models and LES approaches offer improved resolution of unsteady wake dynamics, they are often prohibitively expensive for full-scale parametric studies such as dihedral variation. Therefore, many CFD-based design-stage studies, including this thesis, opt for standard k-ε or SST k-ω models to achieve an acceptable compromise between cost and accuracy.

Studies that apply CFD for the hydrofoil design, as well as performance analysis and optimization, exist in literature [75-77]. In terms of stability, the influence of the hydrofoil geometric parameters, including the span, chord length, and AoA, have been investigated for both fully submerged and surface-piercing hydrofoils [78-81]. However, some geometrical parameters, such as the dihedral angles, have not been thoroughly investigated for their effect on hydrofoil stability. Straub and Tinney [58] investigated the performance of dihedral angles through experimental and analytical

methods in 1957, however, did not directly address the stability effects. Since then, there has been little effort to explore the effects of the dihedral angle on hydrofoil stability. Thus, the influence of high dihedral angles on the stability of hydrofoils presents an area that needs further study.

2.9 Research Gap

Despite hydrofoil stability having been treated at great length in literature, further research is necessary to fully understand the contribution of wings with high dihedral angles (30° - 50°) to stability across all three axes, i.e. longitudinal (pitch), lateral (roll), and directional (yaw). Studies, such as those of Bague et al. [46], reported that increasing dihedral angles may improve hydrofoil stability, especially in rough sea conditions. However, the direct impact of high dihedral angles on stability has not been investigated. This gap becomes more significant in the context of surface-piercing hydrofoils, where dihedral wings interact directly with the free surface [16, 82-84]. Such interactions introduce coupling in the stability derivatives [47, 56, 85-86]. For example, a yaw disturbance could induce a roll moment due to the asymmetric immersion of dihedral hydrofoils, while variations in wetted surface area caused by wave interaction further complicate the dynamics [55, 57]. The rollpitch and roll-yaw interactions generated by asymmetric submersion on two different sides of dihedral wings make the analysis complex. Doversusky et al. [52] investigated surface proximity effects on hydrofoils but did not explore how this interacts with the dihedral geometry. The work of Kaplan et al. [87] on tandem hydrofoils and Labi et al. [60] on racing yachts also explores hydrofoil-induced dynamic effects, but their studies were configuration-specific and did not discuss high dihedral hydrofoils.

This thesis aims to bridge the gap in hydrofoil literature by studying the impact of high dihedral angles (30° - 50°) on the longitudinal, lateral, and directional stabilities of a canard configuration hydrofoil watercraft. The objective of this research is to develop a multiphase CFD simulation framework to capture the nonlinear, multiphase interactions that occur as the hydrofoil pierces the water surface.

As hydrofoil applications extend to low-speed recreational electric watercraft, the need for low-cost passive stability increases. High dihedral angles offer the potential to enhance passive stability, reduce the risk of uncontrolled motions, and improve safety, especially under unsteady or rough sea conditions.

2.10 Objectives

To address existing knowledge gaps, this thesis aims to analyze the performance of hydrofoil watercraft through:

- I. Select the hydrofoil configuration using a conceptual design approach to meet the design requirements provided by the industrial customer.
- II. Develop a multiphase CFD simulation framework with the help of Star-CCM+ software to assess the performance of hydrofoils, such as hydrodynamic forces and moments, in foiling mode with disturbance.
- III. Investigating the influence of high dihedral angles between 30° and 50° on pitch, roll, yaw, and coupled stability using stability derivatives on a canard-configured hydrofoil watercraft.

Chapter 3: Methodology

This chapter outlines the methodology used to investigate the stability effects of high-dihedral hydrofoil wing configurations on a hydrofoil watercraft. The methodology integrates hydrofoil design principles, CFD, and stability derivative extraction.

3.1 Nomenclature and Axis Convention

The signs and naming conventions of the hydrofoil watercraft are borrowed from both aircraft and watercraft design. As shown in Fig. 3.1, the hull represents the frame or body of the watercraft in contact with the water surface during the floating mode, and the deck is the top, relatively flat covering of the hull. The bow refers to the front part of the watercraft, and the stern refers to the rear end. The wing refers to the hydrofoils on the watercraft, and the struts are the connections between the wings and the hull.

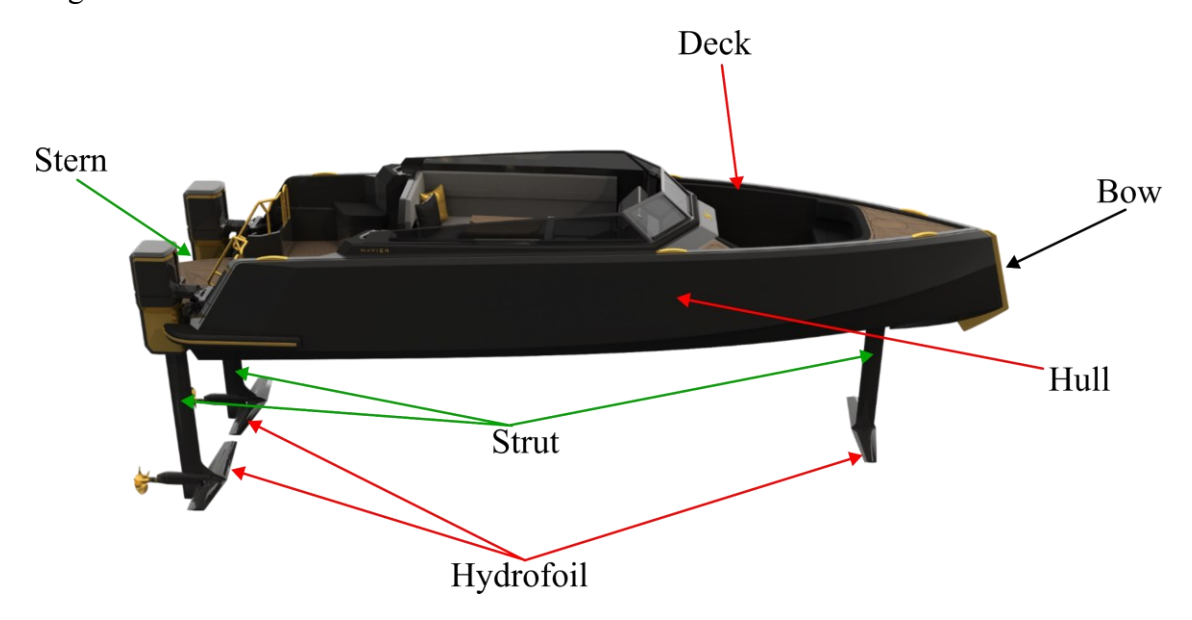


Figure 3.1. Illustrates the naming convention of major components of a hydrofoil watercraft using the Navier N30 model [88]

The axis conventions used in this thesis are defined as follows. The longitudinal axis (x-axis) extends from the bow to the stern. The lateral axis (y-axis) runs from side to side, perpendicular to the longitudinal axis. The vertical axis (z-axis) runs vertically through the watercraft, aligned with the CG. The rotational motions are defined using aircraft terminology, and the translational motions

are defined using marine terminology. The axis convention, as well as the motions, are shown in Fig. 2.10.

3.2 Hydrofoil Layout Selection

This section outlines the design requirements provided by the industrial customer, ENVO, and the selection of the hydrofoil layout in this thesis qualitatively through literature and quantitatively through simulation results.

3.2.1 Design Requirements

The hydrofoil was designed with the goal of meeting or exceeding the performance of a low-speed single-passenger electric recreational watercraft capable of foiling solely on human power. Design requirements are outlined in Table 3.1.

Table 3.1. Design requirements

Requirement ID	Requirement	Goal
R1	Max Power	1500 W
R2	Max Speed	20 km/h
R3	Range	1 Hour
R4	Battery Capacity	800 Wh
R5	Stability	Self-stabilizing
R6	Max weight	120 kg
R 7	Takeoff Speed	7 km/h

3.2.2 Benchmarking and Configuration Analysis

The benchmarking process involved evaluating notable recreational watercraft that accommodate fewer than 11 passengers to highlight the market positioning. Figure 3.2 shows the benchmarks and existing hydrofoil watercraft in this range of performance.

Three hydrofoil layouts were selected from literature review and benchmarking: I) Hybrid layout with fully submerged canard and surface-piercing main wing, II) Surface-piercing Tandem layout,

and III) Surface-piercing Canard layout, which will be referred to as "Configuration a", "Configuration b", and "Configuration c", respectively. The layout selection focused on layouts that achieved static and dynamic stability through passive control rather than active control systems.

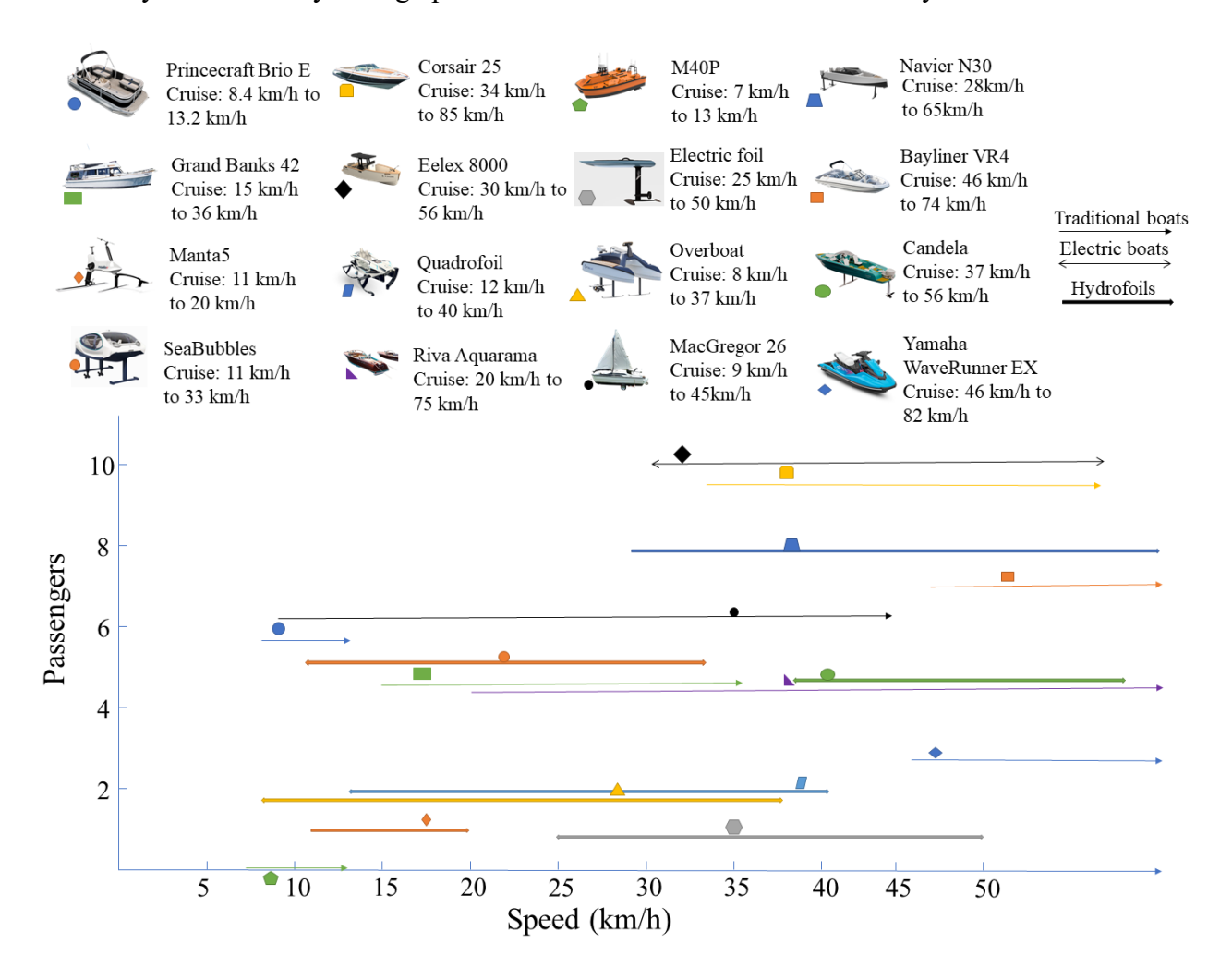


Figure 3.2. Notable recreational watercraft with less than 11 passengers [87-102].

The configurations shown in Fig. 3.2 were assessed based on requirements R1 to R7 listed in Table 3.1 using a decision matrix presented in Table B.1 in Appendix B. The qualitative scores were derived from literature and existing commercial hydrofoil watercraft. To further validate the qualitative design matrix, the selected layouts were modelled using 3D CAD software, OpenVSP and Autodesk Fusion 360, and a performance study was conducted to compare the lift and drag of the layouts within the speed range required by R2 and R7. The structures on the deck are approximated as a single rectangular block for simplification in the CFD simulations. Figure 3.3 shows a CAD

model in front view via Autodesk Fusion 360 Graphical User Interface. For consistency and to facilitate comparison, each configuration was modelled with identical total submerged wing area. The general dimensions for the hydrofoil watercraft are listed in Table 3.2 and the wing sizing details are provided in Appendix B.

Table 3.2. Hydrofoil watercraft parameters

Parameters	Dimensions
Hull Length	3.00 m
Hull Width	1.25 m
Hydrofoil Profile	NACA 4412
Wing Area	1.28 m^2
Wingspan	2.62 m
Wing Chord Length	0.20 m
Wing Dihedral	30° - 50°
Distance from foil to deck	0.92 m
Total Mass of Watercraft	120 kg

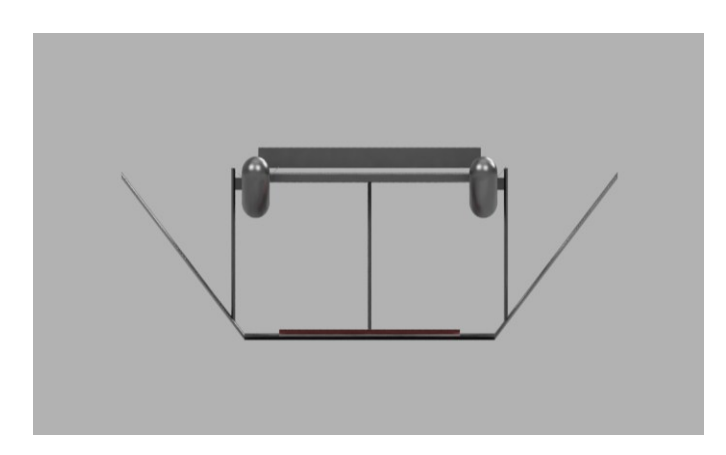


Figure 3.3. A CAD model with exaggerated wingspan for dihedral wing visualisation generated by Autodesk Fusion 360

From the simulation results, the hybrid layout with a fully submerged canard and surface-piercing dihedral main wing exhibited the best drag performance at low speeds among the aforementioned three configurations and was therefore selected in the present study. The analysis for the configurations is presented in Chapter 4 and Appendix B. The next sections present the simulation methodology and a case study.

3.3 Simulation Methodology

This chapter describes the simulation methodology applied in this study to simulate the dynamic behavior of the hydrofoil watercraft. The output of the simulation is used to derive the derivatives, which are then analyzed to evaluate the hydrofoil stability. Star-CCM+ (15.04.010-R8, Siemens), a commercial CFD software, was used for the simulation process. A full-scale model was in the simulation to estimate stability-related forces and moments. The simulation considered longitudinal, lateral, and directional motions.

3.3.1 Mesh Generation

The mesh in this study was generated using the meshing engine of the CFD software, Star-CCM+ (15.04.010-R8, Siemens). The hydrofoil watercraft was meshed as a single rigid body for simplicity.

Rigid Body Mesh

The hydrofoil watercraft is assumed to be a unified, non-deformable structure that moves as a unit. The following meshing models were used in the generation of the rigid body mesh.

- I. Surface Remesher: to accurately capture the CAD model's geometry on the watercraft's outer surface.
- II. Trimmed Cell Mesher: to generate the core volume mesh for the rigid body model.
- III. Prism Layer Mesher: applied along the boundary layers, to capture the velocity and pressure gradients close to the walls.
 - IV. Volumetric Refinements: applied to the hydrofoils and the free surface between the air and water phases.

The mesh quality was continually checked using the Mesh Quality Indicator, which includes skewness, aspect ratio, and orthogonality checking functions. The mesh was refined in critical areas, such as around the dihedral wing and canard, which are shown in Fig. 3.4. A mesh convergence study

was performed to ensure the data was independent of the mesh size as detailed in Appendix E. The flow condition setting of the simulation was set up following the generation of the mesh.

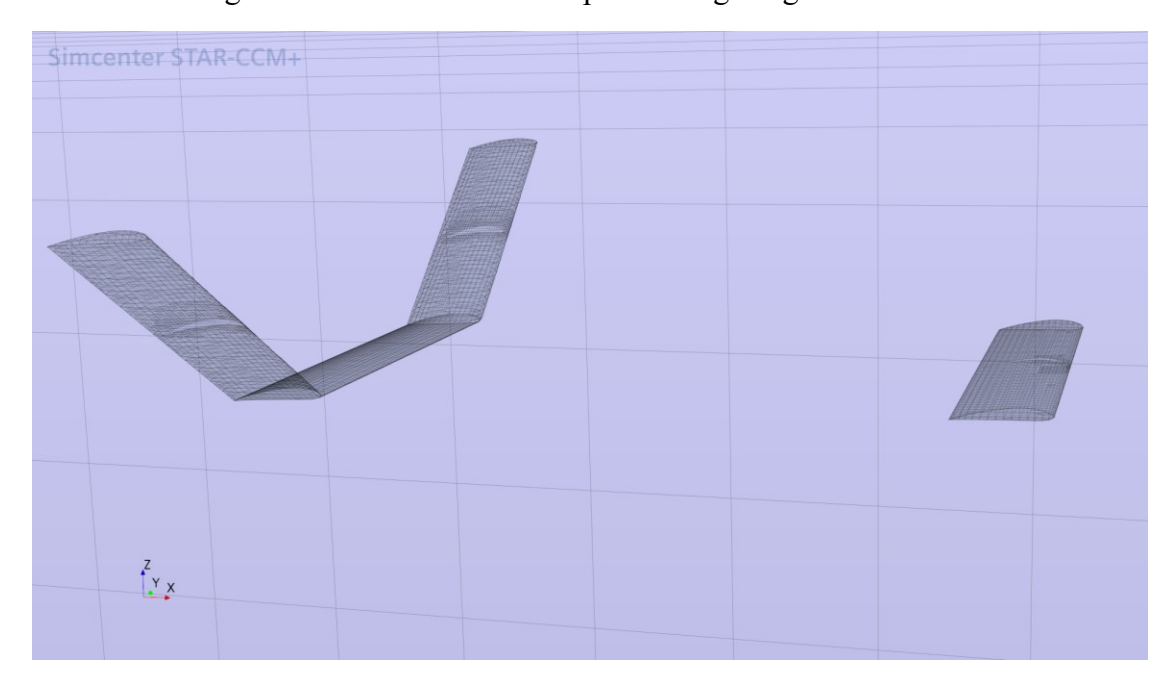


Figure 3.4. Mesh visualisation of the hydrofoils

3.3.2 Physical Models

The simulations were run with model combinations, including Multiphase, Volume of Fluid (VOF), and K-Epsilon (k-ε) turbulence models [41]. The Multiphase model captures the realistic behaviour of the hydrofoil watercraft, especially when considering foils close to the free surface and also surface-piercing hydrofoils. The VOF model was selected to provide the free surface characteristics of the environment and define the inlet velocity of the fluid in the simulations. The k-ε turbulence model was selected to minimize computational cost while maintaining accuracy in multiphase fluid simulations, given time constraints.

3.3.3 Domain and Boundary Conditions

The simulation domain was sized as a function of the typical lengths of the hydrofoil watercraft to minimize boundary effects while maintaining reasonable computational costs. The majority y+values for the boundary layer lie between 30 and 300. Figure 3.5 shows the dimensions of the domain and the simulation boundary conditions.

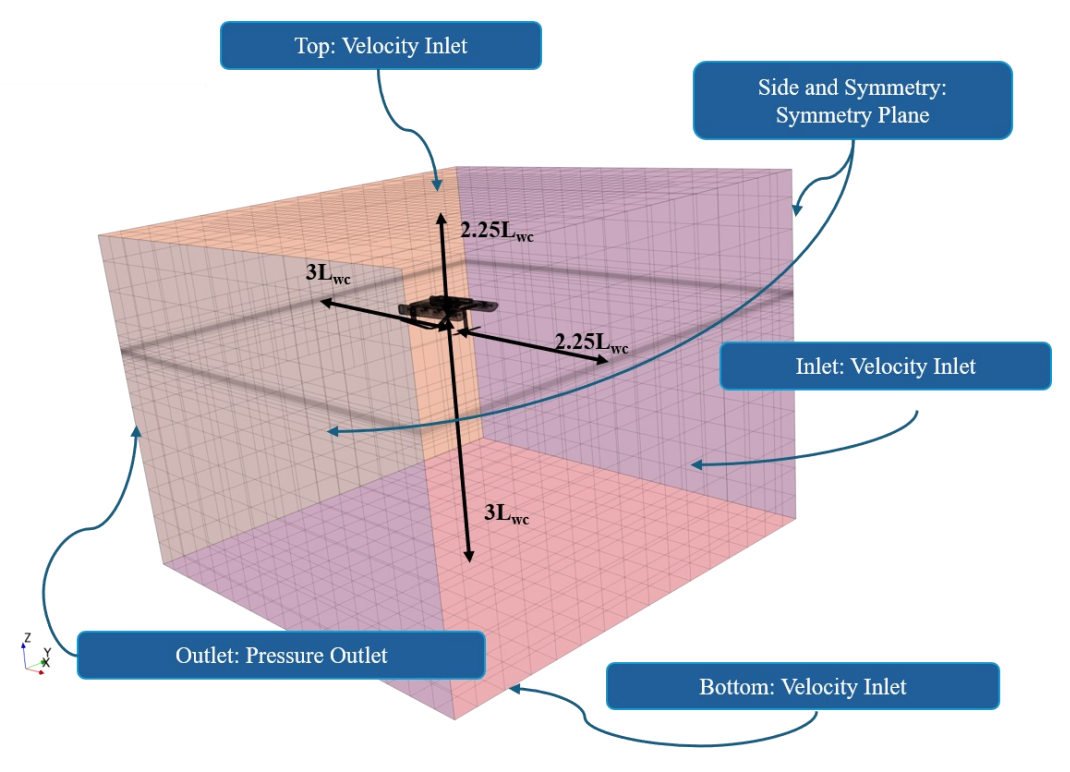


Figure 3.5. Simulation boundary conditions and domain size, where L_{wc} is the typical length of the watercraft

The boundary conditions:

- I. Inlet, Top, and Bottom: A uniform water/air velocity is applied to correspond to the simulation case.
- II. Outlet: A pressure outlet with wave damping is applied to minimize reflections.
- III. Side and Symmetry: Symmetry walls are applied to mimic wide water conditions.
- IV. Hydrofoil watercraft body: No-slip wall condition is applied for near-wall turbulence resolution.

3.3.4 Convergence Criteria

To determine the equilibrium points, the forces and moments acting on the hydrofoil system were obtained from the simulations. These forces included the lift and drag, while the moments were pitch, roll, and yaw moments. The process to simulate forces and moments is detailed below in three steps:

I. Force and Moment Calculation in Star-CCM+: The simulation captured pressure distributions by solving the Navier-Stokes equations:

$$\frac{\partial \rho}{\partial t} + \frac{\partial}{\partial x_i} (\rho u_i) = 0 \tag{4}$$

$$\frac{\partial}{\partial t}(\rho u_i) + \frac{\partial}{\partial x_j}(\rho u_i u_j) = \frac{\partial p(t)}{x_j} + \frac{\partial}{\partial x_j} \mu \left(\frac{\partial u_i}{\partial x_j} \rho \overline{u_i' u_j'}\right) + S_j$$
(5)

where ρ is the fluid density, t is time, u_i and u_j (i, j = 1, 2, 3) are the time-averaged velocity components, p(t) is the time-averaged pressure, μ is the dynamic viscosity coefficient, $\rho u_i^{\prime} u_j^{\prime}$ is the Reynolds stress term, and S_j is the source term (i.e. external forces or other phenomena that drive or influence the fluid flow). The pressure distributions were then used to compute the lift, drag, and moments on the hydrofoil watercraft.

- II. Iterative Convergence: For each configuration, the simulations were run until the forces and moments reached steady-state convergence criteria. The convergence criteria included residuals, moments, lift, and drag forces. For these criteria, thresholds between 10⁻⁴ and 10⁻⁶ were used to confirm that the results were numerically stable.
- III. Establishing Equilibrium Conditions: The equilibrium point was identified when:
 - The net force in all translational directions (X, Y, Z) was zero, indicating steady motion.
 - The net moments about the CG (pitch, roll, yaw) were approximately zero, indicating rotational stability.
 - The hydrofoil attitude does not change with time

Solver and Simulation Phases

The home-made code, containing commands written in Java coding language, allows for the automation of the multiphase solver simulation process in the CFD software. The simulation has two main phases, i.e. Phase I Dynamic Simulations: to extract the equilibrium position and record hydrofoil responses to disturbances in real time, and Phase II Static Simulations: to extract forces and moments when the hydrofoils are fixed in space at specific depths and angles.

3.4 Post-processing

In post-processing, the dynamic stability of a hydrofoil watercraft can be characterized by its response to small perturbations in motion at the equilibrium state. These responses are expressed in the form of stability derivatives. The following sections present the methodology for extracting the primary stability derivatives of a hydrofoil watercraft and how these derivatives capture the stability behaviour of a dihedral hydrofoil watercraft.

3.4.1 Extracted Output

The output extracted from the simulation includes:

- I. Hydrodynamic force-time histories of the entire watercraft as well as the individual parts such as the foils and hull.
- II. Dynamic motion responses such as the trim, sinkage, roll, yaw and sway
- III. Pressure and velocity fields on the foil surfaces
- IV. Free surface profile to visualise and analyse the wake caused by the configuration
- V. Force and moment coefficients from which the stability derivatives are calculated

3.4.2 Stability Derivatives of a Hydrofoil Watercraft

The dynamics of a hydrofoil system have six degrees of freedom, i.e. surge, sway, heave, roll, pitch, and yaw. CFD dynamic simulations identify the equilibrium positions of the hydrofoil. After adding small perturbations to the equilibrium state, the hydrofoil's dynamic responses are analyzed to calculate stability derivatives. This process can be expressed as $\Delta F = \frac{\partial F}{\partial \xi} \Delta \xi$ and $\Delta M = \frac{\partial M}{\partial \xi} \Delta \xi$ in simple terms, where ξ is the state variable, e.g. pitch angle θ . The partial derivatives $\frac{\partial F}{\partial \xi}$ and $\frac{\partial M}{\partial \xi}$ form the stability derivatives, which represent the tendency of the hydrofoil watercraft to restore or amplify the perturbation from the added disturbance. For example, a negative value of the pitching moment stability derivative, $\frac{\partial M}{\partial \theta}$, implies that a positive pitch angle generates a negative moment (i.e. restoring moment), which contributes to pitch stability. The stability derivatives to be considered in this thesis are listed in Table 2.1. The derivatives in this thesis will be expressed in the common aircraft short form, such as $C_{l_{\theta}}$ to represent $\frac{\partial C_{l}}{\partial \theta}$. The identical method will be applied to the lateral and directional stability derivatives.

3.4.3 Determination of Stability Derivatives

The derivatives are extracted from CFD simulations using the Reynolds-averaged Navier–Stokes (RANS) solver with the Volume of Fluid modeling to capture free surface effects. Figure 3.6 shows the overall process for determining the stability derivatives.

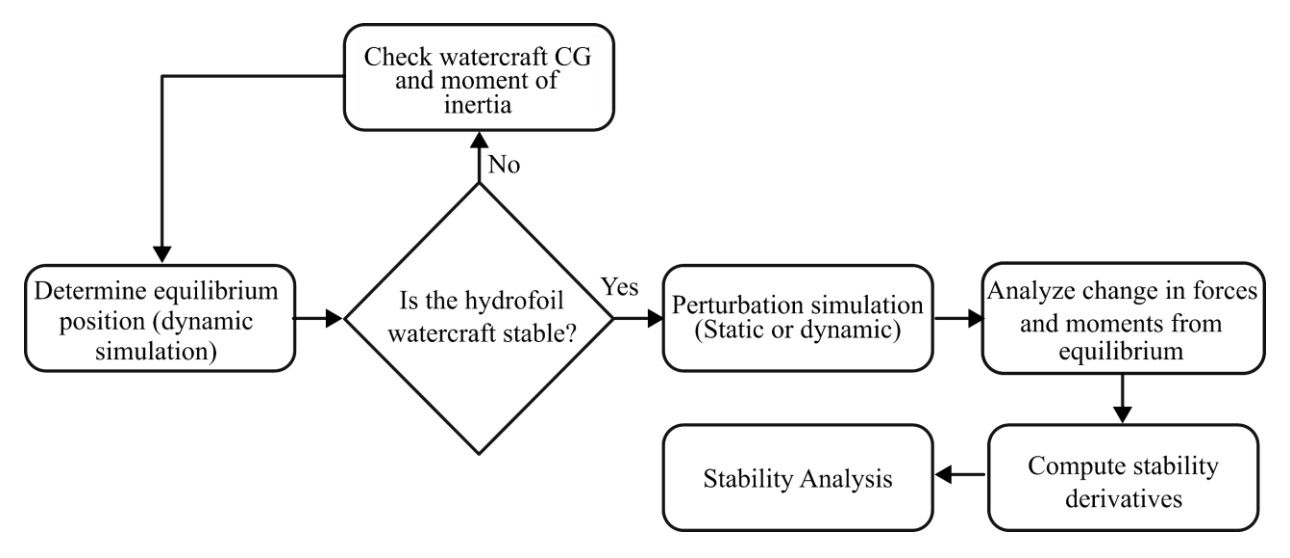


Figure 3.6. Flowchart of the stability derivative determination process

A dynamic simulation of the hydrofoil model is performed at 3 m/s cruising conditions to find the equilibrium condition, where the net forces and moments acting on the watercraft are effectively zero. This equilibrium position, including attitude and velocity, serves as the reference state for further analysis.

The following assumptions are made when finding the equilibrium state:

- I. The hydrofoil mass remains constant
- II. The hydrofoil watercraft is symmetric along all axes. i.e. $I_{xy} = I_{xz} = I_{yz} = 0$
- III. The equilibrium position is the trim state
- IV. The hydrofoil watercraft is a rigid body with no control inputs

Should the dynamic simulation fail to converge to an equilibrium state, the CG location and moment of inertia components would have to be checked and refined before proceeding. The framework can only be followed once a trim state is found.

Figures 3.7 and 3.8 show the angular changes from the equilibrium position for the calculation of the stability derivatives. These perturbations are applied as offsets about the rotational axes, such

as the pitch angle about the y-axis. For each perturbation case, new steady-state hydrodynamic forces and moments are recorded. For instance, in order to assess the pitch stability derivative, the hydrofoil is rotated 2° about its pitch axis while maintaining the new orientation fixed. The resulting hydrodynamic forces and moments are then compared against those from the unperturbed (equilibrium) case. The change of moments and forces with respect to the rotated angle from the equilibrium state represents the stability derivative. For example, the pitch moment stability derivative with respect to the change in pitch angle can be written as:

$$\frac{\partial M}{\partial \theta} \approx \frac{M(\theta + \Delta \theta) - M(\theta)}{\Delta \theta} \tag{6}$$

The resulting derivatives are nondimensionalized into coefficient form, following aircraft nondimensional coefficients [105]. The results are nondimensionalized to enable comparison, generalization and interpretation of the results across different configurations and operating conditions. This process is repeated for each derivative analyzed in this thesis.

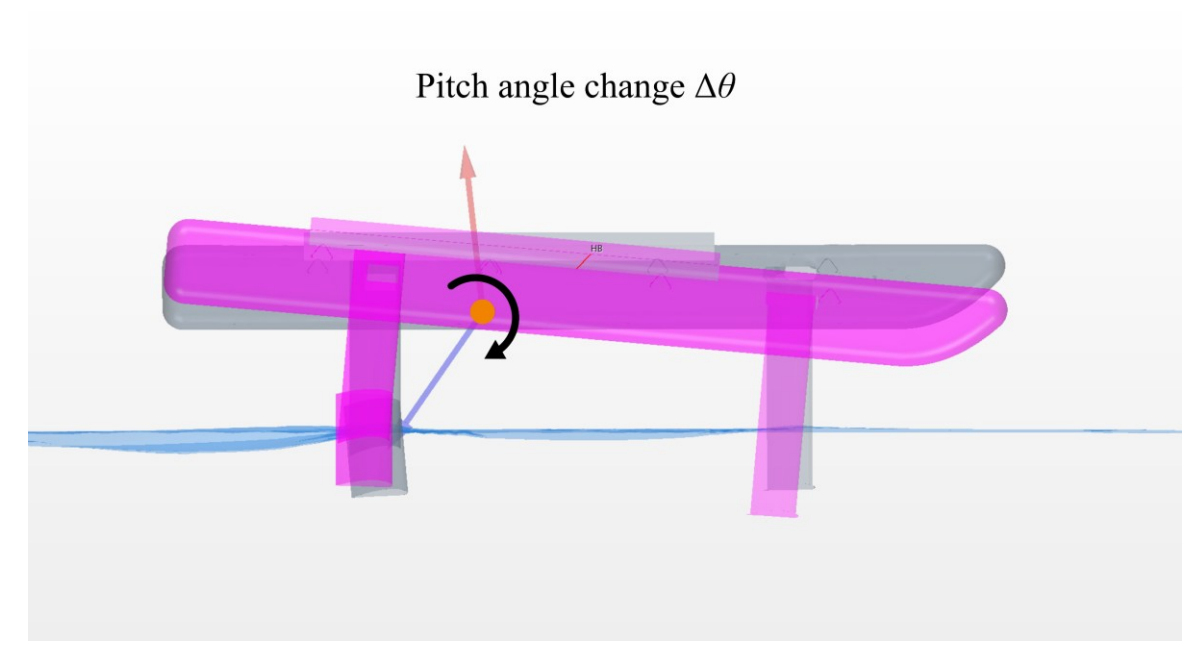


Figure 3.7. A small perturbation applied to the pitch angle in the CFD simulation

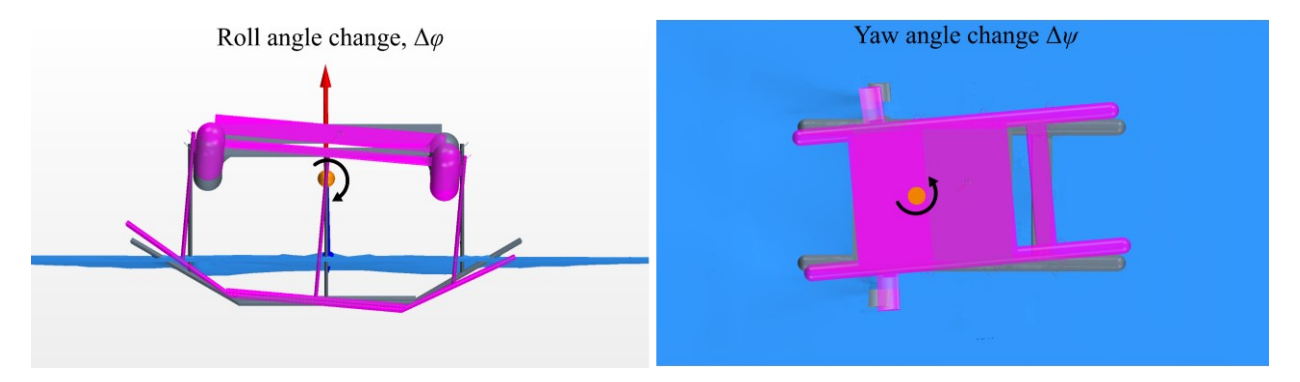


Figure 3.8. A small perturbation applied to the roll (left) and yaw (right) angles, in the CFD simulation

3.5 Variable Control Method for Investigating the Effect of High Dihedral Wings

A variable control method is applied to investigate the effect of high dihedral wings on the roll, pitch, and yaw stabilities of a hydrofoil watercraft. The hybrid layout, featuring a fully submerged canard and a surface-piercing dihedral main wing, is employed in this study. The dihedral angle of the main wing varies from 30° to 50° (Fig. 3.9), with increments of 5°, to analyze the impact on hydrofoil stability. An identical hydrofoil cross-section and equilibrium trim angles are used to isolate the effects of the dihedral angle on stability characteristics. By constraining all other variables and isolating dihedral angle variation, this variable control method enabled an investigation of the relationship between dihedral hydrofoil geometry and stability. Two case studies were performed:

- I. where the AoA of the canard was varied to eliminate its influence from the equilibrium trim position, and
- II. where the canard's AoA was held constant to analyze the effect of the dihedral on the trim position of a hydrofoil watercraft. The second case study is detailed in Appendix C.

Case study I numerically simulates dihedral wings and canard separately to find the optimum canard AoA that maintains an identical overall watercraft trim angle with different dihedral angles. The equilibrium position, forces, and moments define the setting angle of the canard wing to achieve balanced lift distribution and identical trim angles for all tested dihedral models. Dynamic simulations of the main dihedral wing were performed to capture the lift and drag forces, as well as the pitch, yaw, and roll moments around the equilibrium state. The wings are then assembled into the hydrofoil watercraft.

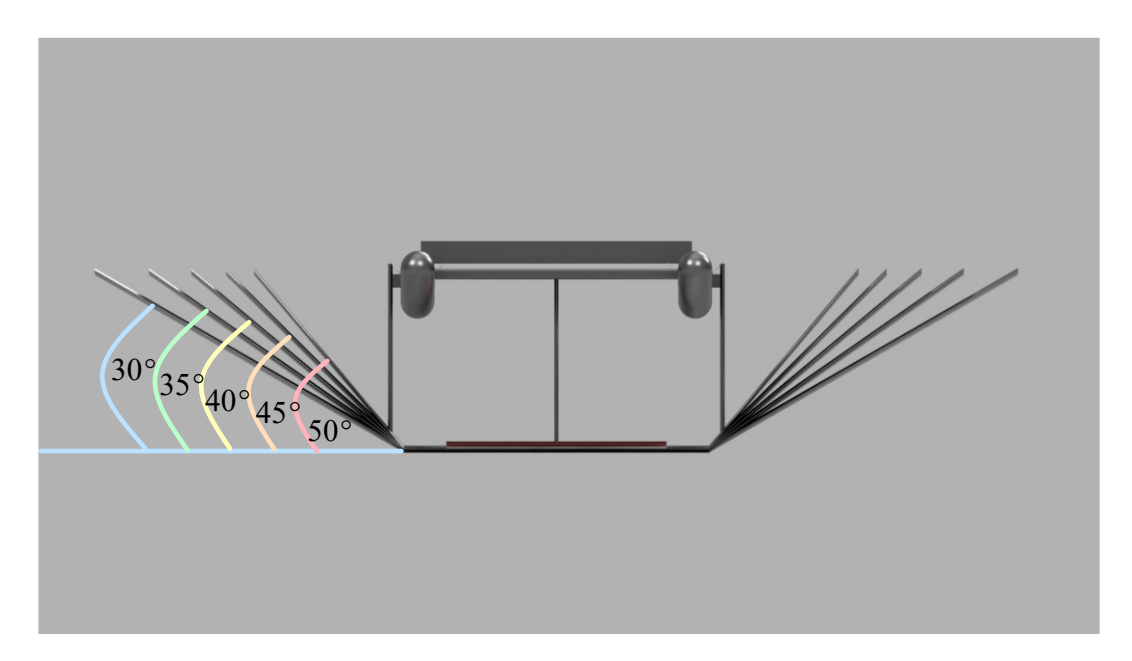


Figure 3.9. Render of canard configured hydrofoil watercraft with varying dihedral angles (wingspan is exaggerated for representation)

The assembly of the hydrofoil watercraft was then simulated to validate the system's equilibrium state under dynamic conditions using the methodology provided in previous sections. The equilibrium state was confirmed when the watercraft maintained steady motion at the desired cruising speed without unbalanced lift and drag forces or moments.

This Chapter outlined the methodology for simulating a hydrofoil watercraft to analyse the stability in the roll, pitch, and yaw axes using CFD. The next Chapter presents the results and discusses how this method can provide insight into the stability of a hydrofoil watercraft in the early design stages.

3.6 Assumptions and Limitations of the Proposed CFD Framework

The framework proposed in this study is limited to the current state of hydrofoil literature and simulation practices. While the simulation results for lift and drag align with experimental data, the validation of the pitch, roll, and yaw moments is incomplete. Available experimental data for surface piercing hydrofoils with high dihedrals are limited in literature. Consequently, direct validation of the simulated moments was not feasible.

In addition, the estimation of the moments is derived from the force predictions. In this study, pitch, roll, and yaw moments were extracted using a small disturbance approach involving changes

in the respective angles. Hence, the deviations in the lift and drag forces may propagate and introduce errors into the derived moment magnitudes. However, the validated lift and drag data provide confidence in the trend accuracy of the resulting moments. The relative magnitudes and directional tendencies of the moments across different dihedral angles provide insights into stability characteristics. For the intended purpose of comparing the relative stability of different hydrofoil configurations in early-stage design, this level of simulation fidelity is considered sufficient[106].

This Chapter outlined the methodology for simulating a hydrofoil watercraft to analyse the stability in the roll, pitch, and yaw axes using CFD. The next Chapter presents the results from this thesis and discusses how this method can provide insight into the stability of a hydrofoil watercraft in the early design stages.

Chapter 4: Results and Discussion

This chapter presents findings from CFD simulations, shows the fidelity of the proposed framework, and investigates the influence of the main wing dihedral angle on the stability characteristics of a canard-configured hydrofoil watercraft. The hydrofoil system includes a fully submerged canard wing and a surface-piercing main wing with dihedral angles ranging from 30° to 50°. The simulations were conducted with identical speed, weight, and CG to isolate the effect of the dihedral angle on the hydrofoil stability.

4.1 Validation of CFD Simulation Framework

The simulation framework was validated using two experimental datasets in literature. The first is from the study experimental and analytical studies of dihedral hydrofoils [58], which provides lift and drag data for hydrofoils with varying AoA and dihedral configurations. The second validation utilized the KCS (KRISO Container Ship) hull benchmark for the drag [107] a standard reference case widely used for marine CFD validation. Although this validation involved a conventional hull, the benchmark validates the boundary conditions chosen to resolve drag forces in an open-water flow. The framework includes the combination of the selected models, meshing strategy, solver settings, and boundary conditions. The validation was performed to assess the framework's fidelity in predicting the lift and drag forces acting on the hydrofoil and the hydrofoil watercraft in general.

Figure 4.1 shows the lift coefficients obtained from the CFD simulations in comparison with experimental data. The trends from the proposed CFD framework simulations closely follow the experimental data, demonstrating good overall agreement. The minor discrepancies are likely as a result of the differences in turbulence modelling and boundary layer transition effects inherent in CFD simulations versus experimental setups. A root mean squared error (RMSE) was calculated to quantify the accuracy of the framework. The results are:

- RMSE_{CL} = 0.004534 and
- $RMSE_{CD} = 0.002862$

The RMSE is over one order of magnitude smaller than the least data point, which validates the simulation methodology proposed in this thesis. The tested data and errors can be found in Table 4.1.

Simulation Validation 0.50 0.40 Simulation Data Coefficient of Lift 0.30 **Experiment Data** 0.20 ···· Poly. (Simulation Data) $R^2 = 0.9266$ 0.10 0.00 0.04 0.05 0.06 0.02 0.07-0.10 -0.20

Figure 4.1. Validation of CFD data using experimental data for dihedral hydrofoils[58]

Coefficient of Drag

Table 4.1. Quantitative validation of CFD results against experimental data

Simulation <i>C_L</i>	Simulation <i>C_D</i>	Experiment C_L	Experiment C_D	Error C _L	Error C_D	Squared Error C _L	Squared Error <i>C_D</i>
-7.89E-02	3.10E-02	-7.47E-02	3.08E-02	-4.24E-03	1.17E-04	1.80E-05	1.37E-08
4.04E-03	3.05E-02	1.92E-03	3.00E-02	2.12E-03	5.29E-04	4.51E-06	2.80E-07
7.85E-02	3.23E-02	7.22E-02	3.48E-02	6.26E-03	-2.54E-03	3.92E-05	6.44E-06
1.59E-01	3.58E-02	1.55E-01	3.19E-02	3.82E-03	3.83E-03	1.46E-05	1.47E-05
2.24E-01	4.14E-02	2.18E-01	3.73E-02	6.48E-03	4.19E-03	4.19E-05	1.76E-05
2.92E-01	4.91E-02	2.92E-01	4.56E-02	1.44E-04	3.48E-03	2.07E-08	1.21E-05
3.59E-01	5.85E-02	3.64E-01	6.10E-02	-5.06E-03	-2.49E-03	2.56E-05	6.20E-06

Furthermore, the validation against the KCS hull demonstrated a deviation of only 1.56% between the simulated and experimental drag coefficients, as shown in Table 4.2, further confirming the fidelity of the CFD framework.

Table 4.2. KCS hull validation comparison

Simulation Drag Coefficient	Experimental Drag Coefficient	Deviation
0.003769	0.003711	1.56%

The validation results demonstrate that the proposed CFD simulation framework accurately captures the lifts and drags of hydrofoils. These forces directly generate the moments from which the stability derivatives are derived. While moment validation would further support the confidence of the simulation, the current force validation is considered sufficient for the purpose of this study, i.e. estimating stability at the early design stages. This validation establishes a foundation for the application of the simulation methodology in analyzing the hydrodynamic performance of hydrofoil watercraft, with reliable predictive capability.

4.2 Application of the Simulation Framework to Hydrofoil Configurations

With the validated framework, the hydrodynamic performance of three hydrofoil layouts selected for an electric hydrofoil watercraft was evaluated, as detailed in Appendix B. Tables 4.3 and 4.4 summarize the power trade-off study conducted using the proposed simulation framework for the three configurations, while Table 4.5 compares the configurations.

4.2.1 Overview of Evaluated Configurations

Figure 4.2 shows the three hydrofoil layouts analyzed in this study, which are:

- I. Configuration a: Hybrid layout
- II. Configuration b: Surface-piercing dihedral tandem layout
- III. Configuration c: Surface-piercing dihedral canard layout

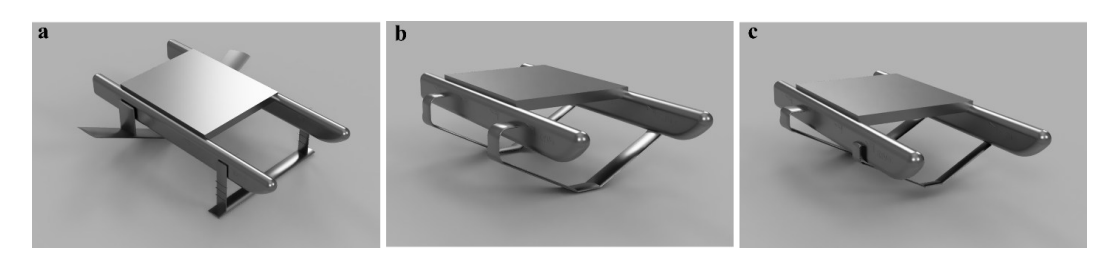


Figure 4.2. Hydrofoil configurations: a) Hybrid layout, b) Surface-piercing dihedral tandem layout, and c) Surface-piercing dihedral canard layout

Tables 4.3 and 4.4 present the results of drag, theoretical power consumption, and range using the requirements shown in Table 3.1 with a focus on low-speed performance at 7 km/h and mid-speed cruising performance between 10.8 and 11.52 km/h. Refer to Appendix B for the full set of simulated results under different speeds.

Table 4.3. Configuration performance comparison

Mission	Velocity		e-piercing Tar Configuration	ndem	Surface-piercing Canard Configuration		
Stage	(km/h)	Drag (N)	Required Power (W)	Range (h)	Drag (N)	Required Power (W)	Range (h)
Cruising	7.00	622.52	1207.69	-	331.50	643.10	-
Cruising	10.80	107.71	323.13	1.56	106.38	319.14	1.58
Cruising	11.52	111.83	357.86	1.41	108.13	346.02	1.46
Cruising	14.98	122.26	508.60	0.99	113.90	473.82	1.06

Table 4.4. Performance estimation of selected configurations

Mission	Velocity	Surface-piercing Canard Configuration		1 0			Ну	brid Configura	tion
Stage	(km/h)	Drag (N)	Required Power (W)	Range (h)	Drag (N)	Required Power (W)	Range (h)		
Cruising	7.00	331.50	643.10	0.78	151.30	293.52	1.72		
Cruising	10.80	107.71	323.13	1.56	210.00	630.00	0.86		
Cruising	11.52	111.83	357.86	1.41	181.92	582.14	0.94		

4.2.2 Low-Speed Performance: Takeoff and Cruising at 7 km/h

At a velocity of 7 km/h, the hybrid configuration produces the lowest drag force (151.30 N) and requires only 293.52 W of power. This performance can be attributed to the foil arrangement. The

fully submerged canard reduces the drag from surface waves by avoiding surface interaction. At the same time, the surface-piercing dihedral main foil limits wetted area and self-regulates ride height, reducing unnecessary lift and associated drag. This combination results in a flow with minimal disturbance, making the hybrid layout effective for low-speed cruising.

In contrast, the tandem and canard configurations experience significantly higher drag (622.52 N and 331.50 N, respectively) and thus demand higher power. The improved performance of the hybrid configuration at low speeds is attributed to its minimized wetted surface area and foil arrangement. This low-speed efficiency of the hybrid configuration results in the longest operational range (1.72 hours), which is over 50% longer than that of Configuration b (0.78 hours) and Configuration c (0.38 hours), aligning with the design requirements for low-speed energy efficiency.

4.2.3 Mid-Speed Performance: Cruise (10.80 - 11.52 km/h)

At higher speeds, however, the Surface-piercing Canard Configuration (Configuration b) outperformed the hybrid and tandem in terms of drag and power requirements, with a longer range of up to 1.56 hours at 10.80 km/h. This improvement is associated with the stability and efficiency of surface-piercing foils at higher speeds, resulting from the inherent self-regulating lift behaviour of dihedral geometries.

In contrast, the hybrid configuration experienced increased drag and reduced range (0.86 - 0.94 hours) at speeds of 10.80 km/h to 11.52 km/h. As the speed increased, the riding height increased, and the canard foil approached the free surface, which in turn increased the free surface effects such as ventilation and wave interference, as described in Section 2.2. This performance reduction highlights a trade-off between low-speed and high-speed efficiency inherent in hybrid foil designs.

4.2.4 Human versus Electric Propulsion Analysis

A study was performed to ensure that the user could maintain foiling at low-speed cruising using only human power. The power required at 7.2 km/h (approximately 250 W) lies within the sustainable output of a trained amateur rider (typically 200 - 300 W)[108], making it feasible for short periods of self-powered operation. At this speed, the hybrid design enables a cruising duration of over 1 hour with a total input power of 500 W, demonstrating the watercraft's suitability for both pedal-assist and pure human-powered use in low-drag conditions.

The electric-only results (Table B.4 in Appendix B) show a similar trend, with cruising ranges of up to 17.5 km at 9.72 km/h, indicating a strong alignment with range and efficiency objectives under battery propulsion. Further information is provided in Appendix B.

Table 4.5. Summary of configuration performance

Configuration	Strengths	Limitations	Use case
Hybrid	Low-speed	Drag increases at mid-range	Low-speed cruising,
	performance	speeds due to free surface	pedal-assist
		interference	
Surface-Piercing	Moderate cruising	Higher drag at low speeds	Mid-speed efficient
Canard	speeds, consistent		cruising
	range across 10 - 15		
	km/h		
Surface-Piercing	Stable lift distribution	Highest drag at all speeds	
Tandem			-

The following section presents the results of a dynamic stability margin study, demonstrating the capability of the proposed framework.

4.3 Stability Margin Evaluation

Following the performance comparison, the hybrid configuration, Configuration a, comprising a fully submerged canard and a surface-piercing dihedral main foil, was simulated to determine the extent to which the hydrofoil watercraft can withstand disturbance while returning to its original position without any input from the rider, known as the fixed-stick condition. This is achieved by introducing external hydrodynamic forces and moments as disturbances in the simulation.

4.3.1 Passive Stability Margin Analysis

To investigate the inherent stability of the hybrid layout, simulations were conducted in which external disturbances were applied in pitch, yaw, and roll. Figure 4.3 shows the response of the watercraft to each disturbance, visualized as the angle changes in pitch, yaw, and roll at three stages: initial equilibrium state, change in attitude due to disturbance, and return to the stable equilibrium state.

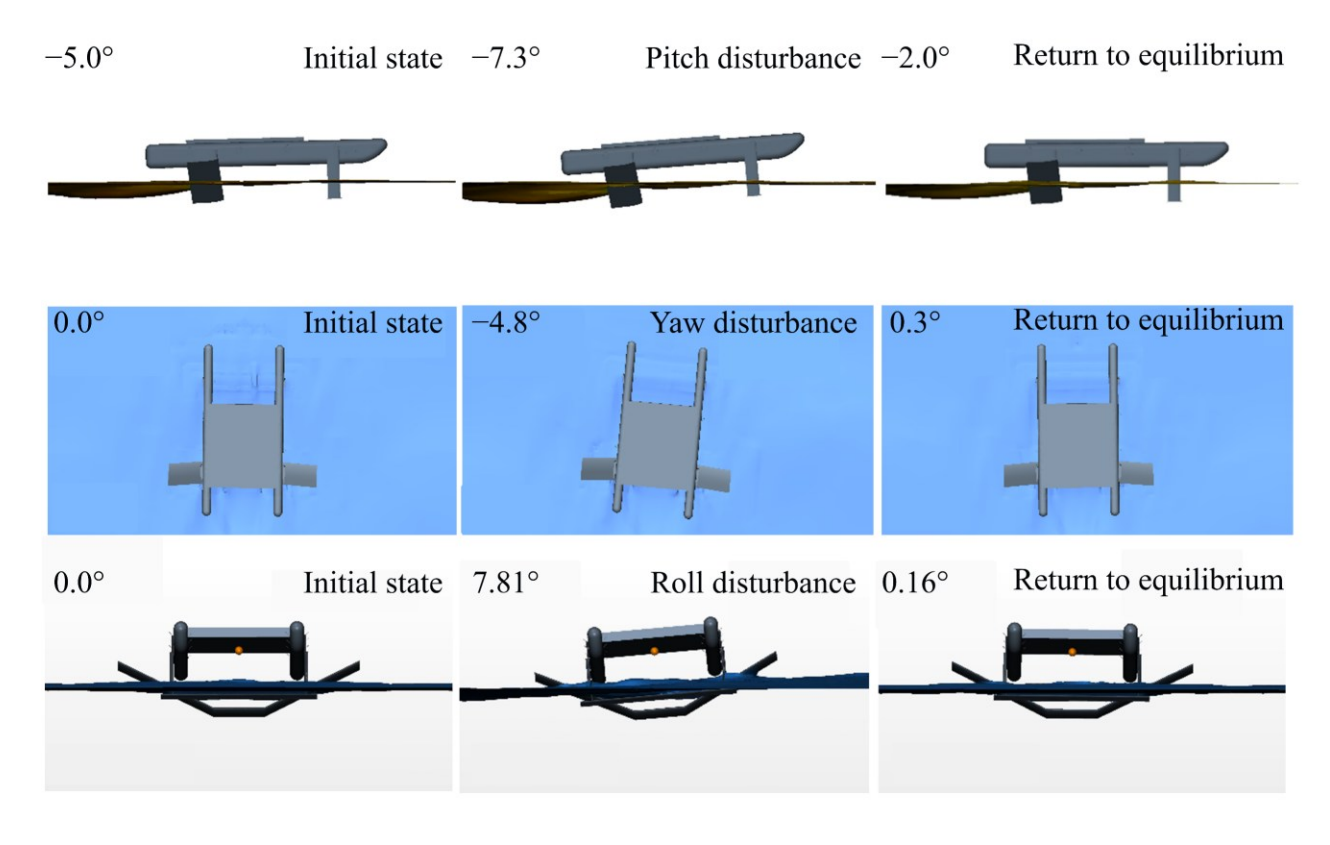


Figure 4.3. Passive stabilizing effect. From top to bottom, trim, yaw, and roll stability. From left to right, initial state, after introduction of disturbance, and return to stable state.

The results demonstrate that the hybrid configuration exhibits passive restoring behaviour in all three axes. The subsequent sections explain the self-righting ability of the hydrofoil watercraft as a result of the dihedral wing.

4.3.2 Mission Profile Simulation

Figure 4.4 presents the whole mission profile simulation of the hybrid configuration, from displacement mode to takeoff, cruising, and response to transient perturbations. The simulation results further demonstrate the framework's capacity in modeling a complete operational scenario.

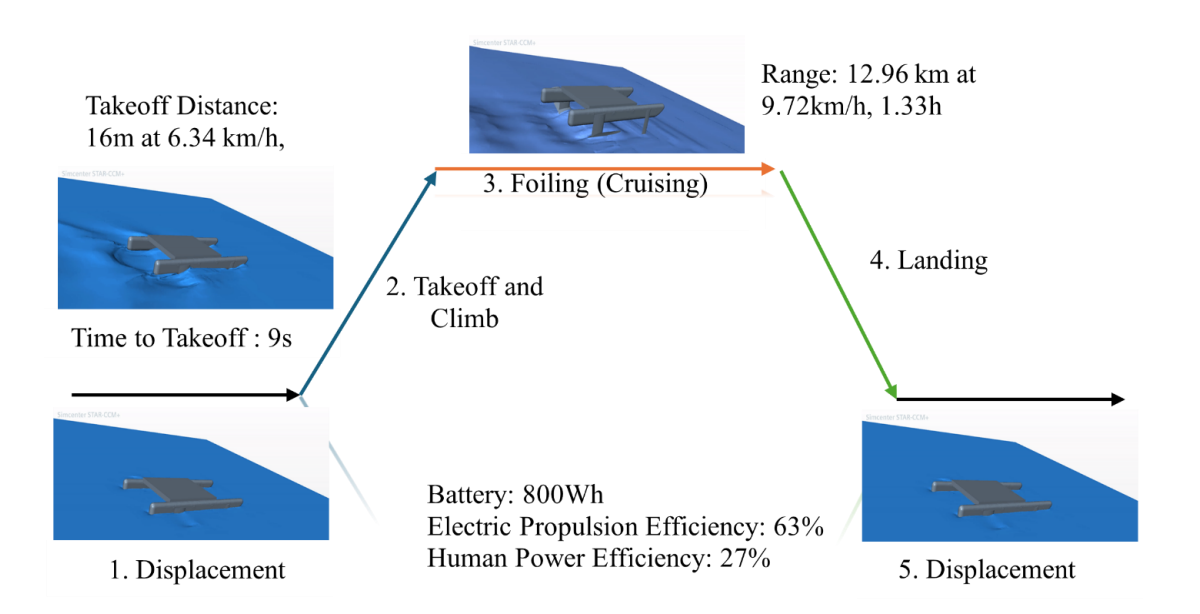


Figure 4.4. A sample mission profile of the hybrid configuration

Having validated the performance and passive stability of the hybrid layout, the following section presents results for investigating the effect of high dihedral angles on the roll, pitch, and yaw stability of a hydrofoil watercraft.

4.4 Equilibrium Position

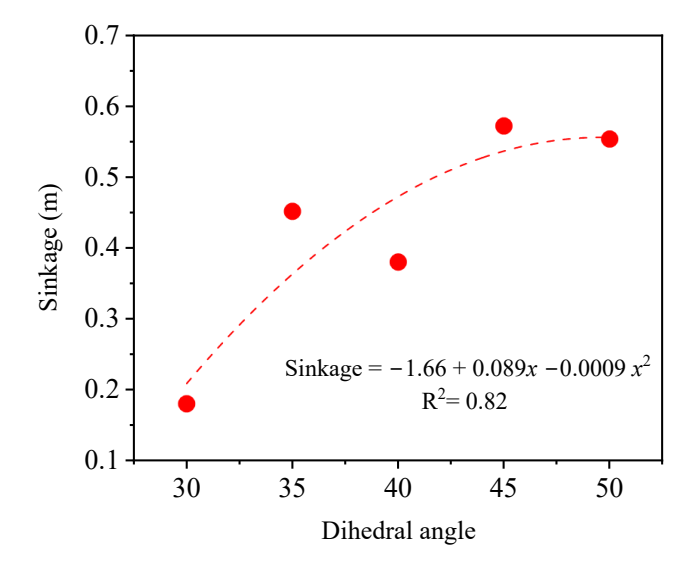


Figure 4.5. Sinkage changes with respect to dihedral angle variation

Figures 4.5 to 4.7 show that, under an identical speed of 3 m/s, the riding height decreases as the dihedral angle increases. Increasing the dihedral angle increases the wing's inclination away from

the horizontal plane, which reduces the horizontal reference area and, in effect, reduces the effective lift component. This relationship can be expressed mathematically as $L_{vertical} = L \cos \Gamma$. To compensate for the lift reduction, the hydrofoil watercraft's foils increase submergence, which generates sufficient lift for steady cruising. The complete simulation results of the dihedral angles and corresponding canard angles are presented in Appendix C.

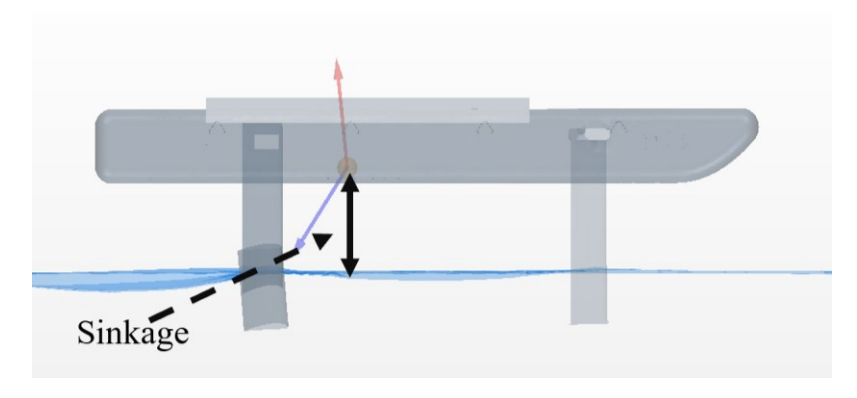


Figure 4.6. Sinkage at the equilibrium position

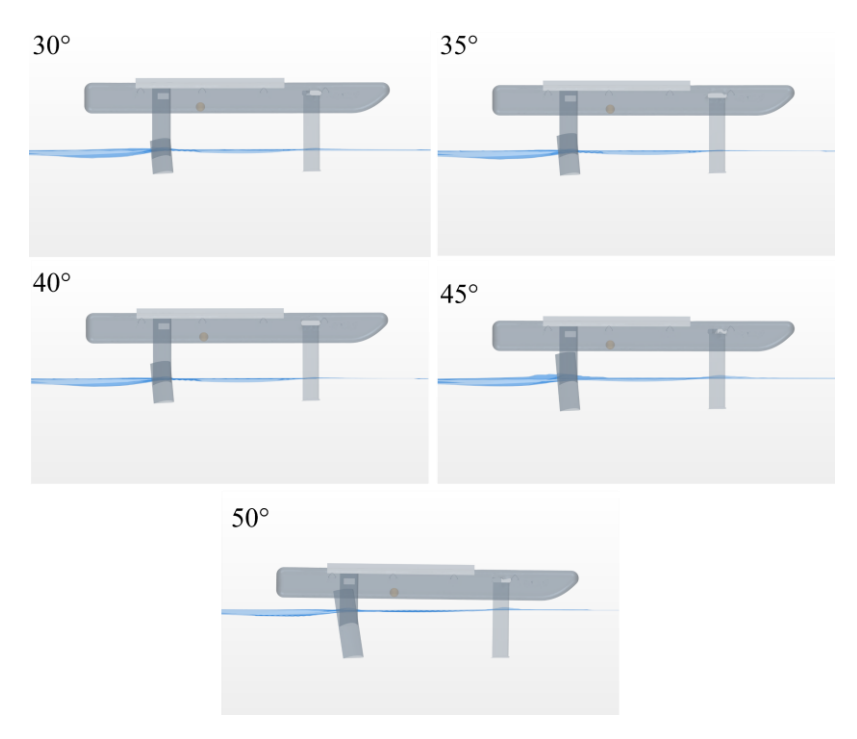


Figure 4.7. Trim position at equilibrium stages of hydrofoil with different dihedral angles

4.5 Stability Derivatives

This section presents the results and discusses the variation of non-dimensional stability derivatives C_l , C_m , and C_n , with respect to the dihedral angle. The stability derivatives are derived under three

types of angular disturbances, pitch (θ) , roll (ϕ) , and yaw (ψ) . These derivatives quantify the influence of the dihedral angle on the longitudinal, lateral, and directional stability of the hydrofoil watercraft, as well as the interaction between different stability axes. The methodology for extracting the derivatives has been outlined in the previous chapter.

4.5.1 Stability Derivatives with Respect to Pitch $(\partial \theta)$

The stability behavior of a hydrofoil watercraft in response to pitch disturbances is primarily characterized by the pitch moment derivative with respect to the pitch angle, $C_{m_{\theta}}$, and secondarily by cross-coupling derivatives such as the roll moment derivative with respect to pitch, $C_{l_{\theta}}$, and the yaw moment derivative with respect to pitch, $C_{n_{\theta}}$. The calculated nondimensional stability derivatives under a pitch disturbance are summarised in Table 4.6. Figure 4.8 shows the 35° and 45° dihedral hydrofoil watercraft after a pitch disturbance in the form of a pitch angle change of 2° is introduced.

A stable system typically exhibits:

- I. $C_{m_{\theta}} < 0$: A pitch-up moment in response to a pitch-down disturbance (restoring pitch stability) and vice versa
- II. $C_{l_{\theta}} < \theta$: Roll stability induced by pitch (e.g., dihedral effect in aircraft)
- III. $C_{n_{\theta}} < \theta$: Directional stability following a pitch disturbance.

Table 4.6. Nondimensionalized stability derivatives with respect to pitch

Dihedral Angle (°)	$C_{l_{ heta}}$	$C_{m_{\theta}}$	$C_{n_{\theta}}$
30	-0.0078	-0.6947	-0.0128
35	0.0098	-0.6495	0.0195
40	0.0095	-0.6289	0.0179
45	-0.0122	-0.7404	-0.0234
50	0.0157	-0.7664	0.025

Table 4.7. Moments generated by the dihedral wings on opposite sides in response to a pitch disturbance

	3:	5°	4:	5°
Dihedral Angle	Left dihedral	Right dihedral	Left dihedral	Right dihedral
Pitch (Nm)	128.5441	127.5139	75.12691	76.73265
Roll (Nm)	-89.5639	88.89567	-38.0517	38.85407
Yaw (Nm)	-100.676	100.182	-79.8428	81.51293

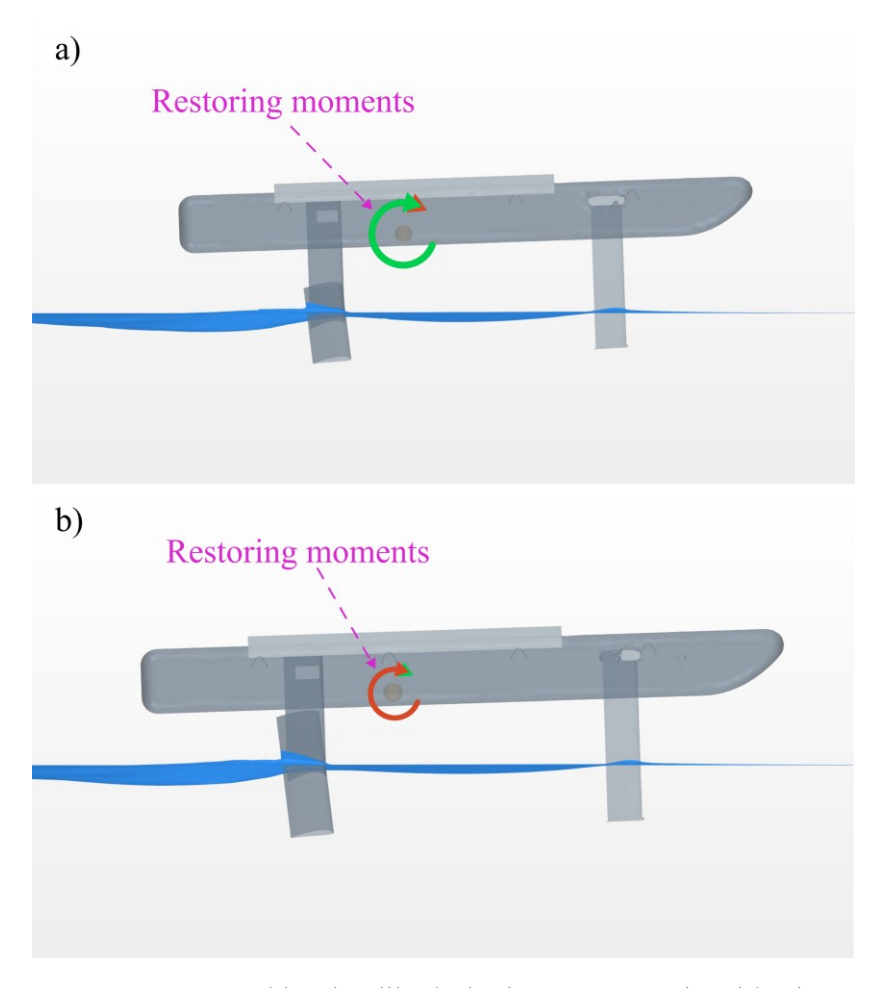


Figure 4.8. Moments generated by the dihedral wings on opposite sides in response to a pitch disturbance (Moment not drawn to scale). The red moment represents the left wing, and the green moment represents the right wing. a) 35° dihedral model and b) 45° dihedral model

Pitch Response

The hydrofoil exhibits pitch stability for the tested dihedral angles when a pitch disturbance is introduced, as seen in Table 4.6 and Fig. 4.8. However, the absolute values of pitch stability decrease from $C_{m_{\theta}}$ of -0.6947 at 30° dihedral angle to -0.6289 at 40° dihedral angle. Beyond the 40° dihedral, the pitch stability improves with $C_{m_{\theta}}$ increasing to -0.7664 at 50°. The increase in pitch stability does not align with the restoring moments generated by the dihedral wings as shown in Table 4.7. The 35° dihedral with a -2° disturbance generates a restoring pitching moment of 256.1 Nm, which is higher than a 151.9 Nm pitching moment generated by the 45° dihedral under an identical disturbance. The discrepancy in the nondimensionalized data to the raw moments generated by the dihedral wings is as a result of the overall moment from the watercraft and from the reference area used in the nondimensionalization.

The decrease in pitch stability with increasing dihedral angle can be attributed to the reduced lift component in the vertical direction as the dihedral angle increases. The reduction in the vertical lift component moves the aerodynamic center of the hydrofoil closer to the CG, which leads to a shorter moment arm and a reduction in the restoring moments as the dihedral angle increases.

Roll and Yaw Response

As shown in Table 4.6, the roll moment stability derivatives with respect to pitch perturbations, denoted by $C_{l_{\theta}}$, change from -0.0078 at 30° dihedral angle to .0098 and 0.0095 at 35° and 40° dihedral angle, respectively, indicating a reduction in pitch induced roll stability. However, at 45°, $C_{l_{\theta}}$ becomes negative, indicating a pitch induced roll restoring tendency. At 50°, $C_{l_{\theta}}$ becomes 0.0157, indicating pitch-roll coupling. Similarly, the yaw stability derivative in response to a pitch disturbance exhibits a nonlinear trend.

The nonlinear response of roll and yaw to a pitch disturbance may be owing to ventilation and interaction with the free surface due to localised waves. The presence of small wave disturbances and surface deformation due to the piercing of the water creates local variations in submersion depth on the sides of the dihedral wing. These surface irregularities can cause an uneven and asymmetrical submergence in the span direction on both sides of the dihedral wing. The difference in submergence area generates asymmetric lift, creating a destabilizing roll and yaw moment. The destabilising roll/yaw moment increases as the dihedral angle increases, leading to a stronger pitch-roll or pitch-

yaw coupling. Furthermore, this coupling can cause oscillatory behavior in the hydrofoil watercraft. The change in signs of the stability derivatives is a result of this nonlinear coupling between the stability axes, which makes the results inconsistent. Increasing the convergence threshold for the forces may provide more consistent results for smaller forces and moments.

The results indicate that the roll and yaw moments do not experience significant changes in response to a pitch disturbance, as shown in Table 4.7. For example, the 35° dihedral wing produces a -0.7 Nm roll moment as compared to 256.1 Nm pitch moment in response to the 2° pitch displacement. The roll and yaw moments from the opposing dihedral wings tend to be even, and the moment asymmetry increases with increasing dihedral.

In summary, increasing the dihedral progressively reduces the restoring moments under a pitch disturbance. Hence, the hydrofoil watercraft's ability to self-correct is reduced at higher dihedral angles.

4.5.2 Stability Derivatives with Respect to Roll $(\partial \phi)$

The stability behavior of a hydrofoil watercraft in response to roll disturbances is presented in this section. The stability derivatives considered are $C_{m_{\phi}}$, $C_{l_{\phi}}$, and $C_{n_{\phi}}$. The calculated stability derivatives under a roll disturbance are summarised in Table 4.8.

Table 4.8. Nondimensionalized stability derivatives with respect to roll

Dihedral Angle (°)	$C_{l_{\phi}}$	$C_{m_{\phi}}$	$C_{n_{\phi}}$
30	-0.0386	-0.5574	-0.0241
35	-0.0156	-0.5066	-0.0165
40	-0.0169	-0.4968	-0.0199
45	-0.0016	-0.5385	-0.0163
50	0.0099	-0.6049	0.0128

Table 4.8 examines the hydrofoil watercraft's stability derivatives in response to a roll disturbance. The results in Table 4.10 show a change in roll restoring moment from -25.6 Nm at 30°

dihedral angle to 6.54 Nm at 50° dihedral, which results in a decrease in the roll stability derivative as seen in Table 4.8. The list of non-dimensionalized stability derivatives is presented in Appendix D.

Table 4.9. Moments generated by the dihedral wings on opposite sides in response to a roll disturbance

	3:	5°	4.5	5°
Dihedral Angle	Left dihedral	Right dihedral	Left dihedral	Right dihedral
Pitch (Nm)	-54.3581	86.00996	80.94191	121.6709
Roll (Nm)	80.04304	131.4442	-43.7577	62.32192
Yaw (Nm)	-68.4999	93.43544	-94.8442	117.5895

Table 4.10 Stability derivatives in response to a roll disturbance

Dihedral Angle (°)	Roll Moment Derivative (Nm)	Pitch Moment Derivative (Nm)	Yaw Moment Derivative (Nm)
30	-25.59927	-369.3745	-15.99038
50	6.54253	-400.8385	8.46203

Theoretically, increasing the dihedral angle is expected to enhance the roll stability, as a larger dihedral amplifies the lateral restoring moment generated by the greater asymmetric lift during roll (shown in Fig. 4.9). When a roll disturbance is introduced, the side of the wing to which the hydrofoil watercraft rolls becomes more submerged and hence generates more lift. The difference in submergence area between the two sides of the wing increases as the dihedral angle increases, resulting in more uneven lift on the two sides of the wing and creating a stronger restoring roll moment. However, as the asymmetric lift increases, pitching moments are also created. The vertical component of the roll-restoring force causes these pitching moments. The extra pitching moments reduce pitch stability, which in turn affects coupled roll stability. This coupling between the lateral and longitudinal stabilities increases with the gain of dihedral angle, leading to an overall decrease in roll stability. The results in Table 4.9 confirm this phenomenon as the total restorative moment from the opposing dihedral wings decreases from 211.5 Nm at the 35° dihedral to 18.6 Nm at the 45° dihedral. The moments of each dihedral wing are shown in Fig. 4.10. A similar phenomenon occurs with the

yaw stability derivative. The results show that at a dihedral angle of 50°, the hydrofoil loses yaw and roll stability, as evidenced by the positive stability derivatives. This trend indicates reduced restorative moments and thus diminishing stability at higher dihedral angles.

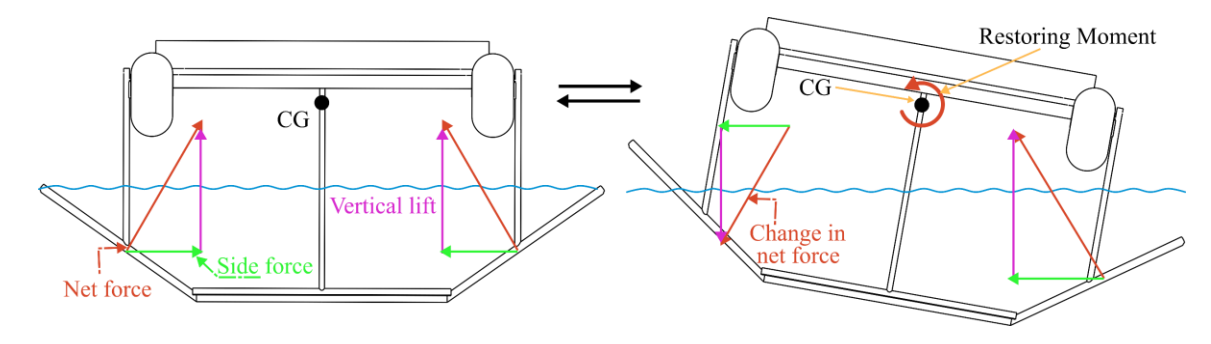


Figure 4.9. Demonstration of the change in lift and moment arm due to changes in the submerged area of the dihedral wing

Furthermore, there is a decrease in the coupled roll-yaw resistance at low dihedral as the dihedral angle increases. While roll-yaw coupling is expected in surface-piercing dihedral wings, as evidenced by the magnitude of the roll induced yaw stability derivatives, the reduction in $C_{l_{\phi}}$ from -0.0386 at 30° dihedral angle to 0.0099 at 50° dihedral angle and $C_{n_{\phi}}$ from -0.0241 at 30° dihedral angle to 0.0128 at 50° dihedral angle suggests increased susceptibility to oscillatory motions like "Dutch roll"[58]. Further dynamic analysis would be required to confirm this phenomenon.

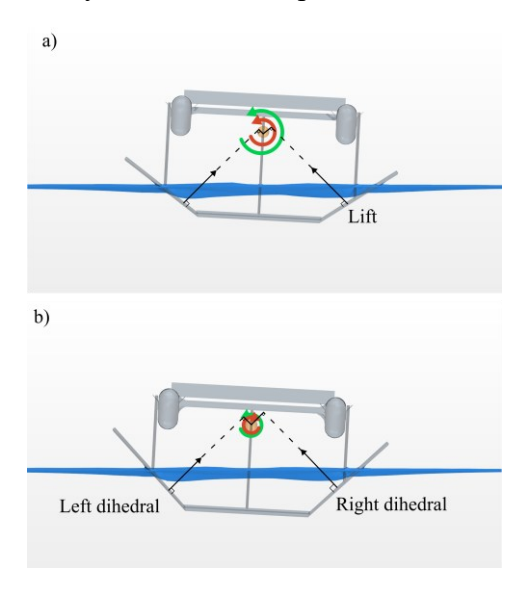


Figure 4.10. Moments generated by the opposing dihedrals in response to a roll disturbance (Force, moment and moment arm not drawn to scale). The red represents the left wing, and the green represents the right. a) 35° and b) 45° dihedral model

In summary, increasing the dihedral angle reduces the capability of the hydrofoil watercraft to return to equilibrium after a roll disturbance. Dihedral angles greater than 45° show a positive roll moment derivative coefficient, indicating a destabilizing moment.

4.5.3 Stability Derivatives with Respect to Yaw $(\partial \psi)$

The data presented in Table 4.11 are the results of the nondimensionalized stability derivatives under a yaw disturbance in the form of a 3° yaw angle change. The results indicate that an increase in dihedral angle reduces the hydrofoil's ability to generate corrective roll and yaw moments. Since roll and yaw are closely coupled in hydrofoil dynamics, especially with surface-piercing elements, these results suggest that increasing dihedral makes the hydrofoil system more susceptible to oscillatory behaviour.

Table 4.11. Nondimensionalized stability derivatives with respect to yaw

Dihedral Angle (°)	$C_{l_{\psi}}$	$C_{m_{\psi}}$	$C_{n_{\psi}}$
30	-0.0238	-0.5505	-0.0108
35	-0.0182	-0.5031	-0.0064
40	-0.016	-0.4883	-0.004
45	-0.0119	-0.5153	-0.0015
50	-0.0194	-0.5906	-0.0381

Table 4.12. Moments generated by the dihedral wings on opposite sides in response to a yaw disturbance

	35°		45°	
Dihedral Angle	Left dihedral	Right dihedral	Left dihedral	Right dihedral
Pitch (Nm)	109.3288	97.81534	92.94927	108.3994
Roll (Nm)	-77.8205	61.22109	-45.5157	61.33824
Yaw (Nm)	-86.0001	74.94359	-97.5889	116.4829

Figure 4.11 shows the tendency of the hydrofoil watercraft to produce a righting moment to return to the equilibrium position after a yaw disturbance in the form of a 3° yaw angle change is introduced. The trend of yaw stability derivatives is similar to that of the roll disturbance derivatives, which aligns with aircraft theory due to their coupled interaction. The data in Table 4.13 show a consistent decrease in the absolute value of yaw righting moments from -7.14 Nm at a 30° dihedral angle to -1.01 Nm at a 45° dihedral angle, and an increase of over 300% at the 50° dihedral angle to -25.27 Nm. This may be caused by increased coupling between the stability axes as the roll and pitch moment absolute values also increase from -7.91 Nm and -341.45 Nm at 45° to -12.86 Nm and -391.40 Nm at 50° dihedral angle, respectively.

Table 4.13. Stability derivatives in response to a yaw disturbance

Dihedral Angle (°)	Roll Moment Derivative (Nm)	Pitch Moment Derivative (Nm)	Yaw Moment Derivative (Nm)
30	-15.78209946	-364.8208563	-7.144283654
35	-12.03287156	-333.4050315	-4.270734593
40	-10.62659655	-323.573888	-2.662971884
45	-7.906842417	-341.4478497	-1.017046387
50	-12.85821652	-391.4007133	-25.27194501

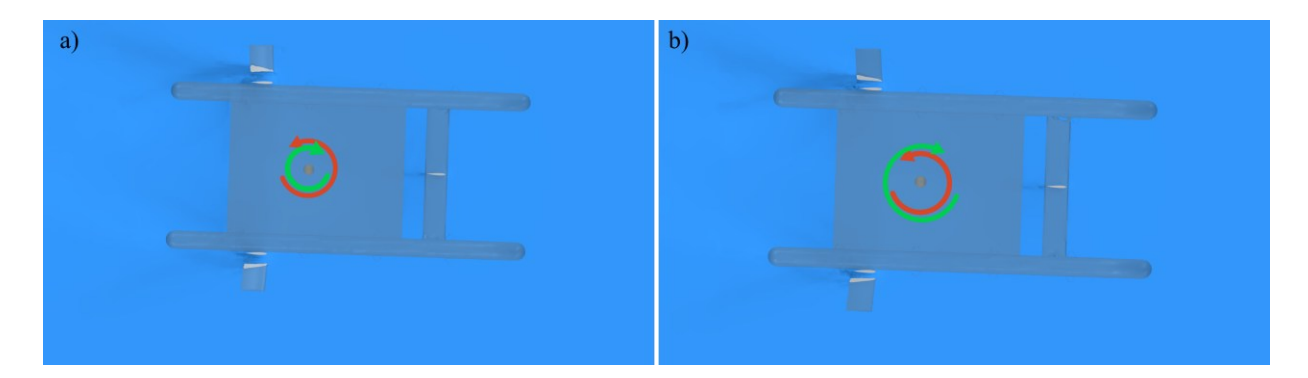


Figure 4.11. Moments generated by the dihedral wings on opposite sides in response to a yaw disturbance (Moments not drawn to scale). The red moment represents the left wing, and the green moment represents the right wing. a) 35° dihedral model and b) 45° dihedral model

The trend of stability decrease is a result of the change in flow direction, asymmetric lift, and coupling between the stability axes, discussed as follows:

Flow direction: A yaw disturbance causes the dihedral wing to have a lateral motion vector component of the water flow. This lateral component creates a side force (Fig. 4.9) on each side of the hydrofoil due to the angle of the wing surface with respect to the incoming flow. A portion of the produced side force is converted into vertical lift due to the dihedral geometry, instead of contributing to directional stability. The lateral component of this force, which contributes to the yaw stability, can be expressed as $F_{side_{lateral}} = F_{side} \sin \Gamma$, which increases as the dihedral angle increases. The increase in side force is coupled with the increase in uneven and asymmetrical submergence in the span direction on both sides of the dihedral wing, leading to an increase in asymmetric lift. However, when the lateral force component is even larger, it can induce rolling. This coupling further reduces the yaw and roll stabilities as the dihedral angle increases, as shown in Table 4.11. The sum of the yaw moments from the two sides of the dihedral wing decreases as the dihedral angle increases, as seen in Fig. 4.9 and Table 4.12, leading to less yaw stability.

Yaw-roll Coupling Interference: A yaw motion of surface-piercing foils often causes secondary roll due to asymmetric lift. This roll further introduces unevenness in wetted areas across the dihedral wing, producing asymmetric lift that affects yaw recovery in a nonlinear manner. The coupling between roll and yaw becomes more intense with increased dihedral, as can be seen for the 50° dihedral results. This may be because a yaw-induced roll feeds back into the yaw response, which also feeds into the pitch response as detailed in Section 4.2.2.

In summary, increasing the dihedral angle generally reduces the hydrofoil's stability. Beyond the 45° dihedral angle, nonlinear coupling between the stabilities in different axes increases, potentially resulting in amplified responses to disturbances.

.

Chapter 5: Summary and Conclusion

This project quantified the stability of high dihedral angles (30° - 50°) on the pitch, roll, and yaw stability of a hydrofoil watercraft. The proposed CFD simulation framework determined the lift and drag forces, as well as the pitch, roll, and yaw moments of the hydrofoil watercraft. The free surface effect caused by the air-water boundary of the surface-piercing hydrofoils with high dihedral angles was considered in the numerical simulation. The free surface effect reduces the lift-to-drag ratio as the hydrofoil approaches the water surface. It also introduces phenomena such as ventilation, which disrupts the water flow along the span of the hydrofoil. The simulation framework is capable of estimating the complex nonlinear behavior of the flow and the coupled nature of the forces. The forces and moments for each dihedral case were calculated from the simulations and then transformed into stability derivatives using the small disturbance theory. This work examined the contribution of high dihedral angles to the stabilities of hydrofoil roll, pitch, and yaw.

5.1 Contribution and Summary of Findings

This thesis makes three contributions.

- I. Developed a CFD-based simulation framework for hydrofoil stability
- II. Performed performance tradeoff studies of different hydrofoil configurations
- III. Analysed the influence of high dihedral angles on the pitch, roll, and yaw stability of a hydrofoil watercraft

The proposed simulation framework is capable of accurately modelling the hydrofoil lift and drag forces acting on hydrofoils, including the effects of the air-water interface. When validated against experimental data, the framework demonstrated lift prediction accuracy within a 4% relative error and drag prediction accuracy within 8%. The framework is also capable of simulating the performance of hydrofoil's entire mission profile, as well as the dynamic stability margins of a hydrofoil watercraft within a single dynamic simulation setup.

The developed framework was applied to evaluate the range of three electrical hydrofoil configurations considered in this thesis. The findings showed that the hybrid configuration exhibited improved efficiency at low speeds, with a range of 1.72 hours. In contrast, the canard surface-piercing configuration delivered better performance at higher speeds, with a range nearly twice that of both

the hybrid and tandem surface-piercing configurations. The findings from this study highlight the framework's ability to differentiate between the performance of hydrofoil configurations, making it a valuable tool in concept evaluation and selection, especially during the conceptual design stages of hydrofoil watercraft.

This work explores the influence of the dihedral angle on the hydrofoil's stability across roll, pitch, and yaw axes. In terms of roll stability, dihedral angles between 30° - 40° offer the best balance between roll resistance and stable behavior. However, as the dihedral angle increases beyond 45°, the hydrofoil's roll resistance begins to reduce, leading to increased susceptibility to roll oscillations, particularly under yaw disturbances. Dihedral angles between 45° - 50° increase the possibility of oscillatory behavior due to the reduced stability in yaw and pitch.

The CFD simulation results show that the restoring moments for pitch stability decrease as the dihedral angle increases. This is in part because of the increased asymmetric lift distribution, which reduces the hydrofoil's ability to recover from pitch disturbances. As the dihedral angle increases, the hydrofoil becomes more sensitive to pitch disturbances, requiring additional stabilization measures.

For yaw stability, the hydrofoil becomes less yaw resistant as the dihedral angle increases. This can be attributed to factors such as the yaw moment arm decreasing as the dihedral angle increases, reducing yaw stability. At 50° dihedral angle, the yaw-roll coupling increases, further complicating the hydrofoil's stability.

In summary, dihedral angles between 30° and 40° show optimum stability across the longitudinal, lateral, and directional stability axes. Higher dihedral angles, e.g. those above 40°, can lead to increased coupling effects, which may destabilize the hydrofoil watercraft when disturbed. This study shows the need to carefully consider the dihedral angle when optimizing hydrofoil performance, since the hydrofoil with dihedral angles above 40° needs control mechanisms to maintain system stability.

5.2 Future Work

The stability derivatives in this thesis show the effect of the dihedral angle on the pitch, yaw, and roll stability of the hydrofoil watercraft. These derivatives serve as the foundation for building a stability framework to analyze various hydrofoil configurations, especially in the early design stages.

Future work may include developing a framework to provide more intuitive results on the stability of hydrofoil watercraft. It should also consider the dynamic responses brought about by the dihedral wing. Additionally, there are several improvements that can be made regarding the derivative calculations. Currently, the entire watercraft is considered as one rigid body. Future work should consider separating the effects of the various components on the stability of the hydrofoil watercraft for more detailed analysis. This may provide insights into the outliers from the dataset.

The future framework should be expanded to include analytical models to calculate dynamic derivatives. The integration of the analytical model will reduce the computation time of the dynamic simulations and may replace the dynamic simulations for early stability prediction. This will allow for faster optimization of hydrofoil configurations and exploration of new hydrofoil concepts in the early design stages.

List of Related Publications

Poster

• Justin Ayinbila Amoah, Hang Xu, *Electric Hydrofoil Boat*, Electrification for Resilient Decarbonized Communities (ERDC) Poster Presentation, 06 September 2023, Montreal, Quebec, Canada

Conference

• Justin Ayinbila Amoah, Hang Xu, Design of Electrical Hydrofoil Configurations for Stability Improvement Using the CFD Method, Canadian Society for Mechanical Engineering/Computational Fluid Dynamics Society of Canada (CSME/CFD) Conference, 26-29 May 2024, Toronto, Ontario, Canada

Paper

• Aron Kessel, Justin Ayinbila Amoah, Irene Banzi, Marcus Ryden, and Hang Xu, Framework for Hydrofoil Stability Analysis, (In Preparation)

References

- [1] IMO, "2023 IMO Strategy on Reduction of GHG Emissions from Ships." Accessed: Mar. 13, 2025. [Online]. Available: https://www.imo.org/en/ourwork/environment/pages/2023-imo-strategy-on-reduction-of-ghg-emissions-from-ships.aspx
- [2] F. M. N. U. Khan, M. G. Rasul, A. S. M. Sayem, and N. Mandal, "Maximizing energy density of lithium-ion batteries for electric vehicles: A critical review," *Energy Reports*, vol. 9, pp. 11–21, Oct. 2023, doi: 10.1016/j.egyr.2023.08.069.
- [3] B. Horel, "System-based modelling of a foiling catamaran," *Ocean Engineering*, vol. 171, pp. 108–119, Jan. 2019, doi: 10.1016/j.oceaneng.2018.10.046.
- [4] Z. Liu, H. Qu, X. Song, Z. Chen, and H. Ni, "Energy-harvesting performance of tandem coupled-pitching hydrofoils under the semi-activated mode: An experimental study," *Energy*, vol. 279, Sep. 2023, doi: 10.1016/j.energy.2023.128060.
- [5] "HMCS Bras D'Or Canada.ca." Accessed: May 27, 2025. [Online]. Available: https://www.canada.ca/en/navy/services/history/ships-histories/bras-dor.html
- [6] C. Wassgren, "Buoyant Force and Center of Buoyancy," Dec. 15, 2021. Accessed: Apr. 10, 2025. [Online]. Available: https://engineering.purdue.edu/~wassgren/teaching/me30800/notesandreading/buoyantforce_reading.pdf
- [7] T. R. Yechout, *Introduction to Aircraft Flight Mechanics*, Third. American Institute of Aeronautics and Astronautics, Inc., 2024. doi: https://doi.org/10.2514/4.107252.
- [8] S. Zikry and F. Fitriadhy, "Seakeeping Performance of a Hydrofoil in Waves using CFD Approach," *Universiti Malaysia Terengganu Journal of Undergraduate Research*, vol. 3, no. 3, pp. 167–176, Jul. 2021, doi: 10.46754/umtjur.2021.07.017.
- [9] K. A. Belibassakis and E. S. Filippas, "Ship propulsion in waves by actively controlled flapping foils," *Applied Ocean Research*, vol. 52, pp. 1–11, Aug. 2015, doi: 10.1016/j.apor.2015.04.009.
- [10] E. Bøckmann and S. Steen, "Experiments with actively pitch-controlled and spring-loaded oscillating foils," *Applied Ocean Research*, vol. 48, pp. 227–235, Oct. 2014, doi: 10.1016/j.apor.2014.09.004.
- [11] K. Matveev and R. Duncan, "Development of the tool for predicting hydrofoil system performance and simulating motion of hydrofoil-assisted boats," *ASNE symposium on High Speed / High Performance Ships and Craft*, Jan. 2004.
- [12] D. P. Raymer, *Aircraft Design: A Conceptual Approach*, Sixth. American Institute of Aeronautics and Astronautics, Inc., 2018. doi: 10.2514/4.104909.

- [13] S. Gudmundsson, General Aviation Aircraft Design: Applied Methods and Procedures. Elsevier, 2022. doi: 10.1016/B978-0-12-818465-3.09989-4.
- [14] J. Murua, P. Martínez, H. Climent, L. Van Zyl, and R. Palacios, "T-tail flutter: Potential-flow modelling, experimental validation and flight tests," *Progress in Aerospace Sciences*, vol. 71, pp. 54–84, Nov. 2014, doi: 10.1016/j.paerosci.2014.07.002.
- [15] R. Cavallaro and L. Demasi, "Challenges, ideas, and innovations of joined-wing configurations: A concept from the past, an opportunity for the future," *Progress in Aerospace Sciences*, vol. 87, pp. 1–93, Nov. 2016, doi: 10.1016/j.paerosci.2016.07.002.
- [16] A. F. Molland and S. R. Turnock, "Chapter 4 Hydrofoils," in *Marine Rudders, Hydrofoils and Control Surfaces (Second Edition)*, Second Edition., A. F. Molland and S. R. Turnock, Eds., Oxford: Butterworth-Heinemann, 2022, pp. 57–89. doi: https://doi.org/10.1016/b978-0-12-824378-7.00005-6.
- [17] "SX220 22FT Boats Yamaha." Accessed: Apr. 10, 2025. [Online]. Available: https://www.yamahaboats.com/boats/categories/22-ft-boats/sx220/
- [18] "Quadrofoil." Accessed: Apr. 10, 2025. [Online]. Available: https://quadrofoil.com/
- [19] J. J. Stilwell and W. R. Porter, "The Naval Use of Hydrofoil Craft Proceedings February 1963 Vol. 89/2/720," Feb. 1963. Accessed: May 27, 2025. [Online]. Available: https://www.usni.org/magazines/proceedings/1963/february/naval-use-hydrofoil-craft
- [20] Ray. Vellinga, *Hydrofoils: Design, Build, Fly.* Peacock Hill Publishing, 2009.
- [21] J. A. D. Ackroyd, "Sir George Cayley, the father of aeronautics Part 2. Cayley's aeroplanes," *Notes and Records of the Royal Society*, vol. 56, no. 3, pp. 333–348, 2002, doi: 10.1098/rsnr.2002.0186.
- [22] J. Carlton, *Marine Propellers and Propulsion*, Fourth. Elsevier Ltd., 2018. doi: 10.1016/c2014-0-01177-x.
- [23] L. Yun and A. Bliault, *High Performance Marine Vessels*. Boston, MA: Springer US, 2012. doi: 10.1007/978-1-4614-0869-7.
- [24] J. J. Stilwell and W. R. Porter, "The Naval Use of Hydrofoil Craft Proceedings February 1963 Vol. 89/2/720," in *The Naval Use of Hydrofoil Craft*, Feb. 1963. Accessed: Jun. 18, 2025. [Online]. Available: https://www.usni.org/magazines/proceedings/1963/february/naval-use-hydrofoil-craft
- [25] Alexander Graham Bell Foundation, "Hydrofoil," https://agbfoundation.ca/hydrofoil/.
- [26] W. M. Shultz, "Boeing Jetfoil," Feb. 1975. doi: 10.4271/750719.
- [27] L. Larsson, "Failures, fantasies and feats in the theoretical/numerical prediction of ship

- performance," *Keynote lecture, 22nd Symposium on Naval Hydrodynamics, Washington DC, USA*, 1998, Accessed: May 28, 2025. [Online]. Available: https://research.chalmers.se/en/publication/252584
- [28] R. Rodriguez, Y. Wang, J. Ozanne, D. Sumer, D. Filev, and D. Soudbakhsh, "Adaptive learning for maximum takeoff efficiency of high-speed sailboats," in *IFAC-PapersOnLine*, Elsevier B.V., 2022, pp. 402–407. doi: 10.1016/j.ifacol.2022.07.345.
- [29] R. J. Johnston, "Hydrofoils," *Naval Engineers Journal*, vol. 97, no. 2, pp. 142–199, Feb. 1985, doi: 10.1111/j.1559-3584.1985.tb03398.x.
- [30] "ENVO Drive Systems." Accessed: Apr. 10, 2025. [Online]. Available: https://envo-drive.com/
- [31] P. Breeze, *Power Generation Technologies*. Elsevier, 2019. doi: 10.1016/C2017-0-03267-6.
- [32] J. Hu, L. Guo, and S. Sun, "Numerical simulation of the potential flow around a submerged hydrofoil with fully nonlinear free-surface conditions," *J Coast Res*, vol. 34, no. I, pp. 238–252, Jan. 2018, doi: 10.2112/jcoastres-d-16-00153.1.
- [33] N. Xie and D. Vassalos, "Performance analysis of 3D hydrofoil under free surface," *Ocean Engineering*, vol. 34, no. 8–9, pp. 1257–1264, Jun. 2007, doi: 10.1016/j.oceaneng.2006.05.008.
- [34] T. Sun, Q. Xie, X. Li, and L. Zou, "Numerical investigation of the effects of free surface on tip-leakage vortex cavitation behaviors over a NACA0009 hydrofoil," *International Journal of Multiphase Flow*, vol. 141, Aug. 2021, doi: 10.1016/j.ijmultiphaseflow.2021.103671.
- [35] A. F. Molland and S. R. Turnock, *Marine Rudders, Hydrofoils and Control Surfaces*. Elsevier Ltd., 2022. doi: 10.1016/c2020-0-01238-7.
- [36] P. Perali *et al.*, "Performance prediction of a hydrofoil near the free surface using low (BEM) and high (RANS) fidelity methods," *Applied Ocean Research*, vol. 151, p. 104157, Oct. 2024, doi: 10.1016/j.apor.2024.104157.
- [37] T. M. Buermann, "An appraisal of hydrofoil supported craft," *Transactions of the IMarEST*, vol. 66, no. 1, Dec. 1954, Accessed: Jun. 01, 2025. [Online]. Available: https://library.imarest.org/record/1852
- [38] G. Vernengo and L. Bonfiglio, "A Computational framework to design optimally loaded supercavitating hydrofoils by differential evolution algorithm and a new viscous lifting line method," *Advances in Engineering Software*, vol. 133, pp. 28–38, Jul. 2019, doi: 10.1016/j.advengsoft.2019.04.006.
- [39] J. Carlton, Marine Propellers and Propulsion. Elsevier, 2019. doi: 10.1016/C2014-0-01177-X.

- [40] C. M. Harwood, K. A. Brucker, F. M. Montero, and Y. L. Young, "Experimental and numerical investigation of ventilation inception and washout mechanisms of a surface-piercing hydrofoil," 2014, Accessed: Jun. 01, 2025. [Online]. Available: https://www.researchgate.net/publication/280568075
- [41] K. I. Matveev, M. P. Wheeler, and T. Xing, "Numerical simulation of air ventilation and its suppression on inclined surface-piercing hydrofoils," *Ocean Engineering*, vol. 175, pp. 251–261, Mar. 2019, doi: 10.1016/j.oceaneng.2019.02.040.
- [42] Y. Masuyama, "Stability analysis and prediction of performance for a hydrofoil sailing boat: Part 2: Dynamic stability analysis," Oct. 1982, doi: 10.3233/isp-1987-3439001.
- [43] J. Huang *et al.*, "Hydrodynamic performance of a surface-piercing hydrofoil with differing oblique angle: A numerical study," *Physics of Fluids*, vol. 36, no. 12, Dec. 2024, doi: 10.1063/5.0236032.
- [44] A. F. Molland and S. R. Turnock, "Physics of control surface operation," in *Marine Rudders, Hydrofoils and Control Surfaces*, Elsevier, 2022, pp. 21–56. doi: 10.1016/b978-0-12-824378-7.00006-8.
- [45] "Differences Between Hydrofoil Boats and Other Boats Candela." Accessed: Apr. 03, 2025. [Online]. Available: https://candela.com/foiling-vs-floating-understanding-the-differences-between-hydrofoil-boats-and-other-boats/
- [46] A. Bagué, "Boat using CFD dynamic stability analysis of a hydrofoiling sailing," 2018.
- [47] M. Angelou and K. J. Spyrou, "Dynamic stability assessment of yacht downwind sailing in regular waves," *Applied Ocean Research*, vol. 111, Jun. 2021, doi: 10.1016/j.apor.2021.102651.
- [48] J.-B. R. G. Souppez, J. M. M.-A. Dewavrin, Gohier F, and Labi G Borba, "Hydrofoil Configurations for Sailing Superyachts: Hydrodynamics, Stability and Performance," *Design & Construction of Super and Mega Yachts 2019*, May 2019, doi: 10.3940/rina.smy.2019.05.
- [49] M. Touw, "Prediction of the longitudinal stability and motions of a hydrofoil ship with a suspension system between the wings and the hull using a state-space model." [Online]. Available: http://repository.tudelft.nl/.
- [50] H. Shen, Q. Xiao, J. Zhou, Y. Su, and X. Bi, "Design of hydrofoil for the resistance improvement of planing boat based on CFD technology," *Ocean Engineering*, vol. 255, Jul. 2022, doi: 10.1016/j.oceaneng.2022.111413.
- [51] K. Akbari Vakilabadi, H. R. Ghafari, and H. Ghassemi, "Investigation of front hydrofoil position influence on the hydrofoil-assisted craft," *Ocean Engineering*, vol. 304, Jul. 2024, doi: 10.1016/j.oceaneng.2024.117901.
- [52] M. Daskovsky, "The hydrofoil in surface proximity, theory and experiment," Ocean

- Engineering, vol. 27, no. 10, pp. 1129–1159, Oct. 2000, doi: 10.1016/S0029-8018(99)00032-3.
- [53] J. G. Leishman, *Introduction to Aerospace Flight Vehicles*. Daytona Beach, Florida: Embry-Riddle Aeronautical University, 2023. doi: 10.15394/eaglepub.
- [54] Y. Masuyama, "Stability analysis and prediction of performance for a hydrofoil sailing boat Part 3: Directional stability analysis," 1987.
- [55] A. Bagué, J. Degroote, T. Demeester, and E. Lataire, "Dynamic stability analysis of a hydrofoiling sailing boat using CFD," 2021. [Online]. Available: http://onepetro.org/jst/article-pdf/6/01/58/2422527/sname-jst-2021-04.pdf/1
- [56] P. Kaplan, P. N. Hu, and S. Tsakonas, "Methods for estimating the longitudinal and lateral dynamic stability of hydrofoil craft," Apr. 1958.
- [57] L. G. Straub, J. M. Wetzel, and W. H. C. Maxwell, "Longitudinal motions and stability of two hydrofoil systems free to heave and pitch in regular waves," Dec. 1961.
- [58] L. G. Straub and E. R. Tinney, "Experimental and analytical studies of dihedral hydrofoils," Nov. 1954. Accessed: Feb. 03, 2025. [Online]. Available: https://hdl.han-dle.net/11299/108301
- [59] Y. Tahara, Y. Masuyama, T. Fukasawa, and M. Katori, "Sail performance analysis of sailing yachts by numerical calculations and experiments," *Fluid Dynamics, Computational Modeling and Applications*, Feb. 2012, doi: 10.5772/28440.
- [60] G. Labi Borba, "Velocity Prediction Program Development for Hydrofoil-Assisted Sailing Monohulls 'EMSHIP' Erasmus Mundus Master Course in 'Integrated Advanced Ship Design," 2019.
- [61] M. Reichel and A. Bednarek, "The experimental studies on hydrofoil resistance," *Archives of Civil and Mechanical Engineering*, vol. 7, no. 3, pp. 167–175, Jan. 2007, doi: 10.1016/S1644-9665(12)60024-7.
- [62] N. T. Thompson, P. R. Whitworth, and K. I. Matveev, "Development of small-scale unmanned hydrofoil boats," *J Unmanned Veh Syst*, vol. 9, no. 1, pp. 21–32, 2021, doi: 10.1139/juvs-2019-0019/asset/images/large/juvs-2019-0019f11.jpeg.
- [63] H. Hansen, K. Hochkirch, I. Burns, and S. Ferguson, "Maneuver simulation and optimization for AC50 class," 2019. [Online]. Available: www.bravosystems.es
- [64] T. N. Schouten, "Stability analysis of the equations of motion for the 2014 Delft Solar Boat," 2015.
- [65] M. Haase, K. Zurcher, G. Davidson, J. R. Binns, G. Thomas, and N. Bose, "Novel CFD-based full-scale resistance prediction for large medium-speed catamarans," *Ocean*

- Engineering, vol. 111, pp. 198–208, Jan. 2016, doi: 10.1016/j.oceaneng.2015.10.018.
- [66] P. Xu *et al.*, "Analysis and optimization of self-propelled performance of wave-driven vehicle hydrofoil under high sea-level condition," *Applied Ocean Research*, vol. 153, Dec. 2024, doi: 10.1016/j.apor.2024.104223.
- [67] M. Dular, R. Bachert, B. Stoffel, and B. Širok, "Influence of the velocity distribution at the inlet boundary on the CFD prediction of local velocity and pressure fields around a hydrofoil," *Exp Therm Fluid Sci*, vol. 32, no. 3, pp. 882–891, Jan. 2008, doi: 10.1016/j.expthermflusci.2007.10.008.
- [68] Y. Shang and J. Horrillo, "Advanced heave control of a hydrofoil-based autonomous surface vehicle: CFD modeling with integrated variable propeller revolution control," *Ocean Engineering*, vol. 315, p. 119800, Jan. 2025, doi: 10.1016/j.oceaneng.2024.119800.
- [69] S. Li, W. Zhong, S. Yu, and H. Wang, "Numerical study of cavitating flows around a hydrofoil with deep analysis of vorticity effects," *Fluid Dynamics and Materials Processing*, vol. 21, no. 1, pp. 179–204, 2025, doi: 10.32604/fdmp.2024.056228.
- [70] M. G. De Giorgi, D. Fontanarosa, and A. Ficarella, "CFD data of unsteady cavitation around a hydrofoil, based on an extended Schnerr-Sauer model coupled with a nucleation model," *Data Brief*, vol. 25, Aug. 2019, doi: 10.1016/j.dib.2019.104226.
- [71] H. Shen, Q. Xiao, J. Zhou, Y. Su, and X. Bi, "Design of hydrofoil for the resistance improvement of planing boat based on CFD technology," *Ocean Engineering*, vol. 255, Jul. 2022, doi: 10.1016/j.oceaneng.2022.111413.
- [72] P. Ploé, "Surrogate-based optimization of hydrofoil shapes using RANS simulations," École centrale de Nantes, 2018. [Online]. Available: https://theses.hal.science/tel-02050026
- [73] N. Raza, I. Mehmood, H. Rafiuddin, S. Bilal, and M. Rafique, "Numerical simulation of free surface effect on moving hydrofoil near free surface," *Proceedings of 2013 10th International Bhurban Conference on Applied Sciences and Technology, IBCAST 2013*, pp. 249–255, 2013, doi: 10.1109/ibcast.2013.6512162.
- [74] S.-E. Kim and D. Cokljat, "Evaluation of an URANS-LES hybrid approach for turbulent free surface flows around surface-piercing bodies," in *International Conference on Numerical Ship Hydrodynamics*, Aug. 2007. Accessed: Jul. 21, 2025. [Online]. Available: https://www.researchgate.net/publication/235084742_evaluation_of_an_urans-les_hybrid_approach_for_turbulent_free_surface_flows_around_surface-piercing_bodies
- [75] A. Çetinkaya and U. Oral Ünal, "A computational study into the effect of the winglets on the performance of fully submerged hydrofoils," *Applied Ocean Research*, vol. 104, Nov. 2020, doi: 10.1016/j.apor.2020.102357.
- [76] P. Kundu, "Numerical simulation of the effects of passive flow control techniques on hydrodynamic performance improvement of the hydrofoil," *Ocean Engineering*, vol. 202,

- Apr. 2020, doi: 10.1016/j.oceaneng.2020.107108.
- [77] M. Andrun, B. Šarić, J. Bašić, and B. Blagojević, "CFD analysis of surface-piercing hydrofoil ventilation inception," in *XXII Theory and Practice of Shipbuilding*, Trogir, Oct. 2016. Accessed: Jun. 01, 2025. [Online]. Available: https://www.researchgate.net/publication/308948321_cfd_analysis_of_surface-piercing_hydrofoil_ventilation_inception
- [78] J. Mahig, "Effect of sweep and drag on hydrofoil stability," *Journal of Engineering for Industry*, vol. 98, no. 3, pp. 965–967, Aug. 1976, doi: 10.1115/1.3439059.
- [79] R. Kant and A. Bhattacharyya, "Hydrofoil geometry and leading-edge modifications: Influence of section profile, aspect ratio, and sweep," *Ocean Engineering*, vol. 262, p. 112306, Oct. 2022, doi: 10.1016/j.oceaneng.2022.112306.
- [80] C. Y. Hsin, J. L. Wu, and S. F. Chang, "Design and optimization method for a two-dimensional hydrofoil," *J Hydrodynam B*, vol. 18, no. 3, pp. 323–329, Jul. 2006, doi: 10.1016/S1001-6058(06)60073-5.
- [81] R. Kant and A. Bhattacharyya, "Hydrofoil geometry and leading-edge modifications: Influence of section profile, aspect ratio, and sweep," *Ocean Engineering*, vol. 262, p. 112306, Oct. 2022, doi: 10.1016/j.oceaneng.2022.112306.
- [82] R. Tannenberg, S. R. Turnock, K. Hochkirch, and S. W. Boyd, "VPP driven parametric design of AC75 hydrofoils," 2023.
- [83] M. Reichel and A. Bednarek, "The experimental studies on hydrofoil resistance," *Archives of Civil and Mechanical Engineering*, vol. 7, no. 3, pp. 167–175, 2007, doi: 10.1016/s1644-9665(12)60024-7.
- [84] S. Longo, F. M. Domínguez, and A. Valiani, "The turbulent structure of the flow field generated by a hydrofoil in stalling condition beneath a water-air interface," *Exp Therm Fluid Sci*, vol. 61, pp. 34–47, Feb. 2015, doi: 10.1016/j.expthermflusci.2014.10.008.
- [85] N. Garg, G. K. W. Kenway, J. R. R. A. Martins, and Y. L. Young, "High-fidelity multipoint hydrostructural optimization of a 3D hydrofoil," *J Fluids Struct*, vol. 71, pp. 15–39, May 2017, doi: 10.1016/j.jfluidstructs.2017.02.001.
- [86] M. Angelou and K. J. Spyrou, "Modeling of transient hydrodynamic lifting forces of sailing yachts and study of their effect on maneuvering in waves," *Ocean Engineering*, vol. 173, pp. 531–547, Feb. 2019, doi: 10.1016/j.oceaneng.2019.01.021.
- [87] P. Kaplan, P. N. Hu, and S. Tsakonas, "Methods for estimating the longitudinal and lateral dynamic stability of hydrofoil craft," Apr. 1958.
- [88] "NAC News Edition 589 (Central Technical School) Naval Association of Canada." Accessed: Mar. 17, 2025. [Online]. Available: https://www.navalassoc.ca/nac-news-edition-589-central-technical-school/

- [89] "Brio Electric Series (2025) Pontoons Princecraft." Accessed: Jun. 18, 2025. [Online]. Available: https://www.princecraft.com/ca/en/products/Pontoons/2025/Brio-Electric-Series.aspx
- [90] "M40P Unmanned Surface Vehicle OceanAlpha." Accessed: Jun. 18, 2025. [Online]. Available: https://oceanalpha.com/product-item/m40p/
- [91] "Navier The Boat of the Future." Accessed: Jun. 18, 2025. [Online]. Available: https://www.navierboat.com/
- [92] "Grand Banks 42 Classic Boats." Accessed: Jun. 18, 2025. [Online]. Available: https://www.boats.com/boats-for-sale/?make=grand-banks&model=42-classic
- [93] "2002 Grand Banks 42 Classic Grand Banks Yachts." Accessed: Jun. 18, 2025. [Online]. Available: https://preowned.grandbanks.com/yacht-listing/2002-grand-banks-42-classic/
- [94] "Eelex 8000 The Electric Day Cruiser with the Power of Silence." Accessed: Jun. 18, 2025. [Online]. Available: https://xshore.com/us/products/eelex-8000/
- [95] "Fliteboard eFoil." Accessed: Jun. 18, 2025. [Online]. Available: https://fliteboard.com/enca
- [96] "Bayliner VR4 Explore Bowrider Boat Models | Bayliner." Accessed: Jun. 18, 2025. [Online]. Available: https://www.bayliner.com/us/en/boats/bowrider/vr4-bowrider.html
- [97] "Manta5 Hydrofoil Bikes." Accessed: Jun. 18, 2025. [Online]. Available: https://manta5.com/
- [98] "Overboat NovaLuxe Yachts." Accessed: Jun. 18, 2025. [Online]. Available: https://www.novaluxeyachts.com/overboat
- [99] "Hydrofoiling Electric Boats and Ferries Candela." Accessed: Jun. 18, 2025. [Online]. Available: https://candela.com/
- [100] "The zero-emission flying boats Home SeaBubbles." Accessed: Jun. 18, 2025. [Online]. Available: https://www.seabubbles.com/
- [101] "Aquarama Riva Anniversary." Accessed: Jun. 18, 2025. [Online]. Available: https://www.riva-anniversary.com/en-us/heritage/history-aquarama
- [102] "MacGregor 26 Sailboat Specs and Review." Accessed: Jun. 18, 2025. [Online]. Available: https://boatinggeeks.com/macgregor-26/
- [103] "WaveRunners Yamaha Motor Canada." Accessed: Jun. 18, 2025. [Online]. Available: https://www.yamaha-motor.ca/en/water/waverunner
- [104] "Meet the Quadrofoil." Accessed: Jun. 18, 2025. [Online]. Available:

- https://quadrofoil.com/
- [105] D. K. Schmidt, *Modern Flight Dynamics*. Reston, VA: American Institute of Aeronautics and Astronautics, Inc., 2023. doi: 10.2514/4.106170.
- [106] L. Larsson, F. Stern, and V. Bertram, "Benchmarking of computational fluid dynamics for ship flows: The Gothenburg 2000 workshop," *Journal of Ship Research*, vol. 47, no. 1, pp. 63–81, Mar. 2003, doi: 10.5957/JSR.2003.47.1.63.
- [107] Simman, "KCS Geometry and Conditions." Accessed: Jun. 23, 2025. [Online]. Available: http://www.simman2008.dk/kcs/kcs_geometry.htm
- [108] A. E. Jeukendrup and J. Martin, "Improving cycling performance: How should we spend our time and money," *Sports Medicine*, vol. 31, no. 7, pp. 559–569, Nov. 2001, doi: 10.2165/00007256-200131070-00009/figures/tab6.
- [109] S. Mokhov, G. Roper, C. A. Meza, and F. et al. Salhany, "Speed: Gina Cody School HPC Facility: Scripts, Tools, and Refs." doi: 10.5281/ZENODO.15484963.
- [110] S. Brizzolara and Y. L. Young, "Physical and theoretical modeling of surface-piercing hydrofoils for a high-speed unmanned surface vessel," *Proceedings of the International Conference on Offshore Mechanics and Arctic Engineering OMAE*, vol. 4, pp. 831–837, Aug. 2013, doi: 10.1115/omae2012-84028.
- [111] L. A. Faison, "Design of a high speed planing hull with a cambered step and surface piercing hydrofoils," Massachusetts Institute of Technology, 2014. Accessed: Jun. 01, 2025. [Online]. Available: https://dspace.mit.edu/handle/1721.1/92144
- [112] G. Fridsma, "Ventilation Inception on a Surface-Piercing Dihedral Hydrofoil with Plane-Face Wedge Section," Defense Documentation Center for Scientific and Technical Information, Sep. 1963.
- [113] R. Rothblum, "Investigation of methods of delaying or controlling ventilation on surface piercing struts," Jan. 01, 1977. Accessed: Jun. 01, 2025. [Online]. Available: https://www.academia.edu/89126713/Investigation_of_methods_of_delaying_or_controlling_ventilation_on_surface_piercing_struts
- [114] J. M. Wetzel, "Experimental Studies of Air Ventilation of Vertical Semi-Submerged Bodies," St. Anthony Falls Hydraulic Laboratory, Jul. 1957. Accessed: Jun. 01, 2025. [Online]. Available: https://hdl.handle.net/11299/108803

Appendix A: Hydrofoil Configurations

Appendix A provides a well-organized collection of hydrofoil types and classifications obtained from extensive research of various literature sources. It offers a categorized overview, supported by real world examples, clarifying the subtle differences that exist within the field of hydrofoil technology.

Hydrofoil Configurations

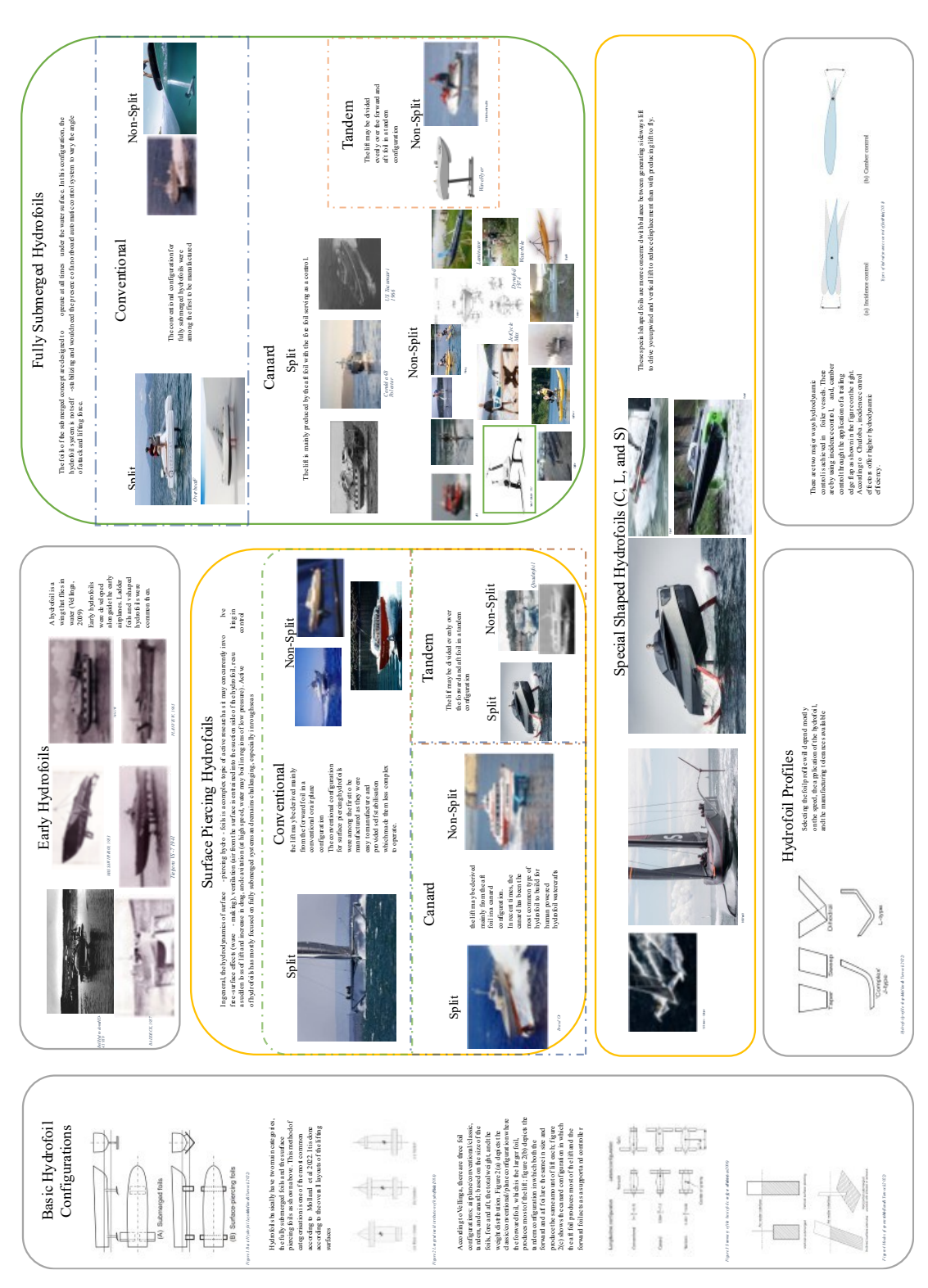


Figure A.1. Literature review poster [87-102]

Appendix B: Hydrofoil Selection and Perfor- mance Study

The information presented in this appendix provides an overview of the hydrofoil watercraft's configuration selection and performance metrics. It includes essential data such as lift values, drag forces, moments affecting the craft's stability, and detailed motion characteristics about its principal axes. This compilation serves as a fundamental reference point for evaluating the craft's responses and performance under different simulated conditions.

Table B.1. Hydrofoil layout decision matrix

Criteria	Weight (%)	Tandem Surface- Piercing	Canard Surface- Piercing	Hybrid (Se- lected)
Passive Stability	35%	Medium (0.5)	Medium (0.5)	High (1)
Control Simplicity	25%	Medium (0.5)	Medium (0.5)	High (1)
L/D Performance	25%	High (1)	Medium (0.5)	High (1)
Cost Effective- ness	15%	High (1)	Medium (0.5)	Low (0)
Weighted Total Score	100%	70	50	85

Guess Sizing and Initial Sizing

Using the equations from aircraft design, estimates of the foil area and geometry parameters were made. Some assumptions in this stage included

- I. The total lift required is equal to the weight at equilibrium
- II. The main wing and tail/canard would have a lift distribution of 75% and 25%, respectively

The guess sizing was performed using Equations 7 to 10 to develop several configurations. A parametric study was conducted using aspect ratios (AR) ranging from 2 to 12 for various spans of the hydrofoil. The AR range was chosen from the existing literature. A NACA 4412 symmetric airfoil section was selected for both the wings.

$$L_{req} = W = m \times g \tag{7}$$

$$S = \frac{L}{0.5 \rho V^2 C_l} \tag{8}$$

$$b = \sqrt{AR \times S} \tag{9}$$

$$c = \frac{S}{h} \tag{10}$$

Where L_{req} is lift required, W is the total weight, m is the total mass; g is the gravity; S is the area; L is lift; ρ is fluid density; V is velocity; C_l is the coefficient of lift; b is the wingspan; AR is aspect ratio.

The configurations from the guess sizing were analysed, focusing on parameters such as stability, drag, and takeoff performance. In addition, trade-off studies were performed to compare the performance of the configurations, which will be discussed in this Appendix.

Configuration Design and Performance Estimation

This section details the configuration design and performance estimation of various hydrofoil watercraft concepts. These concepts were developed with the industry partner, ENVO Drive Systems, for a pedal-assist electric hydrofoil water bike. The design requirements for the water bike are found in Table 3.1.

Table B.2. Design requirements

Max Power	Max Speed	Range	Battery Capacity	Empty Weight	Total Weight	Cruise at
1500 W	20 Km/h	1 Hour	800 Wh	50Kg	120Kg	low speeds (7km/h)

Hydrofoil Configurations

Three hydrofoil configurations were evaluated for their hydrodynamic performance and suitability for a small-scale watercraft operating across takeoff and cruise phases:

- I. Configuration a: Hybrid layout
- II. Configuration b: Surface-piercing dihedral tandem layout
- III. Configuration c: Surface-piercing dihedral canard layout

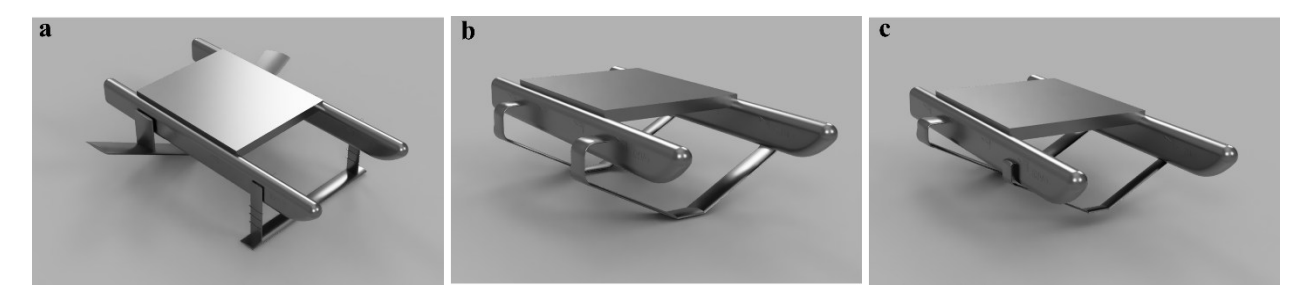


Figure B.1. Model hydrofoil configurations from left to right: a) Hybrid layout, b) Surface-piercing dihedral tandem layout, and c) Surface-piercing dihedral canard layout

Performance Comparison of Configurations

Each configuration was evaluated for performance during takeoff and cruising at different speeds. The performance metrics analyzed included drag, power required, and range at speeds ranging from 7 km/h to 20 km/h. Table B.3 and B.4 present the results for this study which are calculated using the methodology from Hydrofoil Design Build Fly[20].

Power Trade Off Study

A trade-off study was conducted to determine the optimal operational modes and speeds for the watercraft based on the design requirements. Simulations were performed to evaluate the watercraft's performance at three operational conditions: takeoff, cruising, and maximum velocity. The processed data from the simulations are shown in Tables B.3 and B.4. The performance data from the simulations indicate that the range design requirements have been met, with the Surface-piercing Canard Configuration achieving the highest range of 1.56 hours during cruising. The human power was taken from literature[108].

Table B.3. Performance estimation considering both human power and electric propulsion

Mission Profile	Velocity (km/h)	Drag(N)	Required Power (W)	Power Consumption per Meter (Wh/m)	Range (km) 80% Efficiency	Range (km) 63% Efficiency	Range (h)
Takeoff	6.34	193.82	341.12	0.05	-	-	-
Takeoff	7.00	151.30	1059.10	0.04	-	-	-
Takeoff	7.20	251.57	503.14	0.07	-	-	-
Takeoff	9.72	350.00	945.00	0.10	-	-	-
Cruising	7.20	250.00	500.00	0.07	9.22	7.26	1.01
Cruising	9.72	140.00	378.00	0.04	16.46	12.96	1.33
Cruising	10.80	210.00	630.00	0.06	10.97	8.64	0.80
Cruising	11.52	181.92	582.14	0.05	12.66	9.97	0.87
Cruising	14.98	140.16	583.07	0.04	16.44	12.95	0.86
Cruising	18.00	159.92	799.60	0.04	14.41	11.35	0.63
Max	20.00	209.49	1164.76	0.06	11.00	8.66	0.43

Table B.4. Performance estimation considering electric propulsion only

Mission Profile	Velocity (km/h)	Drag(N)	Required Power (W)	Power Consumption per Meter (Wh/m)	Range (km) 80% Efficiency	Range (km) 63% Efficiency	Range (h)
Takeoff	6.34	193.82	341.12	0.05	-	-	-
Takeoff	7.00	151.30	1059.10	0.04	-	-	-
Takeoff	7.20	251.57	503.14	0.07	-	-	-
Takeoff	9.72	350.00	945.00	0.10	-	-	-
Cruising	7.20	250.00	500.00	0.07	9.80	7.84	1.09
Cruising	9.72	140.00	378.00	0.04	17.50	14.00	1.44
Cruising	10.80	210.00	630.00	0.06	11.67	9.33	0.86
Cruising	11.52	181.92	582.14	0.05	13.47	10.78	0.94
Cruising	14.98	140.16	583.07	0.04	17.48	13.99	0.93
Cruising	18.00	159.92	799.60	0.04	15.32	12.26	0.92
Max	20.00	209.49	1164.76	0.06	11.69	9.36	0.47

Selected Layout

The specifications for the selected layout are presented in Table 3.2.

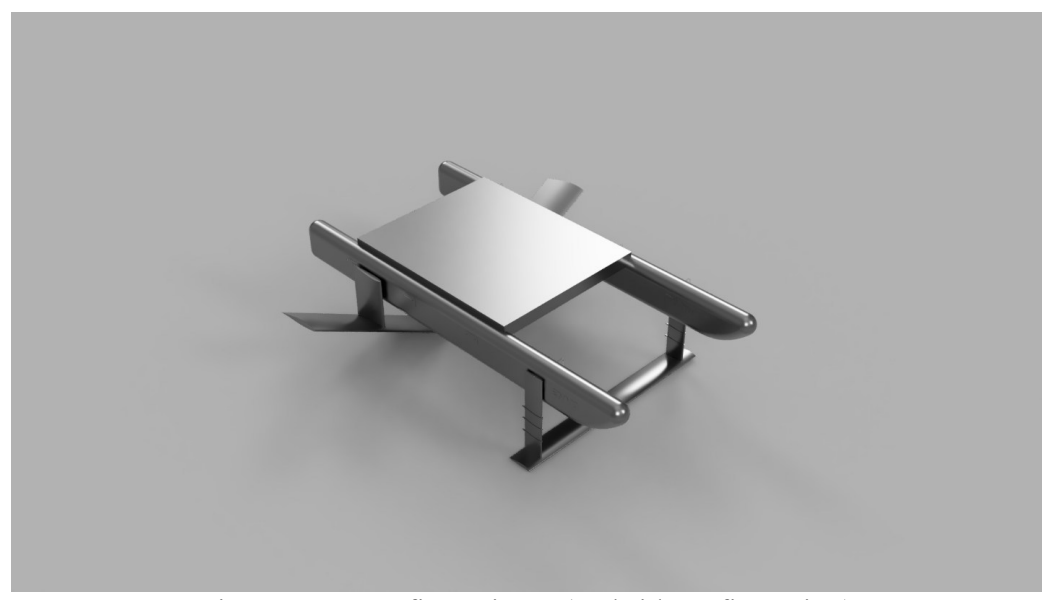


Figure C.2. Configuration a (Hybrid configuration)

Appendix C: High Dihedral Case Study II

The 30° dihedral configuration (Fig. C1) exhibits a close to 0° trim position at equilibrium among the tested dihedral angles. As the dihedral angle increases, the hydrofoil watercraft tends to pitch up at equilibrium for the tested cruise speed of 3m/s. This effect is more pronounced at the 50° dihedral configuration, where the trim angle exceeds -4.5°, as shown in Fig. C.2. Increasing the dihedral angle increases the wing's inclination away from the horizontal plane and, in effect, reduces the effective vertical lift component since more of the lift acts laterally. This relationship can be expressed mathematically as $L_{vertical} = L \cos \Gamma$. To compensate for the change in the vertical lift vector, the hydrofoil watercraft pitches up to increase the AoA, which increases the total lift and generates sufficient vertical lift for steady cruising, effectively shifting the aerodynamic center and altering the trim position.

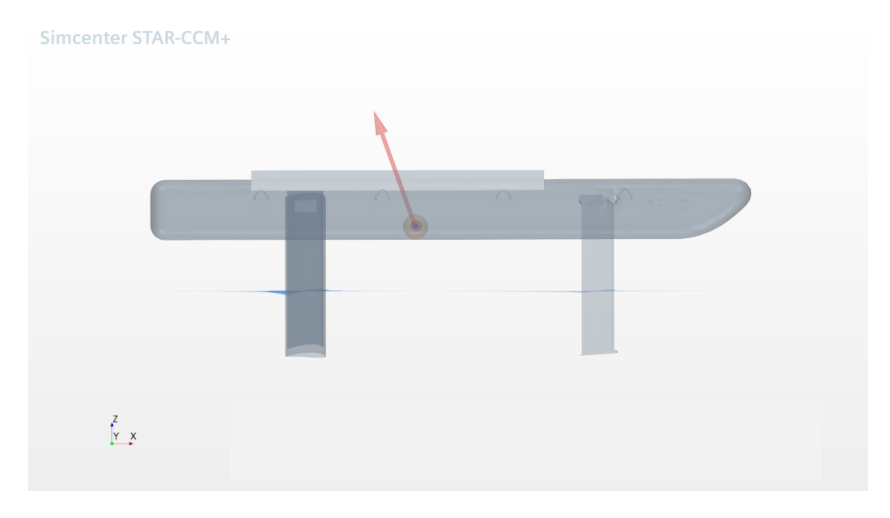


Figure C.1. Visualization of the 30° dihedral model equilibrium position

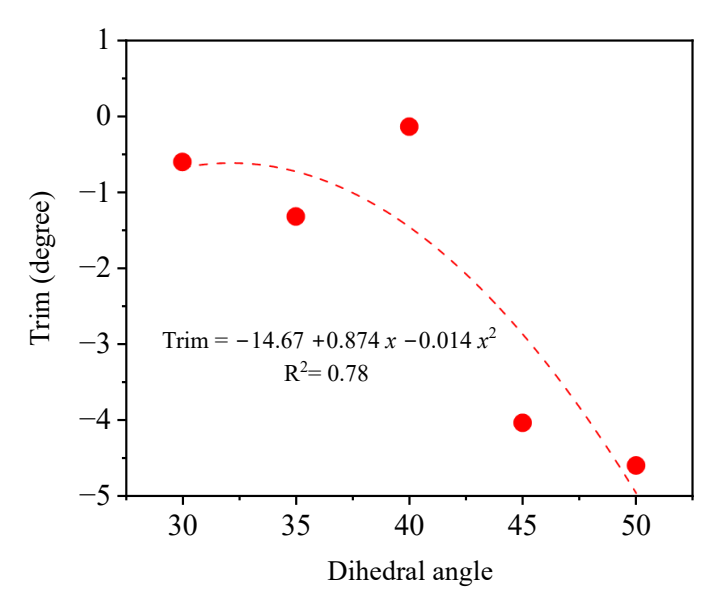


Figure C.2. Trim at the equilibrium position

Stability derivatives with respect to pitch

The stability behavior of a hydrofoil watercraft in response to pitch disturbances is primarily characterized by the pitch moment derivative with respect to the pitch angle, $C_{m_{\theta}}$, and secondarily by cross-coupling derivatives such as the roll moment derivative with respect to pitch, $C_{l_{\theta}}$, and the yaw moment derivative with respect to pitch, $C_{n_{\theta}}$. The calculated stability derivatives under a pitch disturbance are summarised in Table C.1.

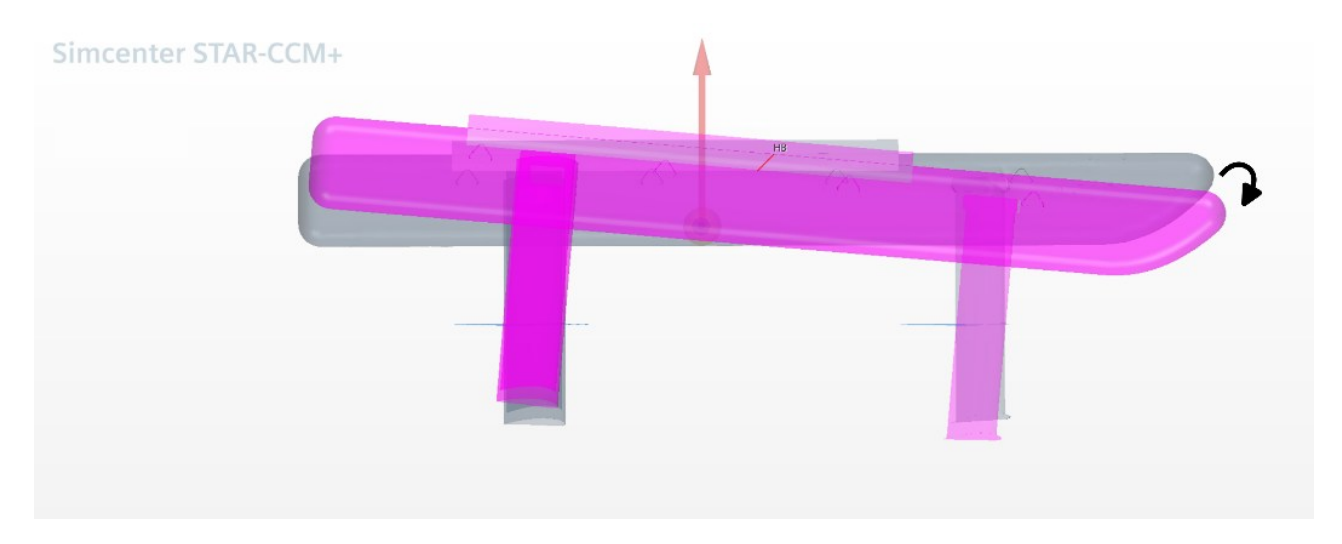


Figure C.3. Introducing a pitch disturbance to the hydrofoil system

Table C.1. Stability derivatives coefficients with respect to pitch

Dihedral Angle (°)	$C_{l_{ heta}}$	$C_{m_{ heta}}$	$C_{n_{\theta}}$
30	-0.0561	-0.2177	-0.1079
35	-0.0056	-0.0487	0.0041
40	-0.0010	0.1890	0.0036
45	-0.0041	0.2180	0.0052
50	0.029951	0.543241	0.055634

Roll Response

As shown in Table C.1, the roll moment stability derivative with respect to pitch perturbations, denoted by $C_{l_{\theta}}$, tends towards a positive value with increasing dihedral. For example, $C_{l_{\theta}}$ decreases from -0.05 at the 30° dihedral to 0.02 at the 50° dihedral angle, which is over a 100% degradation in the roll restoring moment when a pitch disturbance is introduced. As the dihedral angle increases to 50°, $C_{l_{\theta}}$ approaches zero and eventually becomes positive, indicating a reduction in roll resistance as shown in Table C.1. The phenomenon exhibited in Table C.1 can be attributed to:

Lift change: The lift of a surface-piercing hydrofoil is approximately proportional to the submerged area. Changing the pitch angle, θ , results in a change in hydrofoil orientation, which leads to an uneven and asymmetrical submergence in the span direction on both sides of the dihedral wing. The difference in submergence area generates asymmetric lift, creating a destabilizing roll and yaw moment. The destabilising roll/yaw moment increases as the dihedral angle increases, leading to a stronger pitch-roll or pitch-yaw coupling. Furthermore, this coupling can cause oscillatory behavior in the hydrofoil watercraft.

Free surface effects: The presence of small wave disturbances and surface deformation due to the piercing of the water creates local variations in submersion depth. These surface irregularities can cause one side of the wing to submerge slightly more than the other, leading to different wetted areas on the two sides of the wing, which produces asymmetric lift.

Pitch Response

The pitch moment stability derivative, $C_{m_{\theta}}$, starts negative at 30° dihedral, indicating a pitch-stable behaviour. However, $C_{m_{\theta}}$ becomes positive after 40°. A positive stability derivative implies that a pitch disturbance results in a further pitching moment in the same direction, signifying pitch instability. The decreasing pitch stability with increasing dihedral angle can be attributed to factors such as the asymmetric lift generation from the dihedral wing and the changes in the flow angle to the dihedral wing. A pitch disturbance would be expected to cause a symmetric change in wetted area on both sides of the dihedral wing. This is, however, not the case. Factors such as the free surface effects, roll and yaw coupling with pitch, changes in the flow angle, and the nonlinear lift responses that come from the changes in wetted area lead to asymmetric lift on the sides of the dihedral wing, which affect the restoring moments. These effects are however minimal and nonlinear.

The trend and explanation for this behavior are similar to those observed in the previously discussed roll response. In addition, as the hydrofoil watercraft pitches up, the leading edges of the hydrofoil encounter changing flow directions and AoA. These interactions can cause uneven pressure distribution between the left and right sides of the hydrofoil wing, leading to asymmetric lift. The change in the AoA of the dihedral wing shifts the position of the center of pressure closer to the CG, which reduces the pitch restoring moment. As the dihedral angle increases, the center of pressure moves ahead of the CG, creating a destabilizing (positive) pitch moment as seen as the dihedral angle approaches 50°.

Yaw Response

The yaw moment derivative, $C_{n_{\theta}}$, as shown in Table C.1, becomes positive, with an increase in the dihedral angle, indicating reduced directional stability with respect to a pitch disturbance. For this coupled derivative, the 30° dihedral is the only model that shows a yaw restoring moment. The reduced directional stability can be attributed to the asymmetric lift distribution across the span of the dihedral main wing during a pitch perturbation, as described earlier. The asymmetric lift leads to an unbalanced side force, which tends to generate a yaw moment, which could cause the hydrofoil watercraft to veer off-course.

In summary, increasing the dihedral progressively reduces the restoring moments under a pitch disturbance. Hence, the hydrofoil watercraft's ability to self-correct is reduced.

Stability Derivatives with Respect to Roll

The stability behavior of a hydrofoil watercraft in response to roll disturbances is presented in this section. The stability derivatives considered are $C_{m_{\phi}}$, $C_{l_{\phi}}$, and $C_{n_{\phi}}$. The calculated stability derivatives under a roll disturbance are summarised in Table C.2.

Table C.2. Stability derivatives with respect to roll

Dihedral Angle (°)	C_{l_ϕ}	$C_{m_{\phi}}$	$C_{n_{\phi}}$
30	-0.0767	0.1313	-0.0542
35	-0.0724	0.1441	-0.0291
40	-0.0624	0.1590	-0.0290
45	-0.0544	0.1626	-0.0282
50	-0.0459	0.1819	-0.0257

Table C.2 examines the hydrofoil watercraft's stability derivatives in response to a roll disturbance. When a roll disturbance is introduced, there is a decrease in the magnitude of roll and yaw moment derivatives as the dihedral angle increases. This trend indicates reduced restorative moments and thus diminishing dynamic stability at higher dihedral angles. However, for all tested dihedral angles in a roll disturbance, the values of $C_{n_{\phi}}$ are negative, meaning that roll induces a yawing moment which helps reduce coupled roll-yaw oscillations.

Under a roll disturbance, the side of the wing to which the hydrofoil watercraft rolls becomes more submerged, and hence generates more lift. The difference in lift between the two sides of the wing produces a restoring roll moment. Although increasing the dihedral angle increases the lateral lift component, contributing to the roll and yaw restoring moments, the wetted areas are reduced under a similar roll disturbance. This reduction leads to diminishing restorative moments.

While some roll-yaw coupling is expected in surface-piercing dihedral wings, the reduction in $C_{l_{\phi}}$ and $C_{n_{\phi}}$ with increasing dihedral angle suggests increased susceptibility to oscillatory motions like Dutch roll.

The pitch response to roll, on the other hand, is unstable throughout all tested dihedral angles. Theoretically, a roll disturbance does not influence pitch motion. However, due to asymmetries from surface-piercing effects and dihedral geometry, there is an imbalance in the vertical lift component of the dihedral wing. This imbalance leads to a bow-up or bow-down pitching moment, indicated by the positive increase in $C_{m_{\phi}}$ from Table C.2. The pitch sensitivity to a roll disturbance may also be due to the canard configuration.

Stability Derivatives with Respect to Yaw

Similar trends are observed in yaw-induced stability responses (See Table C.3). Higher dihedral angles reduce the hydrofoil's ability to generate corrective roll and yaw moments, indicating reduced dynamic stability. Since roll and yaw are coupled in hydrofoil dynamics, especially with surface-piercing elements, these results suggest that increasing dihedral weakens both axes' stability simultaneously, making the system more susceptible to oscillatory behavior.

Table C.3. Stability derivatives with respect to yaw

Dihedral Angle (°)	$C_{l_{\psi}}$	$C_{m_{\psi}}$	$C_{n_{\psi}}$
30	-0.0380	0.1176	-0.0192
35	-0.0053	0.1257	-0.0061
40	-0.0060	0.1505	-0.0067
45	-0.0076	0.1573	-0.0096
50	-0.0113	0.1746	-0.0100

Table C.3 shows the tendency of the hydrofoil watercraft to produce a righting moment to return to the equilibrium position after a yaw disturbance is introduced. The trend here is similar to that of the roll derivatives, which aligns with aircraft theory due to their coupled interrelation. Under a yaw disturbance, the hydrofoil watercraft exhibits stability in roll and yaw while having decreasing stability in pitch as the dihedral angle increases.

Flow direction: A yaw disturbance causes the dihedral wing to have a lateral motion vector component of the water flow. This lateral component creates a side force on each hydrofoil due to the angle of the side to the incoming flow. A portion of the side force produced is converted into

vertical lift due to the dihedral wing and does not contribute to directional correction. The lateral component of this force, which contributes to the yaw stability, can be expressed by $F_{side_{lateral}} = F_{side} \cos \Gamma$. This force component decreases as the dihedral angle increases, under the same disturbance. The yaw moment arm also decreases as the dihedral angle increases, leading to less yaw stability.

Yaw-Roll Coupling Interference: In surface-piercing foils, yaw often causes secondary roll due to asymmetric lift, and this roll further introduces asymmetric wetted areas across the dihedral wing, which produces asymmetric lift, affecting yaw recovery in a nonlinear way. The coupling between roll and yaw becomes more intense with increased dihedral, because any yaw-induced roll feeds back into the yaw response.

Appendix D: Dihedral Effect Isolation Study

This appendix contains data from the main results presented in this study. The lift, drag, and moment derivatives are presented in their dimensional forms.

Table D.1. Canard incidence angle adjustment

Dihedral Angle	Dihedral Sinkage	Canard Trim	Dihedral Moment	Canard Moment	Total Mo- ment	Mean To- tal Lift
30	0.507671	3.1	357.5084	-345.405	12.10329	1176.577
35	0.483621	3.1	356.7232	-356.022	0.701372	1176.759
40	0.459815	2.7	355.4019	-347.794	7.608322	1176.896
45	0.434606	2.7	352.8776	-353.096	-0.21842	1175.862
50	0.39336	2.4	353.7693	-350.441	3.328248	1181.711

Lift and Drag Characteristics

Table D.1 show that as the dihedral angle increases, the total vertical lift decreases. Geometrically, dihedral hydrofoil surfaces produce less vertical lift and more lateral force components. The drag coefficient remains relatively stable across the configurations. This may suggest that the dihedral orientation of the main wing does not significantly disrupt flow attachment or increase drag. This could imply some hydrodynamic benefits despite the reduction in stability. More investigations are needed to confirm this relation.

Table D.2. Stability derivatives in response to a roll disturbance

Dihedral Angle (°)	Roll Moment Deriva- tive (Nm)	Pitch Moment Deriva- tive (Nm)	Yaw Moment Deriva- tive (Nm)
30	-25.59927	-369.3745	-15.99038
35	-10.35309	-335.705	-10.90995
40	-11.16702	-329.248	-13.16561
45	-1.05004	-356.8828	-10.79201
50	6.54253	-400.8385	8.46203

Table D.3. Stability derivatives in response to a pitch disturbance

Dihedral Angle (°)	Roll Moment Deriva- tive (Nm)	Pitch Moment Deriva- tive (Nm)	Yaw Moment Deriva- tive (Nm)
30	-1.251283655	-449.5613716	-0.876051511
35	6.487132802	-392.6468515	9.706359099
40	-0.654802682	-406.3994956	0.348620879
45	-7.971890547	-408.4776534	-13.63360476
50	14.00640072	-472.1471686	22.78964889

Table D.4. Stability derivatives in response to a yaw disturbance

Dihedral Angle (°)	Roll Moment Deriva- tive (Nm)	Pitch Moment Deriva- tive (Nm)	Yaw Moment Deriva- tive (Nm)
30	-15.78209946	-364.8208563	-7.144283654
35	-12.03287156	-333.4050315	-4.270734593
40	-10.62659655	-323.573888	-2.662971884
45	-7.906842417	-341.4478497	-1.017046387
50	-12.85821652	-391.4007133	-25.27194501

Appendix E: Simulation Setup and Convergence

Appendix E presents the conditions for the simulation setup as well as the force convergence criteria and mesh convergence study. It also presents plots of the boundary conditions and mesh. Figures E.1 and E.2 display the lift and drag convergence for the separate parts of the hydrofoil watercraft. Figure E.3 shows the motion of the watercraft to the equilibrium position. Figure E.8 displays the lift force mesh convergence plot. The simulations in this thesis were run on Concordia University's Speed high performance computing [109].

Table E.1 Simulation conditions

Item	Condition
Simulation Code	Star-CCM+ V15.04.010-R8
Flow condition	Multiphase air-water flow (constant density)
Analysis method	Implicit unsteady
Time step	0.04
Turbulent model	k-ε
Mesh cells	$8 \times 10^5 - 3 \times 10^6$
Velocity range	1.74 m/s - 5.56 m/s
Length based Rn	$\sim 6 \times 10^6 - 2 \times 10^7$
Inlet boundary	Velocity inlet
Outlet boundary	Pressure
Walls	No slip

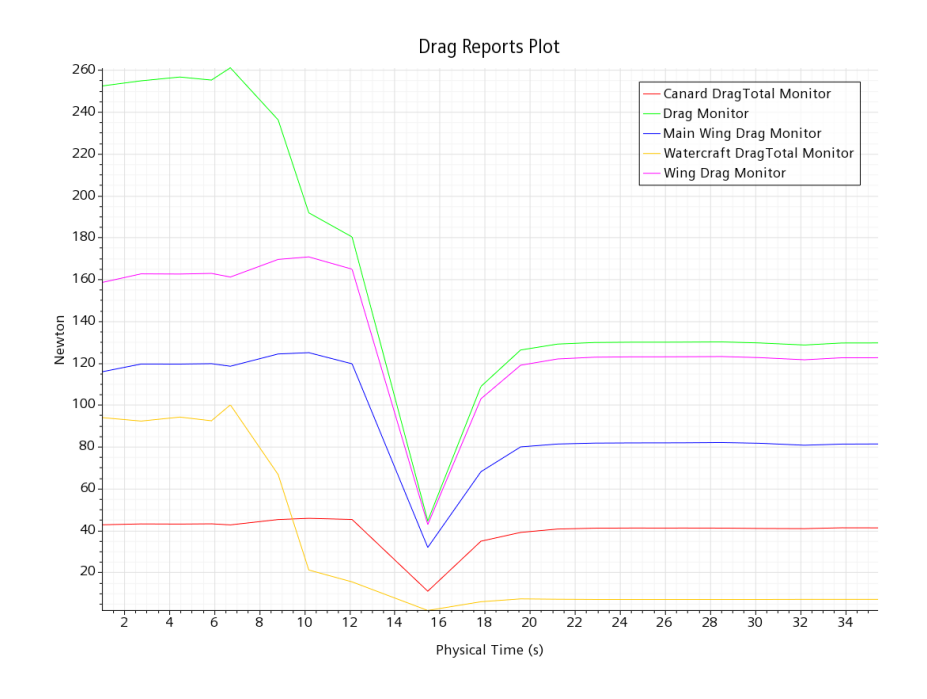


Figure E.1. Sample drag report plot

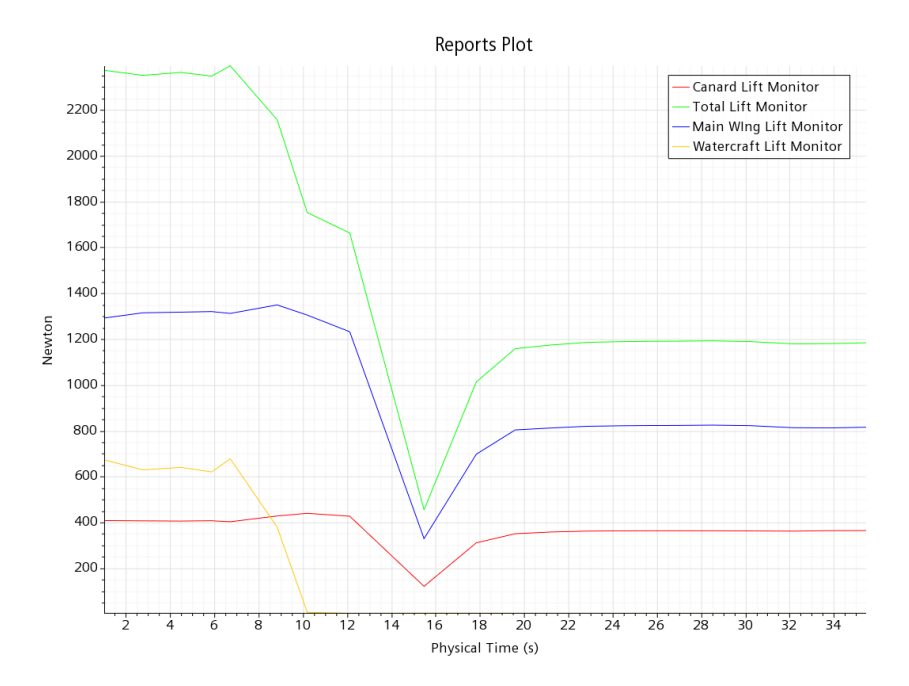


Figure E.2. Sample lift report plot

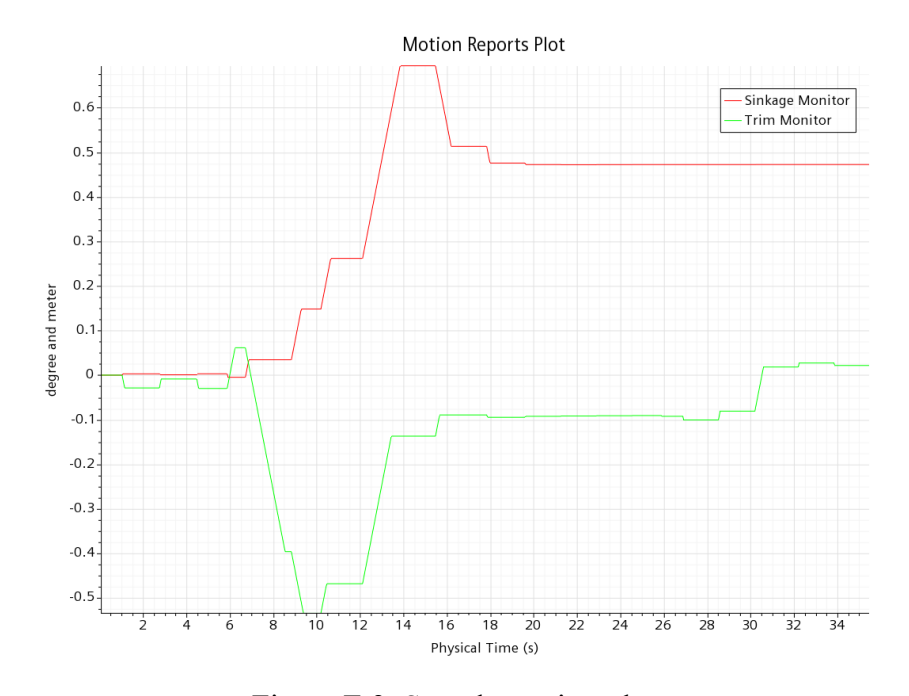


Figure E.3. Sample motion plot

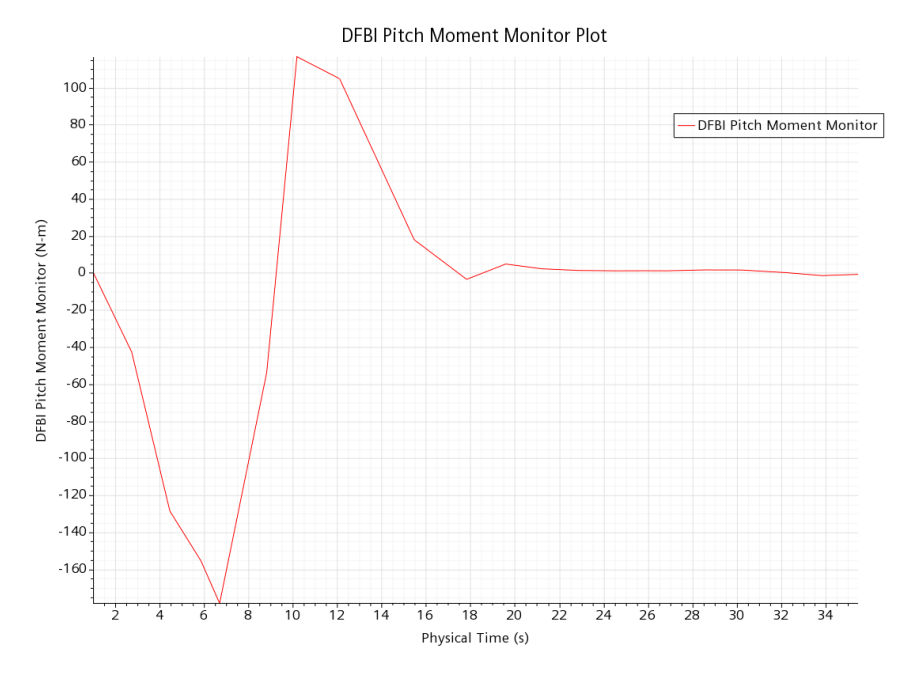


Figure E.4. Sample moment plot

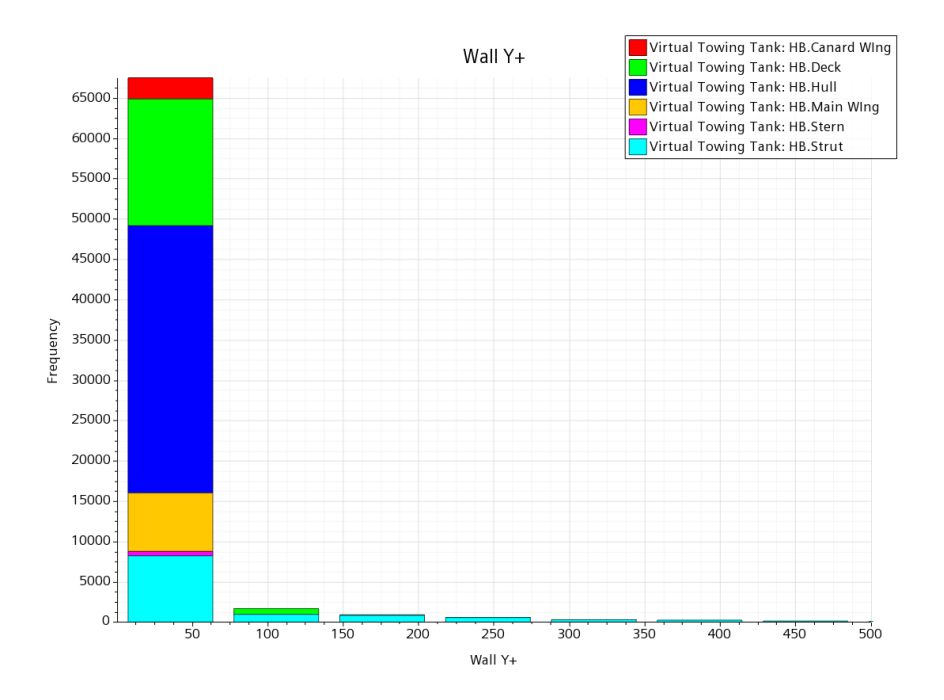


Figure E.5. Sample wall y+ value study

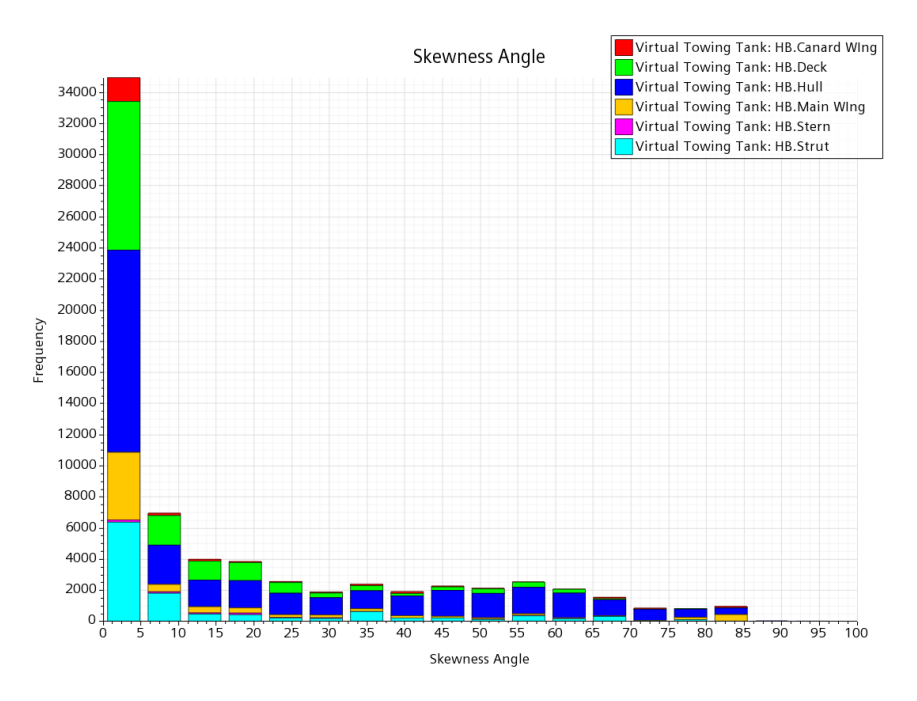


Figure E.6. Sample mesh skewness angle study

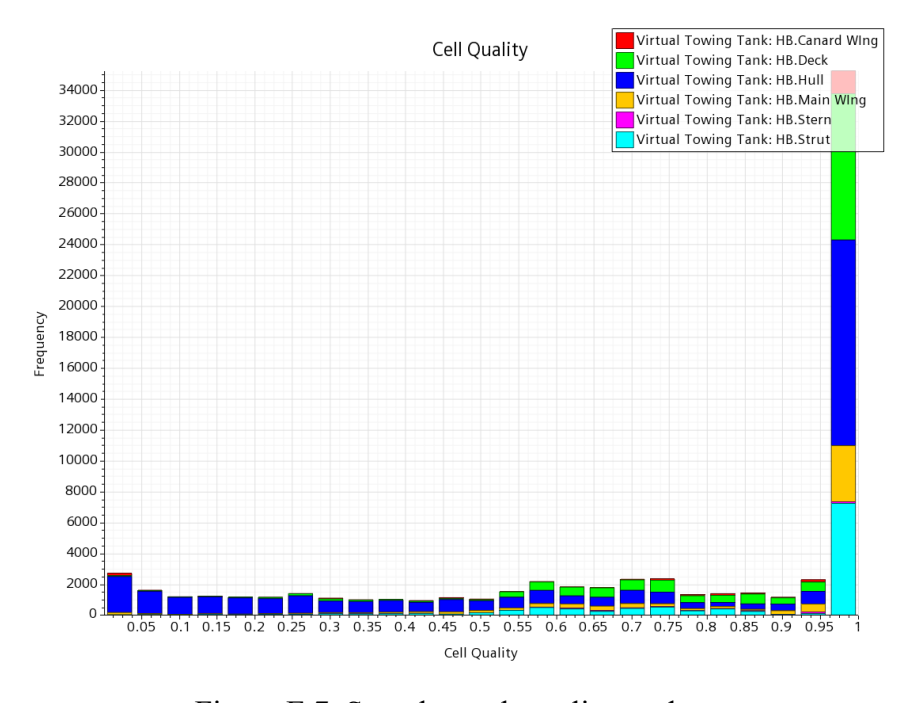


Figure E.7. Sample mesh quality study

Mesh Convergence Study

A mesh convergence study was conducted to evaluate the sensitivity of simulation results to mesh resolution and ensure numerical accuracy in the CFD predictions. Five base mesh sizes were evaluated: 0.084375 m, 0.1125 m, 0.135 m, 0.140625 m, and 0.16875 m, arranged from the coarsest to the finest mesh studied. For each mesh, the lift, drag, moments, DFBI (Dynamic Fluid Body Interaction) lift and moment, and sinkage were measured.

Mesh Independence Study

The finest mesh (base size = 0.084375 m) produced physically unrealistic lift and moment values, which did not converge to a single value, suggesting numerical instability. Hence, this mesh was excluded from further consideration. For the remaining meshes, trends in hydrodynamic forces and sinkage were analyzed to assess convergence.

As the mesh was refined from 0.16875 m to 0.1125 m, the lift values fluctuated slightly, while drag and sinkage showed more consistent trends. Notably, the mesh with base size 0.1125 m yielded a lift of 1178.6 N, which was closest to the analytically calculated lift of 1177.2 N. The variation in lift to this mesh size was also less than 1%, which suggests acceptable mesh independence for engineering analysis.

The DFBI lift and moment values also stabilized with finer meshes. At a base size of 0.11255 m, the DFBI moment was 0.27 Nm and the DFBI lift was -0.07 N, compared to 10.35 Nm and -6.57 N at 0.140625 m. These variations reflect the sensitivity of dynamic body interaction modelling to mesh resolution but remain within an acceptable range.

Final Mesh Selection

Based on the convergence trends, the mesh with a base size of 0.1125 m was selected for subsequent simulations. This mesh provided a balance between accuracy and computational cost. It demonstrated reasonable agreement in lift, drag, and sinkage compared to finer meshes, while avoiding instability and non-convergence.

A summary of the mesh convergence study is provided in Tables E2 and E3, highlighting the changes in forces and confirming the mesh independence of the selected grid.

Table E.2. Mesh convergence study

Base size (m)	Lift (N)	Drag (N)	Moment (Nm)	DFBI lift (N)	DFBI mo- ment (Nm)	Sinkage (m)	Simulation state
0.225	1183.85	138.246	375.358	1.67646	-0.65	0.48125	Converged
0.16875	1203.77	158.177	377.979	2.8302	36.5643	0.66204	Diverged
0.14063	1171.44	155.292	357.168	-6.5663	10.352	0.60492	Converged
0.135	1179.11	140.717	374.159	-0.5667	7.97674	0.5384	Converged
0.1125	1178.65	130.272	377.456	-0.076	0.27017	0.49124	Selected
0.08438	1908.26	315.583	226.386	-338.14	-34.281	0.64851	Diverged

Table E.3. Force and moment change mesh convergence study

Base size (m)	ΔLift (%)	ΔDrag (%)	ΔSinkage (%)	Comparison to analytical lift (%)	Simulation state
0.225	N/A	N/A	N/A	N/A	Converged
0.16875	1.68241	14.4171	37.5667	2.25683	Diverged
0.14063	-2.6853	1.82439	-8.6285	-0.4891	Converged
0.135	0.65458	9.38539	-10.997	0.16232	Converged
0.1125	-0.2089	0.9748	-1.4141	0.12277	Selected
0.08438	N/A	N/A	N/A	N/A	Diverged

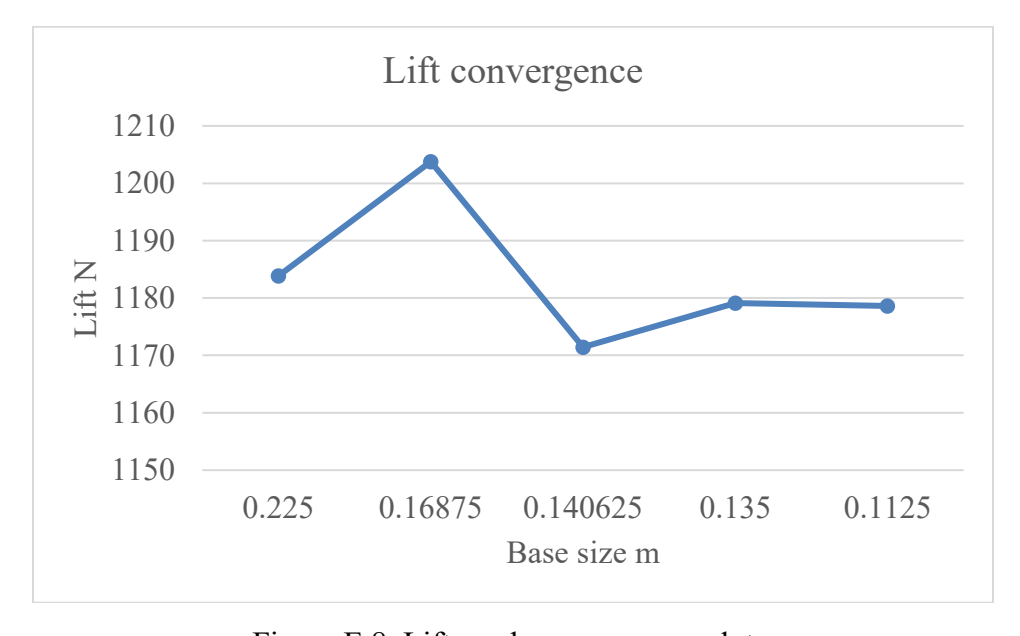


Figure E.8. Lift mesh convergence plot